# Dissertation

submitted to the

Combined Faculties of the Natural Sciences and Mathematics

of the Ruperto-Carola-University of Heidelberg, Germany

for the degree of

Doctor of Natural Sciences

Put forward by

Dipl.-Phys. Martin Hennemann

born in Bamberg, Germany

Oral examination: 30 January 2009

# Multiwavelength observations of massive star-forming regions selected in the far-infrared

Referees: Prof. Dr. Dietrich Lemke
Prof. Dr. Wolfgang Duschl

## Beobachtungen von im Ferninfrarot ausgewählten massereichen Sternentstehungsgebieten in mehreren Spektralbereichen

Es existieren nur wenige Beobachtungen der frühesten Entwicklungsstadien massereicher Sterne. Dies motivierte die Auswahl von massereichen Sternentstehungsgebieten mit Hilfe der 170 $\mu$m ISOPHOT Zufallsdurchmusterung. Die Auswertung umfangreicher Nachfolgebeobachtungen bei Wellenlängen vom Nahinfrarot- bis in den (Sub-)Millimeterbereich ergibt eine Anzahl massereicher Klumpen und erlaubt die Charakterisierung der damit verknüpften Sternentstehung. Die Klumpen bestehen zu einem großen Anteil aus kaltem, staubreichem Material bei Temperaturen zwischen 12 und 22 K, und mehrere haben Massen von 100 $M_\odot$ oder darüber. Der Sternentstehungsprozess hat in allen begonnen und sie enthalten eingebettete Mittelinfrarotquellen, die junge stellare Objekte geringer oder mittlerer Masse darstellen. Mittels Millimeterinterferometrie gelingt in einer Fallstudie die Entdeckung zweier kompakter Kerne, die in einen massereichen Klumpen eingebettet sind. Beide treiben energiereiche Ausflüsse und akkretieren mit möglicherweise hohen Raten, und sind damit Beispiele der frühesten Stadien von entstehenden Sternen mittlerer oder hoher Masse. Die Bedeutung hoher räumlicher Auflösung im Infrarot für die Erforschung der Entstehung massereicher Sterne begründet dezidierte Beobachtungsprogramme mit dem Herschel Weltraumobservatorium. Desweiteren wurde an der Vorbereitung des JWST MIRI Instruments mitgearbeitet, denn besonders die damit erreichbare beispiellose Abbildungsleistung wird wichtige Eigenschaften der untersuchten Quellen aufdecken.

## Multiwavelength observations of massive star-forming regions selected in the far-infrared

The lack of observations of the earliest stages in high-mass star formation motivated the selection of massive star-forming regions using the 170 $\mu$m ISOPHOT Serendipity Survey. The evaluation of comprehensive follow-up observations, covering near-infrared to (sub-)millimetre wavelengths, identifies massive clumps and characterises the star-forming content in detail. The clumps comprise a large fraction of cold dusty material at temperatures between 12 and 22 K, and several have masses of 100 $M_\odot$ or more. Star formation has initiated in every clump, as they harbour embedded sources detected in the mid-infrared that represent low- to intermediate-mass young stellar objects. One case study uses millimetre interferometry and discovers two compact cores of about 15 $M_\odot$ embedded in a massive clump. They are driving energetic outflows and may accrete at high rates, and thus represent examples for the first stages of forming intermediate- to high-mass stars. The importance of high spatial resolution in the infrared for the study of high-mass star formation drives dedicated observing programmes with the Herschel Space Observatory. Furthermore, an active part in the preparation of the JWST MIRI instrument was taken because in particular its unprecedented imaging capabilities will allow to constrain crucial properties of the investigated sources.

# Contents

# Chapter 1

# Introduction: The early phases of high-mass star formation

## 1.1 The formation of high-mass stars

Stars form in the densest parts of interstellar molecular clouds. The star-forming material comprises mostly molecular gas and dust particles. The clouds extend on scales of parsec and appear clumpy and filamentary on smaller scales. The star formation process initiates in dense, cold cores which form the smallest cloud entities. According to the nomenclature adopted in this work, clumps are overdense substructures of clouds with sizes of roughly 0.5 pc, and they usually comprise cores that are smaller by roughly a factor of ten. Cores are thought to be the direct progenitors of individual stars or stellar systems of a few, whereas clumps may rather form stellar associations or clusters.

Dedicated observations have revealed much about the early phases of solar-type star formation in the last two decades. At present, an evolutionary sequence from the starless or prestellar cores to the protostellar cores is supported by many studies. Different phases are distinguished by their spectral energy distributions as shown in Figure 1.1. Notably, the condensation of the star-forming material to dense, cold cores marks the beginning of the sequence. Examples for such objects, having masses $\mathrm{M} \lesssim 10\,\mathrm{M}_\odot$, are known e.g. in the nearby Taurus and Ophiuchus star-forming regions. They are currently studied in great detail regarding their physical and chemical properties as well as their evolution with respect to the stellar initial mass function [Di Francesco *et al.*, 2007; Ward-Thompson *et al.*, 2007].

The upper end of the stellar mass distribution is formed by high-mass stars, i.e. stars with masses of about $8\,\mathrm{M}_\odot$ or more (see Table 1.1). They play an important role in that they synthesise heavy elements and stipulate the energy budget of the interstellar medium throughout their lifetime. Their origin is a lively debated issue, though [Beuther *et al.*, 2008]. Only recently have approaches been presented to establish an evolutionary sequence leading to high-mass stars based on observations and theoretical considerations [Beuther *et al.*, 2007; Zinnecker and Yorke, 2007]. Several issues that appear to distinguish the formation process of high-mass stars from the evolution of low-mass dense cores to stars have to be incorporated:

1. Presumably, high-mass stars do not undergo a pre-main-sequence phase, but the core hydrogen burning begins while the accretion of circumstellar material is still ongoing.

2. The radiative pressure that high-mass stars exert on matter in their immediate

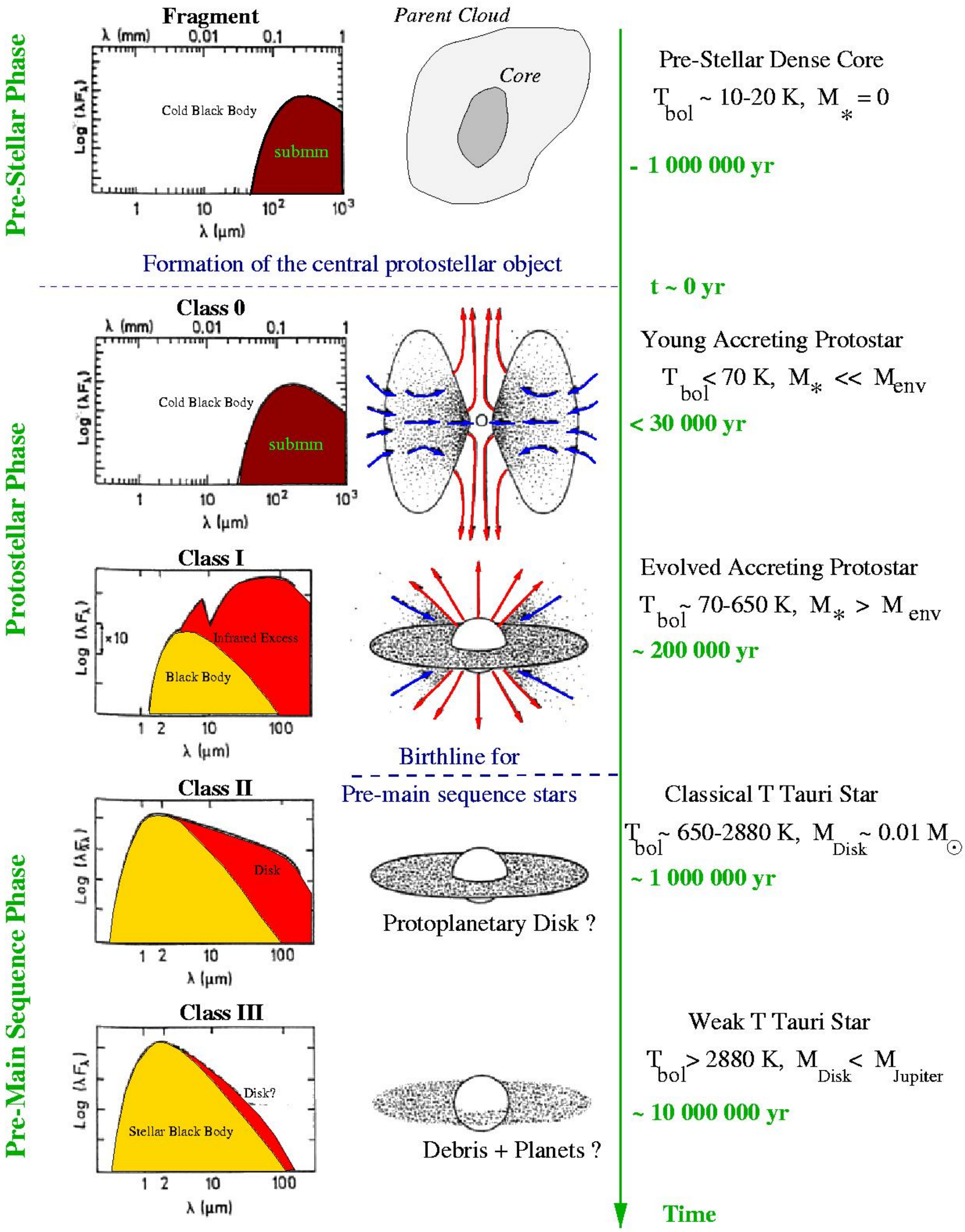

Figure 1.1: Evolutionary sequence of low-mass young stellar objects. Adopted from André [1994].

vicinity has to be overcome to allow accretion.

3. High-mass stars heavily influence their local environment also via gravitational interactions, powerful outflows and winds, and ionising radiation.

4. High-mass stars are seldomly (if at all) formed in isolation (see Figure 1.2).

Related to the first item, the term "high-mass protostar" remains disputable [Evans, 2008]. It may be used for objects with ongoing accretion, or, more restrictive, for sources whose luminosity is dominated by the accretion luminosity that is generated from the release of gravitational energy. However, the latter is difficult to probe observationally.

| Mass ($M_\odot$) | Designation | Spectral Type | MS Lifetime (yr) | Rel. Abundance[a] |
|---|---|---|---|---|
| 8...16 | Early B-type | B3V...B0V | $< 4 \cdot 10^7$ | 0.06 |
| 16...32 | Late O-type | O9V...O6V | $< 2 \cdot 10^7$ | 0.02 |
| 32...64 | Early O-type | O5V...O2V | $< 6 \cdot 10^6$ | 0.009 |
| 64...128 | O/Wolf-Rayet-type | WNL-H[b] | $< 3 \cdot 10^6$ | 0.004 |

[a] Corresponding to a logarithmic slope 1.35 of the stellar mass function, normalised to the 1...2 $M_\odot$ mass bin.

[b] Nitrogen-rich late-type Wolf-Rayet stars that are still on the main sequence.

Table 1.1: Definition of main-sequence high-mass stars in logarithmic mass ranges [Zinnecker and Yorke, 2007, and references therein].

The issue of radiation pressure that could inhibit accretion stimulated different theoretical concepts for the high-mass star formation process. In short, they are usually referenced as monolithic collapse [e.g. McKee and Tan, 2002, 2003], competitive accretion [e.g. Bonnell *et al.*, 2001] and stellar collisions and mergers [e.g. Zinnecker, 1982; Bonnell *et al.*, 1998]. The latter scenario requires extreme stellar densities of $10^6\,\mathrm{pc}^{-3}$ [Bonnell and Bate, 2005] and may play a role for the densely packed cores of massive star clusters. There has been a vigorous debate in recent years which scenario is realistic [Krumholz *et al.*, 2005c; Dobbs *et al.*, 2005; Bonnell and Bate, 2006]. It was pointed out more recently that they are not exclusive and may apply depending on the physical scales and environmental conditions [Krumholz and Bonnell, 2007; Clark *et al.*, 2008]. In the following, theoretical models of monolithic core collapse, fragmentation, and competitive accretion are outlined, and also the theoretical considerations of the accretion process. Altogether, these aspects may eventually form a comprehensive picture of high-mass star formation.

### 1.1.1 Monolithic collapse of massive, turbulent cores

The scenario retaining most similarities with the low-mass star formation process is the monolithic collapse of massive cores. As the name implies, this concept assumes that compact massive cores form, e.g. as a result of fragmentation in turbulent molecular clouds [Padoan and Nordlund, 2002]. Furthermore, they should be relatively long-lived over several free-fall times. McKee and Tan [2003] have presented a model for massive, turbulent cores in pressure equilibrium with the environment. On the basis that the formation of high-mass stars may occur only in regions with a column density of about $1\,\mathrm{g\,cm^{-2}}$, as discussed by Krumholz and McKee [2008], they derive that the pressure in these environments is as high as several $10^8\,k_\mathrm{B}\,\mathrm{K\,cm^{-3}}$. These values are much larger than the average molecular cloud parameters. The cores that become unstable are necessarily very dense

Figure 1.2: Near-infrared colour composite of the Orion Nebula Cluster, covering about $0.9 \times 0.9\,\mathrm{pc}$ at the distance of 410 pc. Roughly 1000 stars, only $10^6$ yr old, form the cluster around the bright Trapezium stars near the centre. At least three of the Trapezium stars are multiple systems with masses between 3 and $34\,\mathrm{M}_\odot$. In the north-west of the Trapezium, a number of yellow to red objects mark the crowded Orion BN/KL region that harbours the nearest high-mass protostar candidates. From there to the upper right of the image, a wide opening-angle outflow with many individual bow shock arcs can be seen as faint red features. Credit: McCaughrean & ESO.

and compact, and they collapse with high accretion rates on the order of $10^{-3}\,\mathrm{M}_\odot\,\mathrm{yr}^{-1}$. The substructure of the cores, imprinted by their turbulent, nonthermal composition, leads to fluctuations in the accretion rates. The time to form a high-mass star is about $10^5$ yr.

### 1.1.2 Fragmentation of molecular clouds, cores and radiative feedback

If massive clouds were supported by thermal pressure exclusively, they would fragment to relatively small condensations [Larson, 2005; Jappsen *et al.*, 2005; Bonnell *et al.*, 2006]. The resulting scales are given by the Jeans length

$$\lambda_\mathrm{J} \approx 0.19\,\mathrm{pc} \times (\mathrm{T}/10\,\mathrm{K})^{1/2} \times (\mathrm{n_{H_2}}/10^4\,\mathrm{cm^{-3}})^{-1/2}$$

and the Jeans mass

$$\mathrm{M_J} \approx 1\,\mathrm{M}_\odot\,(\mathrm{T}/10\,\mathrm{K})^{3/2}\,(\mathrm{n_{H_2}}/10^4\,\mathrm{cm^{-3}})^{-1/2}$$

[Stahler and Palla, 2005] and do not depend on the total mass. In numerical simulations of collapse and fragmentation mainly controlled by gravity and thermal pressure, the number of fragments that form from a cloud or clump is generally comparable to the number of Jeans masses present initially.

If the fragmentation is controlled by supersonic turbulence, it will likely result in a distribution of core masses [Padoan and Nordlund, 2002; Mac Low and Klessen, 2004, and references therein]. In the "gravoturbulent" theory that also includes the role of gravity, molecular cloud cores are transient features that are generated by the dynamical flow in the cloud. Those cores with an excess of gravitational energy collapse rapidly to form stars, whereas the others with sufficiently large internal or kinetic energies reexpand once the turbulent compression fades. The spectrum of core masses may determine the stellar initial mass function. This seems to be universal across the Milky Way and even in the neighbouring galaxies [Chabrier, 2003]. Padoan *et al.* [2007] find that the mass distribution of the unstable cores that will collapse in their MHD simulations is reproducing the stellar initial mass function well, and is in qualitative agreement with the less well determined mass distributions of prestellar cores selected from dust emission or molecular line observations. This may indicate that the fragmentation controlled by turbulence plays a major role, and the influence of thermal pressure is minor. However, the comparison of mass functions does not serve as a good discriminator, because it appears that many proposed models can reproduce mass functions similar to the stellar.

On smaller scales of individual cores, the simulations of Krumholz *et al.* [2007] suggest that compact, massive, and turbulent cores as described above do not fragment strongly. This is the consequence of the radiative feedback of the primary object. The high accretion luminosity within the environment of high optical depth quickly heats the surrounding core material, which prevents local collapse. Thus, the majority of the mass is accreted onto one object, and only a small fraction forms additional low-mass objects.

### 1.1.3 Competitive accretion

The concept of competitive accretion does not require the initial formation of massive cores as progenitors of high-mass stars. Instead, the fragmentation of molecular clouds into cores of about one Jeans mass ($\approx 0.5\,\mathrm{M}_\odot$) sets the stage. The ambient, initially unbound cloud material between the cores is then accreted onto the cores that form low-mass protostars and aggregate to small clusters [Bonnell and Bate, 2006]. The stellar seeds close to the centres of the gravitational potential are embedded in the highest-density material with the lowest velocity dispersion. Thus, they are able to accrete significant amounts of the material and assemble the high-mass stars, whereas those that reside far from the centre do not accrete significantly.

The requirements for competitive accretion to occur are the inefficient fragmentation that produces a large common reservoir of matter from which the protostars can accrete, and that this matter can move freely under the gravitational acceleration. The main difference between competitive accretion and the monolithic collapse scenario is the amount of matter that is accreted by the cores after the initial fragmentation. It is significantly higher than the initial core mass in the competitive accretion picture, and insignificant in the other.

### 1.1.4 Disk accretion

The development of an accretion disk probably circumvents the problem of the high radiative pressure: Radiation-driven bubbles that form above and below the disk and break up due to the Rayleigh-Taylor instability, as well as optically thin outflow cavities perpendicular to the disk, enhance the vertical transport of radiation [Krumholz *et al.*, 2005a,b]. These effects shift the previously derived boundary of about $40\,\mathrm{M}_\odot$ [Yorke and Sonnhalter, 2002], after which the accretion process becomes extremely inefficient, to higher masses.

### 1.1.5 The evolution of protostars at high accretion rates

Recent simulations of protostars undergoing accretion at high rates of $10^{-3}\,\mathrm{M}_\odot\,\mathrm{yr}^{-1}$ predicted a bloating by several tens of solar radii or more before they reach the main sequence [Hosokawa and Omukai, 2008; Yorke and Bodenheimer, 2008]. In the bloating phase, they develop high luminosities at low surface temperatures. The protostellar mass reaches $\sim 30\,\mathrm{M}_\odot$ before the protostar contracts and the central temperature increases, causing the hydrogen burning to begin (see Figure 1.3). Hence, these investigations underline the importance of the accretion history for the further development of the forming high-mass star.

## 1.2 Observations of high-mass star formation

All observational studies of high-mass formation face severe challenges because of the on average large distances to the candidate regions and the confusion of sources. Due to the rarity of high-mass stars and their short lifetimes (see Table 1.1), the number of accreting high-mass star precursors in the Milky Way is on the order of several thousand only [Zinnecker and Yorke, 2007, and references therein]. Within 1 kpc, there are only 17 star-forming regions known where high-mass stars are present or currently formed. The majority of the studied regions lies at distances of 2 kpc and beyond. The formation of high-mass stars appears to be intrinsically linked to the formation of associations and clusters. Therefore, high angular resolution is a prerequisite even for sketchy studies of high-mass star formation.

From an observational perspective, the route from cores to high-mass stars comprises the following steps [cf. Beuther *et al.*, 2007]:

1. Massive starless (or prestellar) cores
2. Massive cores that harbour accreting low- to intermediate-mass protostars (destined to become a high-mass star)

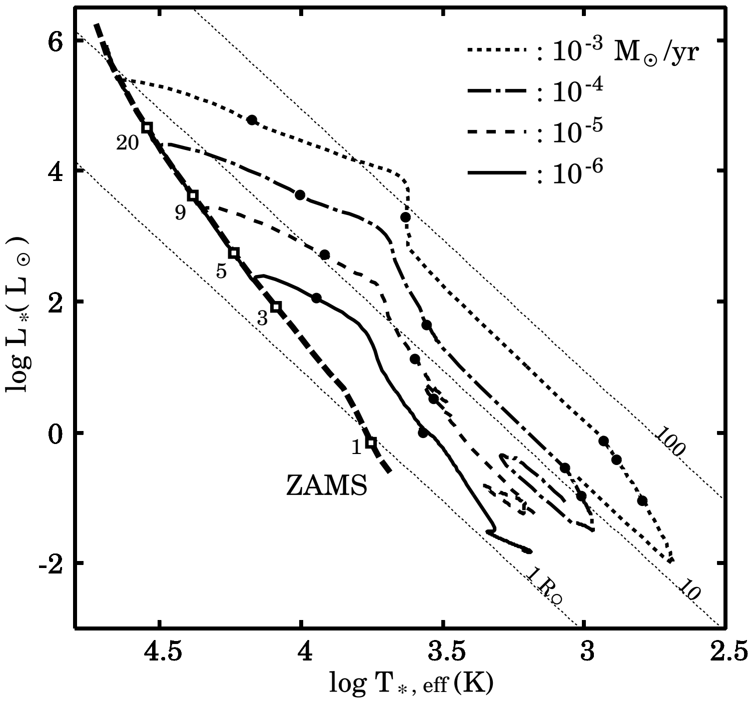

Figure 1.3: The evolution of the protostellar luminosity $L_*$ and surface temperature $T_{*,\mathrm{eff}}$ for different accretion rates between $10^{-6}$ and $10^{-3}\,M_\odot\,\mathrm{yr}^{-1}$ derived by Hosokawa and Omukai [2008]. Filled circles on the tracks represent protostellar masses of 1, 3, 5, 9, and $20\,M_\odot$, starting from the lower right. The thick dashed line shows the zero-age main sequence (ZAMS), and the open squares on it represent the same stellar masses as above. The dotted lines give the locations for constant stellar radii of 1, 10, and $100\,R_\odot$. Adopted from Hosokawa and Omukai [2008].

3. Accreting high-mass (proto-)stars ($M_\star \gtrsim 8\,M_\odot$), including also the phenomena of
    (a) Hot molecular cores
    (b) Hypercompact HII regions (size $< 0.01$ pc)
    (c) Ultracompact HII regions (size $< 0.1$ pc, accretion may have ceased)
4. Final stars

In studies of low-mass dense cores, a distinction is made between starless and prestellar cores [e.g. André *et al.*, 2008]: Prestellar cores are destined to form a central protostar, indicated by a centrally-concentrated density profile or even collapse motions, and they are self-gravitating. Starless cores do not show signatures of infall, and may even be transient, i.e. they eventually disperse without forming stars. They also comprise more pristine chemical signatures like e.g. the underabundance of molecules in the gas phase due to freeze-out on cold dust grains. Here, this distinction is not made for massive cores.

### 1.2.1 Accreting high-mass protostars

Many high-mass star formation studies targeted luminous infrared sources that can be assigned to the later stages, i.e. accreting high-mass protostars. Also the term high-mass protostellar objects is used. Among these, hot molecular cores have large masses of warm and dense gas and large abundances of complex organical molecules that evaporated off dust grains [Kurtz *et al.*, 2000]. Usually, methanol maser emission is associated. Embedded objects are present, but their ground-based detection in the mid-infrared is difficult [De Buizer *et al.*, 2002; Stecklum *et al.*, 2002] and relies on favouring orientations [Linz *et al.*, 2005].

Hypercompact and ultracompact HII regions show small patches of ionised gas surrounding protostellar objects that are still embedded [Keto and Wood, 2006]. Free-free emission from the ionised gas is detected at cm wavelengths. Hypercompact HII regions are often associated with water maser emission and probably trace individual photoevaporating disks. Hot molecular cores and hypercompact HII regions may coexist. Ultracompact HII regions [Churchwell, 2002] rather represent the photoionised envelopes and the accretion process may have ended at this stage.

Massive molecular outflows are ubiquitous in high-mass star-forming regions [Shepherd and Churchwell, 1996; Henning *et al.*, 2000b; Beuther *et al.*, 2002c; Wu *et al.*, 2004]. Furthermore, also collimated jet-like outflows exist at least temporarily, likely the outflow collimation widens with ongoing evolution. Collimated outflows strongly suggest that accretion disks are present, launching the outflows by magneto-hydrodynamics. However, the characteristics of these disks are poorly constrained because of the deep embedding. Nevertheless, kinematic signatures implying disk rotation have been traced for a number of sources.

### 1.2.2 Massive cores

The observational basis for the earlier phases, i.e. massive cores that could harbour accreting low- or intermediate-mass protostars, remains sparse. One of the reasons is the difficult identification of candidate sources: They should be faint in the near- and mid-infrared, and the large amount of cold material (below about 20 K) should lead to spectral energy distributions that peak in the far-infrared. This work focusses on sources selected using the far-infrared surveys of IRAS and ISO as described in the next chapter. Candidate sources have also been found by mapping the vicinity of more evolved objects [Sridharan *et al.*, 2005]. A different approach is the search for extinction features against the galactic mid-infrared background, first enabled by the surveys of ISO and MSX [Perault *et al.*, 1996; Egan *et al.*, 1998; Hennebelle *et al.*, 2001; Simon *et al.*, 2006]. More than $10^4$ infrared dark clouds have been identified with this method. These are generally cold molecular clouds, and amongst them are many massive and high-density regions, naturally promising candidate birthplaces for high-mass stars. Though they appear dark in the mid-infrared, they can harbour embedded sources detectable at longer wavelengths. Thus, the comprised cores are expected to represent various evolutionary stages from starless cores to accreting high-mass protostars.

Although representing the important earliest stage in the evolution, the massive starless cores remained hypothetical up to now. Their properties set the initial conditions for high-mass star formation and determine the involved timescales. The question how long they exist and how fast they evolve [Krumholz and Tan, 2007; Elmegreen, 2007] is not answered yet. Thus, the search for such objects remains a crucial task to gain further insight and evaluate the outlined evolutionary sequence. Altogether, only a relatively small number of candidate sources that resulted from the described strategies have been investigated in depth [recently e.g. Beuther and Steinacker, 2007; Rathborne *et al.*, 2007; Birkmann *et al.*, 2007]. By now, the statistical database is insufficient to estimate the evolutionary timescales, and all detailed studies have found evidence for embedded star-forming activity.

Less detailed studies using large-scale maps of whole cloud complexes are underway, but have so far also failed to trace massive starless cores. The results suggest that the lifetimes of these are very short, on the order of $10^3$ yr only [Motte *et al.*, 2007].

## 1.3 Motivation and outline of this thesis

From these theoretical considerations and observational findings it becomes clear that the earliest stages in the formation of high-mass stars are not well-characterised yet. This also results from a lack of well-studied representative sources. Again from an observational perspective, the following non-exhaustive set of questions remains to be answered:

- What is the structure of massive clumps, and how do they fragment?
- Do massive starless cores exist and what are their properties?
- How do massive cores evolve before the hot molecular core stage?
- What are the accretion rates of forming high-mass stars?

This work addresses these aspects by investigating a sample of massive and cold star-forming regions. They have been identified using the ISO Serendipity Survey that is introduced in the second chapter. Observations at multiple wavelengths from the optical to the millimetre regimes are evaluated to characterise their detailed star-forming content. Chapter 3 describes a study of five ISOSS star-forming regions. Several massive clumps were revealed in which the star-forming process has initiated. In Chapter 4, a detailed case study of the ISOSS J18364-0221 SMM1 clump is presented. This clump comprises two star-forming cores at very early stages. Chapter 5 explores mid-infrared spectroscopic observations of several previously identified clumps in ISOSS regions. In the subsequent Chapter 6, the derived results are discussed with respect to the initial phases of high-mass star formation. The detail to which the selected sources can be studied is limited by the provided angular resolutions and sensitivities. In particular the infrared regime remains crucial for further insights. In this respect, the future space-based observatories will allow major breakthroughs. In Chapter 7, the upcoming observations with the Herschel Space Observatory are outlined and their anticipated impact on high-mass star formation research. Chapter 8 addresses the prospects of using the Mid-Infrared Instrument aboard the James Webb Space Telescope by means of two example studies. In addition, recently achieved results of instrument level tests are presented that allowed to demonstrate and validate several crucial instrument characteristics for the first time. Finally, the conclusions drawn from this thesis are summarised in Chapter 9 and an outlook on aspects to be addressed in future work is given.

# Chapter 2

# The ISOSS sample of massive star-forming regions

## 2.1 The ISOPHOT Serendipity Survey

The European Infrared Space Observatory (ISO) mission [Kessler *et al.*, 1996] was operative in the years 1995 to 1998 and observed in the wavelength range of 2.5 to 240 $\mu$m. While the primary missions of the preceeding IRAS [Neugebauer *et al.*, 1984] and COBE [with its DIRBE instrument, Boggess *et al.*, 1992; Silverberg *et al.*, 1993] far-infrared astronomical satellites were sky surveys, ISO provided an infrared observatory allowing pointed observations towards individual sources at increased angular resolution and high sensitivity. The ISO telescope consisted of a Ritchey-Chrétien system with a 60 cm mirror (f/15) included in a cryostat and cooled to 3 K. Due to the excellent thermal properties of the satellite, the mission duration was prolonged by 11 months and reached 29 months. ISO carried four scientific instruments including the imaging photopolarimeter ISOPHOT [Lemke *et al.*, 1996], developed by a scientific consortium under the leadership of the Max-Planck-Institut für Astronomie (PI D. Lemke), and built by an industrial consortium. ISOPHOT provided spectrophotometric, polarimetric and imaging photometric observations, thereby accounting for the large ISO wavelength range. The detector at the longest wavelengths was the C200 camera with its $2 \times 2$ array of stressed Ge:Ga crystals pushing the sensitivity wavelength range to 240 $\mu$m. The array was cooled down to 1.8 K using superfluid helium. Out of the five available filters, the 170 $\mu$m filter (89 $\mu$m equivalent width) was selected for the ISOPHOT Serendipity Survey (ISOSS). As described in Bogun *et al.* [1996] and Stickel *et al.* [1998], this survey used the satellite slew time between ISO's pointed observations and effectively increased the overall observing efficiency. Because the slews of the observatory depended on the sequence of pointings and on the avoidance of the strongest heat sources in the sky (Sun, Moon, Earth), they could not be predicted in detail. This led to an almost unbiased sky coverage of about 15% from a total observing time of 550 h. Redundant information from slew crossings have been used to improve the photometric accuracy and reproducibility by applying a self-consistent cross-calibration, also taking into account the zodiacal light brightness [Reach, 2000], and the ISOSS 170 $\mu$m Sky Atlas has been compiled [Stickel *et al.*, 2007b]. The ISOSS provided the first infrared survey at high angular resolution beyond the IRAS 100$\mu$m limit. It achieved a comparable angular resolution of $1.5'$ (FWHM) as well as a comparable point source sensitivity of 1 Jy at the longer wavelength. Figure 2.1 shows an example map extracted from the ISOSS Sky Atlas.

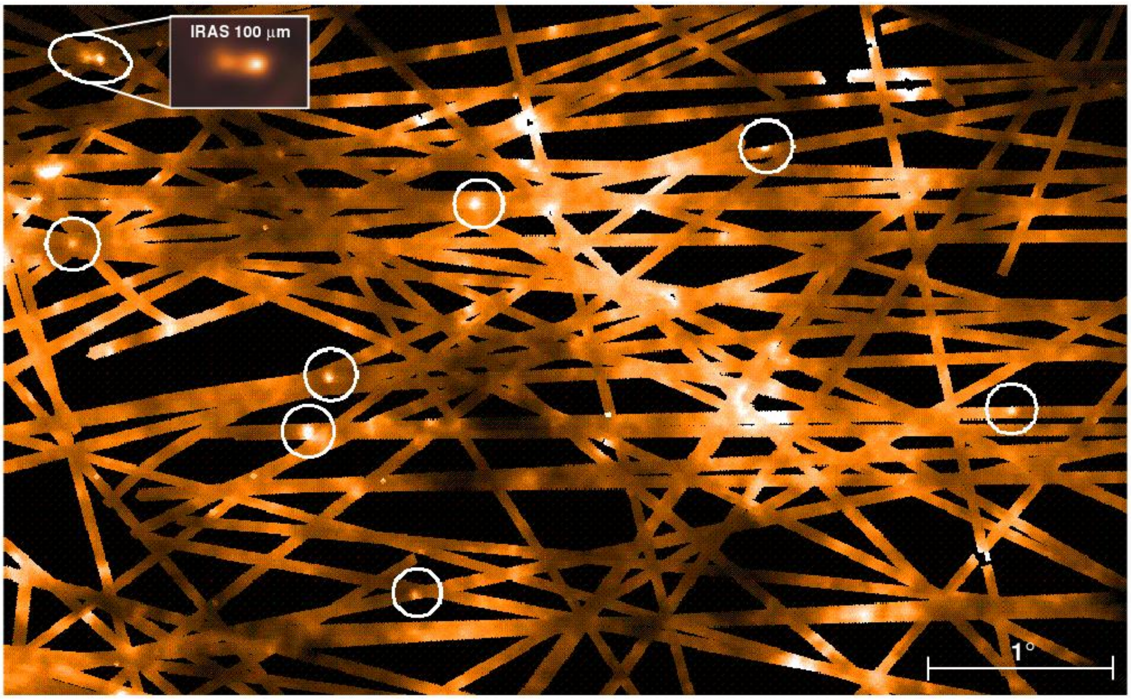

Figure 2.1: Example map from the ISOSS 170 $\mu$m Sky Atlas. The surface brightness scales from 150 to 500 MJy/sr; the angular scale is given in the lower right. Objects from the compact sources database are encircled. The comparison of two adjacent point sources in the upper left with the respective IRAS 100 $\mu$m HIRES map demonstrates the similar angular resolution. Adopted from Krause [2003].

### 2.1.1 Scientific exploitation of the ISOSS

An important scientific return of the ISOSS is the statistical investigation of far-infrared properties of galaxies [Stickel *et al.*, 2007a]. A catalogue of more than 1900 optically identified galaxies with 170 $\mu$m flux measurements has been compiled in Stickel *et al.* [2004] that covers a wide variety of morphological types, flux levels, and redshifts. For a large sample the far-infrared luminosities, dust temperatures and morphologies, and HI-to-dust ratios were established.

Furthermore, the ISOSS allowed to localise and characterise the coldest interstellar clouds in terms of average dust temperature $\mathrm{T_d}$ [Hotzel, 2001]. The Taurus and Cepheus Flare regions contain many sources with $\mathrm{T_d} \approx 12\,\mathrm{K}$, some of them were found in the Chamaeleon and Ophiuchus regions, whereas towards the Cygnus, Cepheus, and Orion regions only warmer sources with $\mathrm{T_d} > 25\,\mathrm{K}$ were detected. The good correlation between the optical extinction and the 170 $\mu$m surface brightness indicates that the latter traces the dust column density very well.

Towards the supernova remnant Cassiopeia A, a large area of $40' \times 80'$ is well-covered in the ISOSS Sky Atlas. In combination with subsequent observations, this enabled to clarify that the ejecta of the remnant do not carry plenty of cold dust [Krause *et al.*, 2004a]. Therefore this object does not support the perception that type II supernovae are producing large amounts of dust.

## 2.2 The selection of cold and massive star-forming regions

The thermal emission arising from cold aggregates of dust peaks in the far-infrared, and therefore this wavelength regime is well-suited to search for the initial stages of star formation. The bands observed by IRAS at 12, 25, 60 and 100 $\mu$m and the resulting point source catalogues [Beichman *et al.*, 1988] allowed to derive far-infrared flux ratios and colour-colour diagrams that have been used to select candidate young star-forming objects. In combination with the IRAS measurements, the ISOSS permitted to extend this method to the 170 $\mu$m band. Krause [2003] and Krause *et al.* [2004b] have applied the following selection criteria to identify the ISOSS star-forming regions:

1. Compact ISOSS source: FWHM between $1.2'$ and $3.5'$, detected by all four camera pixels with a signal-to-noise ratio above 5
2. Associated IRAS 100 $\mu$m point source within $3'$ distance
3. Associated molecular gas emission in the lines $^{12}$CO(1-0), $^{13}$CO(1-0) or CS(2-1) within $3'$ distance

The first criterion constrained the size of the region to below 5 pc at distances up to 5 kpc, assuming a typical size of molecular gas aggregates. In order to enhance the reliability of the catalogue, determine flux ratios, and select cold cores, the second criterion demanded that IRAS measurements are available. The third criterion prevented contamination by interstellar cirrus, which presents a major source of confusion because of its low temperature around 18 K. In addition, the radial velocities determined using the molecular line emission provided kinematical distances according to the galactic rotation model of Brand and Blitz [1993]. As a result, a list of 193 sources has been identified that exhibit a far-infrared luminosity above 100 $L_\odot$ or a total mass above 100 $M_\odot$ [Krause *et al.*, 2004b].

With the ISOSS 170 $\mu$m data a lower temperature range is explored compared to previous studies: 70% of the objects exhibit a far-infrared colour temperature of 20 K and lower. These cold average dust temperatures have been confirmed also for the gaseous component towards a subsample of 35 objects using ammonia observations. Wood and Churchwell [1989] first used IRAS colours to find UCHII regions and defined colour criteria of $[60-12] \geq 1.3$ and $[25-12] \geq 0.57$. These thresholds select thermal dust components at temperatures up to 100 K (not corrected for the dust emissivity). With additional criteria, presumed precursors to UCHII regions have been selected by e.g. Henning *et al.* [1990]; Palla *et al.* [1993]; Sridharan *et al.* [2002]. Their samples mostly contain luminous sources ($L > 1000\,L_\odot$) and the average dust temperatures usually lie above 30 K.

The mass-to-luminosity ratio of the coldest ISOSS objects ($T < 18$ K) is about $0.6\,M_\odot/L_\odot$ and also exceeds the values for the other samples. This renders these sources a promising target sample to study the early phases of star-formation that arise in cold and massive regions.

## 2.3 Previous studies of ISOSS star-forming regions

The measurements from ISO and IRAS assessed the global properties of the identified regions on scales of the beam sizes (about $1.5'$) in the far-infrared wavelength regime. To characterise the star-forming content of the identified regions in detail, follow-up observations providing increased spatial resolution and additional coverage of the spectral energy distributions have been conducted previous to and in the course of this work. An overview covering most observations is given in Birkmann [2007], and further properties of a large sample of ISOSS regions are presented there. In the following, these previous results are summarised.

Independent estimates of the hydrogen column densities and total masses in 99 ISOSS regions have been derived using CO(3-2) molecular line emission maps. The maps provide an angular resolution of about 20″. The uncertainty in the conversion to hydrogen column densities is about a factor of 3. In addition, the kinematical distances were refined. In Figure 2.2 the resulting distributions are shown for the 99 regions. Most regions lie at distances between 2 and 6 kpc. The hydrogen column density distribution peaks at $10^{22}\,\mathrm{cm}^{-2}$, and the mass distribution peaks around $1000\,\mathrm{M}_\odot$.

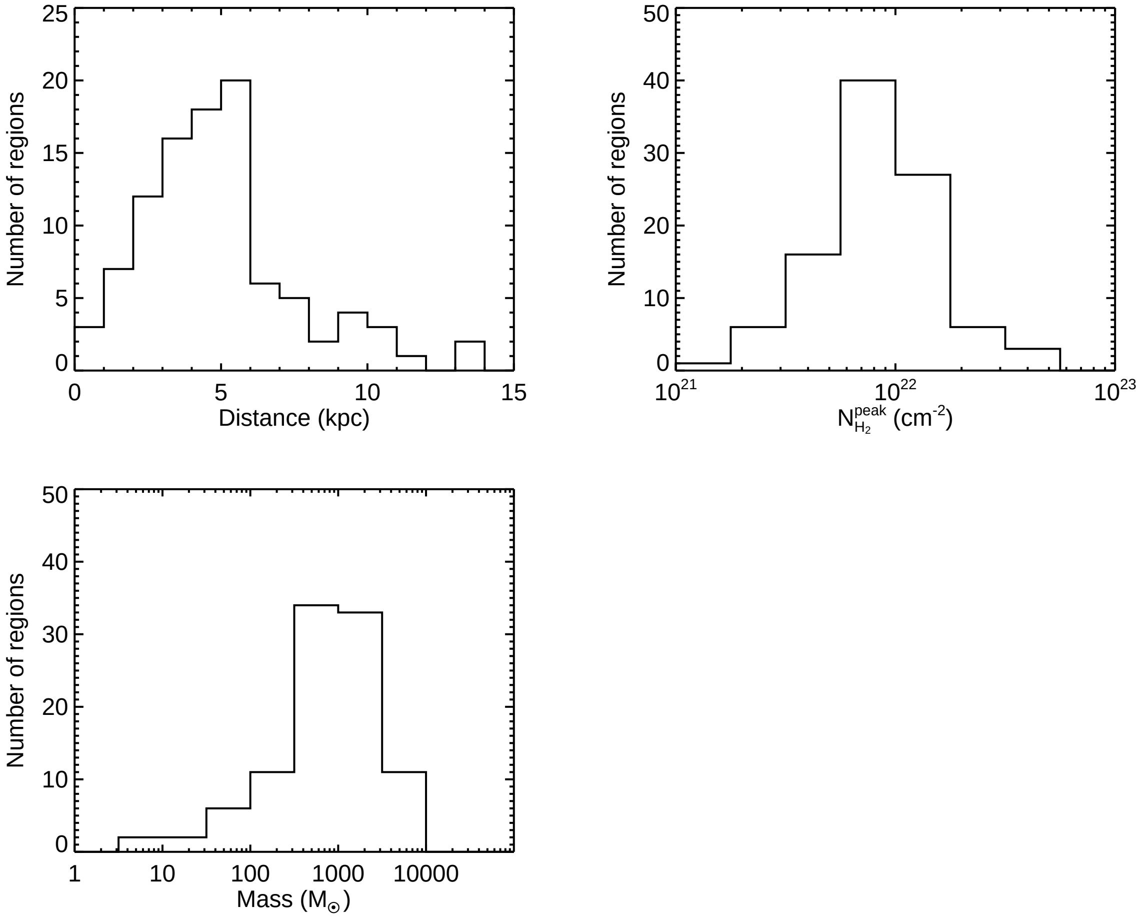

Figure 2.2: The distribution of distances, peak hydrogen column densities, and masses of 99 ISOSS star-forming regions derived from the CO(3-2) emission.

From near-infrared images extinction maps were created using the NICER method [Lombardi and Alves, 2001]. In principle, the extinction maps provide additional mass estimates and explore the morphological structure of molecular cloud complexes. However, the compactness of the ISOSS sources and the high column densities beyond $A_V = 100$ mag towards the dense clumps did not allow to derive meaningful mass estimates.

Several other molecular transitions in the (sub-)millimetre have been observed for a subsample of 17 ISOSS regions. In particular, the measurements of the dense gas tracers CS, $N_2H^+$, and HCN indicate that the regions contain gas components with $n_{H_2} \geq 10^6\,\mathrm{cm}^{-3}$. Furthermore, the kinematics of the gas components could be assessed via the profiles of optically thick lines. Towards several clumps in ISOSS regions, the $HCO^+$(3-2) line profiles show red-shifted self-absorption that indicates collapse motions. Approximately one third of the studied clumps belong to this group. However, observations with high angular resolution are neccessary to explore the clump dynamics in detail, because e.g. outflow phenomena influence the line profiles. One such study is presented in Chapter 4. The following sections describe the previous case studies of individual ISOSS regions.

### 2.3.1 ISOSS J20208+3559

This region was studied initially by Krause *et al.* [2003] where follow-up observations in the optical, mid-infrared, (sub-)millimetre and in the $NH_3$ radio line emission have been evaluated. This region is associated with an optical dark cloud complex with a total mass of 760 $M_\odot$ at a distance of 1.8±0.3 kpc, and is connected to the Cygnus-X Giant Molecular Cloud. Traced by the ISO and IRAS measurements, the dense inner region of the central dark cloud contains 120 $M_\odot$ of gas and dust at an average temperature of 16 K. Two candidate Class 0 objects SMM1 and SMM3 with masses of 8 and 3.5 $M_\odot$ were identified and are possibly intermediate-mass star precursors. The dust temperature of the central clump of 50 $M_\odot$ drops to 11 K in its centre, and the clump is gravitationally bound as derived from $NH_3$ observations. This makes it a candidate massive prestellar clump. In the vicinity, a Herbig B2 star was identified and constitutes the most luminous object. Its mass is 6.5 $M_\odot$ and it exhibits a luminosity of 2200 $L_\odot$. Ongoing accretion on this source is implied by inverse P Cygni line profiles in the higher HI Balmer series and SiII. The SED is reproduced by a Kurucz stellar photosphere model and an optically thick, geometrically thin accretion disk. The stellar age is less than 40000 yr according to pre-main-sequence evolutionary tracks. Besides, several embedded near-infrared sources were found, and one is associated with a mid-infrared reflection nebula. Using stellar masses derived from the near-infrared magnitudes, the star formation efficiency in the central region is estimated to 14%.

These results indicate that the low average dust temperatures derived using ISO trace the cold gas and dust components that dominate in terms of mass. However, the presence of young stellar objects show that star formation is ongoing, and in this region, it already produced an intermediate-mass star. Using additional data, this region is further discussed in Chapter 3.

### 2.3.2 ISOSS J18364-0221

Initially presented by Birkmann *et al.* [2006], this region lies at a distance of about 2.2 kpc in the centre of an extended dark cloud complex. Observations in the near-infrared, submillimetre, and of $NH_3$, $C^{(18)}O$(2-1) and (3-2), and $H^{(13)}CO^+$(3-2) molecular lines have been accomplished. The whole complex has a mass of ca. 3200 $M_\odot$, and the embedded star-forming region comprises around 900 $M_\odot$ traced by thermal dust emission at 15 K and exhibits a luminosity of around 800 $L_\odot$. Two massive clumps were identified in the submillimetre. The eastern, compact 75 $M_\odot$ clump SMM1 shows infall signature and outflow activity and is considered a candidate high-mass star-forming clump. This clump is studied in more detail in Chapter 4. The western, more extended (radius $\approx$ 0.5 pc) SMM2 clump of 280 $M_\odot$ has very cold gas and dust temperatures of 12 K and presumably is Jeans unstable. The association of two low-mass young stellar objects indicates that fragmentation and cluster formation has started in this clump. It may represent the initial conditions for high-mass star formation, and similar to low-mass cores, it shows very low temperatures and low levels of turbulence.

### 2.3.3 ISOSS J23053+5953

Towards this region, Birkmann *et al.* [2007] evaluated near-infrared, *Spitzer* mid- to far-infrared and (sub-)millimetre data including molecular lines and interferometry. Located at a distance of about 3.5 kpc, its mass is similar to ISOSS J18374-0221 (around $900\,M_\odot$), while this region exhibits a higher luminosity of $2100\,L_\odot$. Two clumps SMM1 and SMM2 were identified, both of about $200\,M_\odot$, and more than 99% of the material is at a cold temperature of below 20 K, also in agreement with $NH_3$ measurements. Towards the clumps, a high $H_2$ density of $10^6\,cm^{-3}$ was traced by methanol lines, and the kinetic temperatures of formaldehyde of ca. 40 K support the presence of a dense and warm region. At the high spatial resolution of the interferometric maps, the SMM1 clump is resolved in 2 to 3 components. SMM2 appears to host a very compact core ($9000\times6000$ AU) and the filtered flux measurement give a mass of $26\,M_\odot$. An associated molecular outflow is detected and infall signature is present towards this core. It probably represents a young massive protostellar core, and the embedded protostar of $2\,M_\odot$ or more presumably accretes at a high rate.

This study also supports that the cold gas and dust component, traced by the ISOSS and IRAS measurements, and initially selected by the criteria described in the previous section, dominates the mass of the region. Nevertheless, a fraction of the material is actively converted to stars, and in this case a candidate high-mass star precursor in an early evolutionary stage, of which only few examples are known, was identified. This again implies the connection of the cold and massive regions with the origin of high-mass stars and clusters.

### 2.3.4 Prospects of further studies

The encouraging previous results motivate further studies of the ISOSS star-forming regions. At first, the results provide evidence that the selected regions harbour massive clumps at the onset of star formation, and thus allow to explore these sparsely found objects. Secondly, the addition of recently available infrared observations with *Spitzer* allows to characterise the cold dust components that are traced by the ISO and IRAS measurements on smaller scales. They also reveal embedded objects and thereby place more stringent constraints on the regions' star-forming content than previously possible. It is necessary to enlarge the sample of well-studied regions to establish a better statistical basis and to asses the overall suitability of surveys in the far-infrared for the search of early-stage high-mass star formation. The global properties derived for a sample of sources greatly aid the selection of individual regions for more detailed studies. However, as shown for the region ISOSS J23053+5953, the identification of individual massive cores requires observations at high angular resolution. These prospects drove the studies presented in the following chapters.

# Chapter 3

# An infrared-submillimetre study of five ISOSS regions

## 3.1 Motivation and outline

In this chapter, observations of four ISOSS star-forming regions are reported and the study of ISOSS J20298+3559 is extended. The observed regions are listed in Table 3.1. Continuum observations with high spatial resolution covering the submillimetre to near-infrared wavelength range allow to characterise the detailed star-forming content. In the submillimetre the thermal dust emission is traced and compact condensations were identified. To constrain their evolutionary stage, mid- and far-infrared observations using *Spitzer* were conducted. The long-wavelength data in the far-infrared and submillimetre was used to estimate the dust temperatures and total masses of the clumps. The sensitive mid-infrared data also reveals very young associated stellar objects. Additional deep near-infrared images provide a good assessment of source confusion. For the detected young stellar objects (YSOs), an evolutionary classification from their infrared colours was performed. In Section 3.7, a subset was then characterised using radiative transfer models.

| Region ISOSS… | Assoc. IRAS point source | RA/DEC (J2000) | Distance[a] (kpc) | $T_{\mathrm{FIR\,colour}}$[b] (K) | $F_{170\,\mu\mathrm{m}}$ (Jy) |
|---|---|---|---|---|---|
| J19357+1950 | 19335+1944 | 19:35:45.9 +19:50:58 | 4.0 | 17.5 | 98.8 |
| J19486+2556 | 19465+2549 | 19:48:36.8 +25:56:55 | 2.9 | 18.0 | 54.8 |
| J20153+3453 | 20134+3444 | 20:15:20.9 +34:53:53 | 2.0 | 19.0 | 182 |
| J20298+3559 | 20278+3549 | 20:29:48.3 +35:59:24 | 1.8 | 16.0 | 171 |
| J22478+6357 | 22460+6341 | 22:47:54.1 +63:57:11 | 4.1 | 15.4 | 136 |

[a] Kinematic distances were obtained using the galactic rotation model of Brand and Blitz [1993] and identification of kinematically associated molecular cloud complexes [Krause, 2003].

[b] $T_{\mathrm{FIR\,colour}}$ was derived from the far-infrared flux ratios at 100 $\mu$m (IRAS) and 170 $\mu$m (ISOSS).

Table 3.1: Observed ISOSS star-forming regions.

## 3.2 Observations, data reduction, and analysis

### 3.2.1 Submillimetre continuum emission

Submillimetre continuum jiggle maps at 450 $\mu$m and 850 $\mu$m were obtained with SCUBA [Holland *et al.*, 1999] at the James Clerk Maxwell Telescope (JCMT) in July 2001 and May 2003 under good atmospheric transmission conditions ($\tau_{850\,\mu\mathrm{m}} \lesssim 0.2$). Data reduction used the ORAC-DR [Jenness and Economou, 1999] and SURF [Jenness and Lightfoot, 1998] software. The photometric calibration was based on maps of Uranus acquired shortly before or after the observations. Further analysis used the MIRIAD [Sault *et al.*, 1995] software package and followed the procedure described in Sandell and Weintraub [2001]. To account for the deviations in the JCMT beam from a single Gaussian, the Uranus maps were used to construct symmetric beam models and deconvolve the maps of the target regions. The derived beam sizes are 7.8 – 8.8″ at 450 $\mu$m and 14.7 – 15.1″ at 850 $\mu$m. The maps were then restored using Gaussians of 8″ and 14″, respectively. By fitting Gaussian components to the restored maps, submillimetre continuum fluxes and deconvolved source sizes at 450 $\mu$m were derived first. Then these sizes, convolved with the 14″ Gaussian, were used to extract 850 $\mu$m fluxes in order to only include emission from the same regions. The photometric accuracy is estimated to be 30% at 450 $\mu$m and 20% at 850 $\mu$m, and the pointing uncertainty of the submillimetre maps is 2″ rms.

### 3.2.2 Near-infrared emission

Near-infrared images in J, H, and Ks were taken with the Calar Alto 3.5 m telescope using the two prime focus wide-field cameras Omega2000 [Baumeister *et al.*, 2003] and OmegaPrime [Bizenberger *et al.*, 1998]. Omega2000 features a field of view (FOV) of $15.4 \times 15.4\,\mathrm{arcmin}^2$ with a pixel scale of $0.4496''\,\mathrm{pix}^{-1}$, while the FOV for OmegaPrime is $6.8 \times 6.8\,\mathrm{arcmin}^2$ with a pixel scale of $\sim 0.4''\,\mathrm{pix}^{-1}$. The exposure time in the broad band filters was 20 minutes each. The exposures were dithered on source to allow for sky subtraction. The reduction and photometry was done with IRAF [Tody, 1993] and GAIA[1], and the photometric calibration for J, H, and Ks is based on the 2MASS point source catalogue.

### 3.2.3 Mid- and far-infrared emission

The *Spitzer* [Werner *et al.*, 2004] observations included IRAC [Fazio *et al.*, 2004] imaging in all four photometric bands, MIPS [Rieke *et al.*, 2004] imaging at 24 $\mu$m and 70 $\mu$m and the MIPS spectral energy distribution (SED) mode. For the imaging observations, the basic flux-calibrated data (BCD) of the *Spitzer Science Center* (SSC) pipeline was used for further data reduction and analysis. The calibration uncertainties of the data are about 2% for IRAC [Reach *et al.*, 2005], 4% for MIPS 24 $\mu$m [Engelbracht *et al.*, 2007], and 10% for MIPS 70 $\mu$m [Gordon *et al.*, 2007]. Cosmetic corrections and astrometric refinement were performed with the MOPEX software [Makovoz and Marleau, 2005], and final images were combined using scripts in IRAF. Aperture photometry and PSF fitting was done with the aperture corrections given on the SSC website[2]. The MIPS SED mode calibration is based on a spectrum of $\alpha$ Boo [Low *et al.*, 2005] and the measured MIPS 70 $\mu$m fluxes. The resulting photometric accuracy is estimated to be 5% (IRAC), 10% (MIPS 24), and 20% (MIPS 70 and SED).

---

[1] http://star-www.dur.ac.uk/~pdraper/gaia/gaia.html

[2] http://ssc.spitzer.caltech.edu

## 3.3 Submillimetre emission morphology and associated mid-infrared sources

The five ISOSS regions listed in Table 3.1 are displayed in Figures 3.1 to 3.3. In the following, their individual submillimetre morphologies are described and the associated $24\,\mu$m sources are pointed out. On the IRAC and near-infrared maps, those sources are marked for which singular counterparts can be identified at shorter wavelengths.

### 3.3.1 ISOSS J19357+1950

In this region three submillimetre emission components are resolved at $450\,\mu$m, two adjacent parts (SMM1 North and South) and a southwestern part (SMM2) (left panels in Figure 3.1). They have deconvolved FWHM sizes of about $19''$, $16''$, and $20''$, which correspond to $0.31 - 0.39$ pc. An arc-shaped extended emission feature that stretches from southeast to northwest is visible at $24\,\mu$m. Two $24\,\mu$m point sources are detected associated with SMM1 North. For SMM1 South and SMM2 one and two sources are present. Both SMM1 North and South are also coincident with emission at $70\,\mu$m but are not resolved individually. At the location of SMM2, no distinct $70\,\mu$m feature is detected.

### 3.3.2 ISOSS J19486+2556

Three submillimetre clumps are detected in this region. They are located along a chain from northeast to southwest and termed SMM1 to SMM3 (right panels in Figure 3.1). All three appear compact in the submillimetre: The deconvolved FWHM diameters are about $16''$ (SMM1), $10''$ (SMM2) and $15''$ (SMM3) at $450\,\mu$m. The corresponding length scales are 0.14 to 0.22 pc. Both SMM2 and SMM3 are associated with bright 24 and $70\,\mu$m sources. In the case of SMM2, several objects are detected at $24\,\mu$m, and the brightest one coincides with the submillimetre peak, as well as with the $70\,\mu$m source. For SMM3, one source at 24 and $70\,\mu$m is located at the submillimetre peak. In addition, two areas of extended 24 and $70\,\mu$m emission are found, one southeast of SMM2 and a second one towards the southern rim of SMM3. The first one is not associated with submillimetre emission. Only a faint source at $24\,\mu$m is detected towards the centre of SMM1 and it is not associated with compact $70\,\mu$m emission.

### 3.3.3 ISOSS J20153+3453

This region contains a single submillimetre clump clearly detected in both SCUBA bands (left panels in Figure 3.2). The deconvolved $450\,\mu$m FWHM extension is about $18'' \times 14''$, i.e., the projected diameter of the clump is around 0.16 pc. In the $24\,\mu$m band, two point-like sources surrounded by extended emission are detected towards the northwestern limb of the submillimetre clump. The brighter one is located among a cluster of sources seen at shorter wavelengths. None of these are resolved individually at $70\,\mu$m, but they instead blend into a single slightly extended source. The submillimetre emission peak is offset from the brighter point source by $11''$.

### 3.3.4 ISOSS J20298+3559

This region has been studied in detail in Krause *et al.* [2003]. Four submillimetre emission peaks are found in this region. Two of them are joined by extended emission (SMM1 and SMM2), while SMM3 and SMM4 are offset to the west (right panels in Figure 3.2). SMM4 was not discussed in Krause *et al.* [2003]. The sizes of the clumps SMM1 and

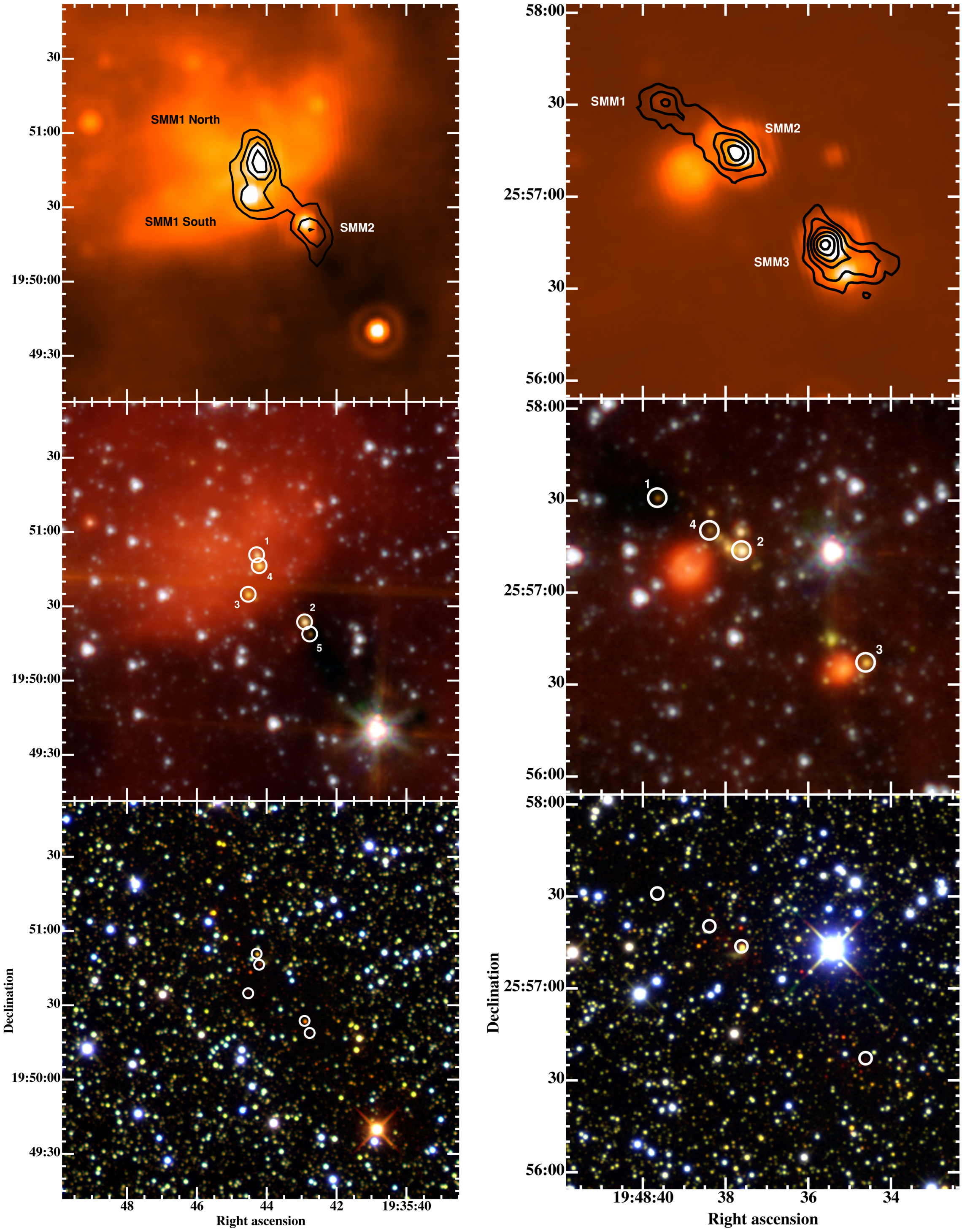

Figure 3.1: Observations of the regions ISOSS J19357+1950 (left) and J19486+2556 (right). The upper panels show the 24 $\mu$m maps and the overlaid contours show the SCUBA 450 $\mu$m emission. The mid panels show colour composites of the IRAC images. The bottom panels are JHKs colour composites using OmegaPrime and Omega2000 observations. The circles surround the sources investigated in the Analysis section.

SMM3 are approximately 0.14 and 0.17 pc, SMM2 is unresolved ($< 0.07$ pc), and SMM4 is more extended. The deconvolved FWHM diameter is roughly $39''$ corresponding to 0.34 pc. SMM1, SMM2, and SMM4 are associated with emission at 70 $\mu$m, and SMM3 was not covered by our 70 $\mu$m maps. Two 24 $\mu$m point sources are detected towards SMM2 and one towards SMM4. Both SMM1 and SMM3 have faint counterparts at 24 $\mu$m.

### 3.3.5 ISOSS J22478+6357

The submillimetre emission in this region traces an elongated clump (SMM1) that is resolved in both an eastern and a western component at 450 $\mu$m (Fig. 3.3). The deconvolved 450 $\mu$m FWHM extensions of these are $\sim 7''$ and $\sim 12''$, corresponding to roughly 0.14 and 0.24 pc. At 24 $\mu$m, several point sources are associated. The brightest are located at the eastern and to the southern limb of the western submillimetre peaks. The 70 $\mu$m map reveals emission that coincides with the submillimetre peaks and with the 24 $\mu$m sources.

## 3.4 Spectral energy distributions and dust temperatures

First, the analysis of the long-wavelength observations towards the star-forming regions are presented. Then, the associated infrared sources are addressed. The extracted fluxes in the far-infrared and submillimetre are listed in Table 3.2. In Figures 3.4, 3.5, and 3.6 the spectral energy distributions (SEDs) of the detected clumps are sketched.

### 3.4.1 Far-infrared spectral slopes

The examination of the SEDs compiled for the seven detected clumps towards which MIPS SED observations were performed showed that the spectral slopes at wavelengths around 70 $\mu$m and below do not resemble a single thermal emission component that would reproduce the submillimetre fluxes. It presumably stems from warmer dust components or transiently heated very small grains [cf. Birkmann *et al.*, 2007; Rawlings *et al.*, 2005]. The spectral slopes ($\mathrm{d}\log(\lambda \mathrm{F}_\lambda)/\mathrm{d}\log\lambda$) vary in the range $0.3 - 2.0$ for $70\,\mu\mathrm{m} < \lambda < 94\,\mu\mathrm{m}$.

### 3.4.2 Clump dust temperatures and masses

The characterisation of the cold component of dust (and gas) that gives rise to the emission at long wavelengths assumed that it can be reproduced by isothermal dust emission. As noted above, the fluxes at wavelengths around 70 $\mu$m and below do not conform to this assumption, so the datapoints at 93, 450, and 850 $\mu$m were used to estimate the dust temperature. In that respect, it was also assumed that the emission at these wavelengths is optically thin and can be approximated by a modified Planck spectrum. The dust opacities given in Ossenkopf and Henning [1994] were used. Among the different models, a MRN distribution either without ice mantles, with thin and with thick ice mantles ($\kappa_{850\mu\mathrm{m}} = 0.6 - 1.4\,\mathrm{cm}^2/\mathrm{g}$) corresponding to emissivity indices of $\beta = 1.81 - 1.85$ at long wavelengths were applied. The dust-to-gas mass ratio was assumed to be 1/100. In the cases where no MIPS SED measurements are available, the 70 $\mu$m flux was extrapolated to 93 $\mu$m, allowing for spectral slopes of 0.3 and 2.0 (adopting the measured extremes). The resulting range of dust temperatures and gas masses for each clump are listed in Table 3.2. The fitted curves are shown in Figures 3.4, 3.5, and 3.6.

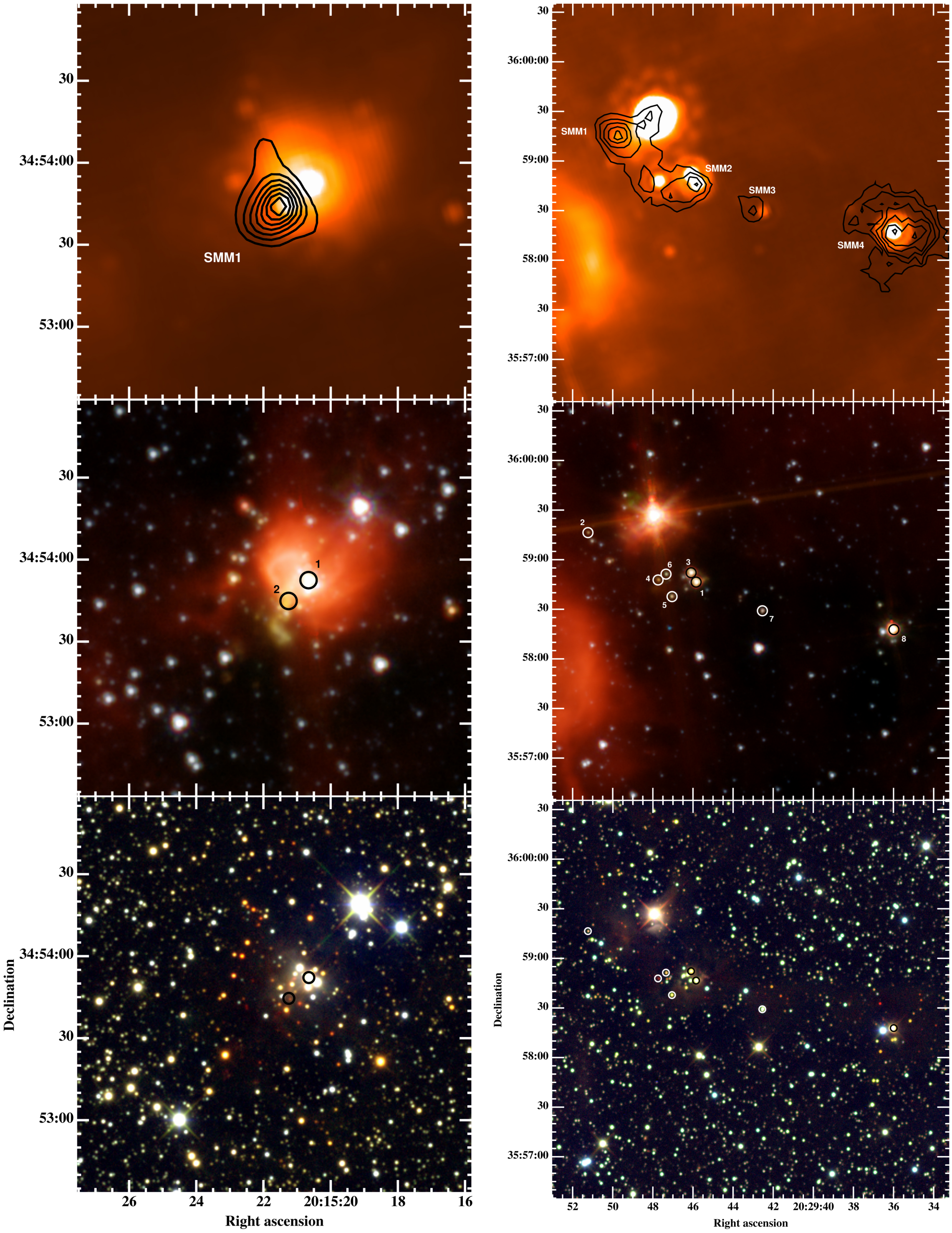

Figure 3.2: Observations of the regions ISOSS J20153+3453 (left) and J20298+3559 (right). Same arrangement and symbols as in Figure 3.1, except that the contours for ISOSS J20298+3559 SMM3 show the 850 $\mu$m emission.

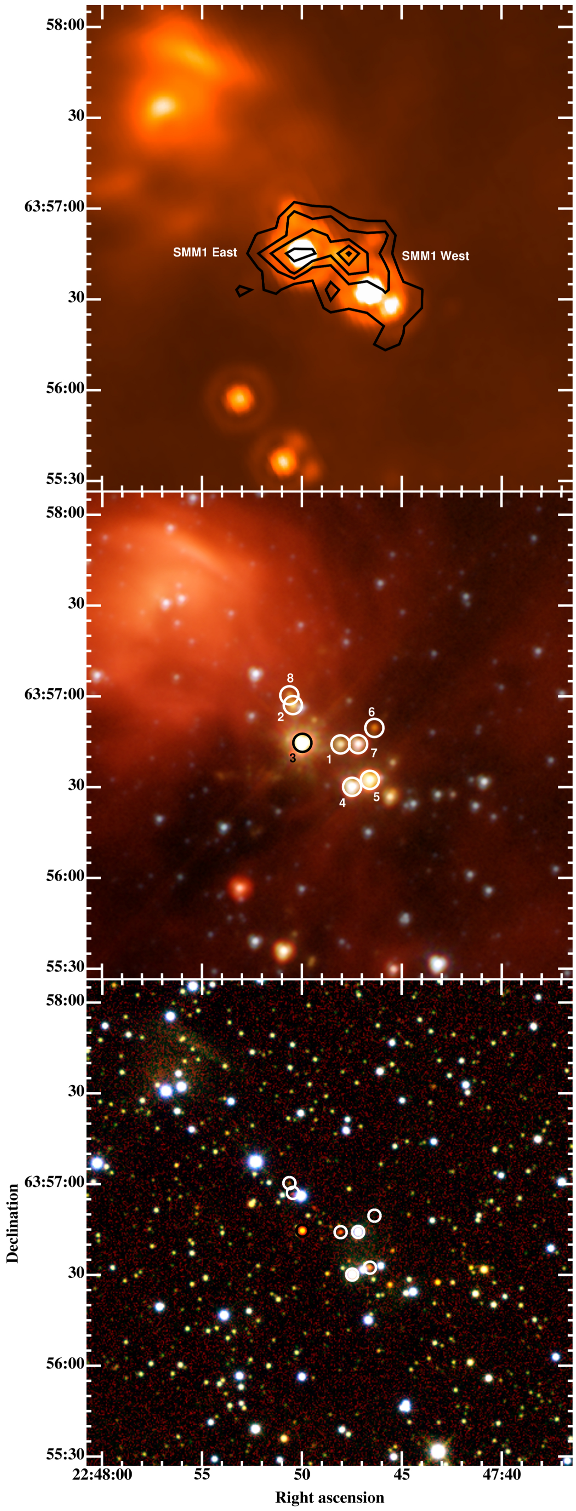

Figure 3.3: Observations of the region ISOSS J22478+6357. Same arrangement and symbols as in Fig. 3.1.

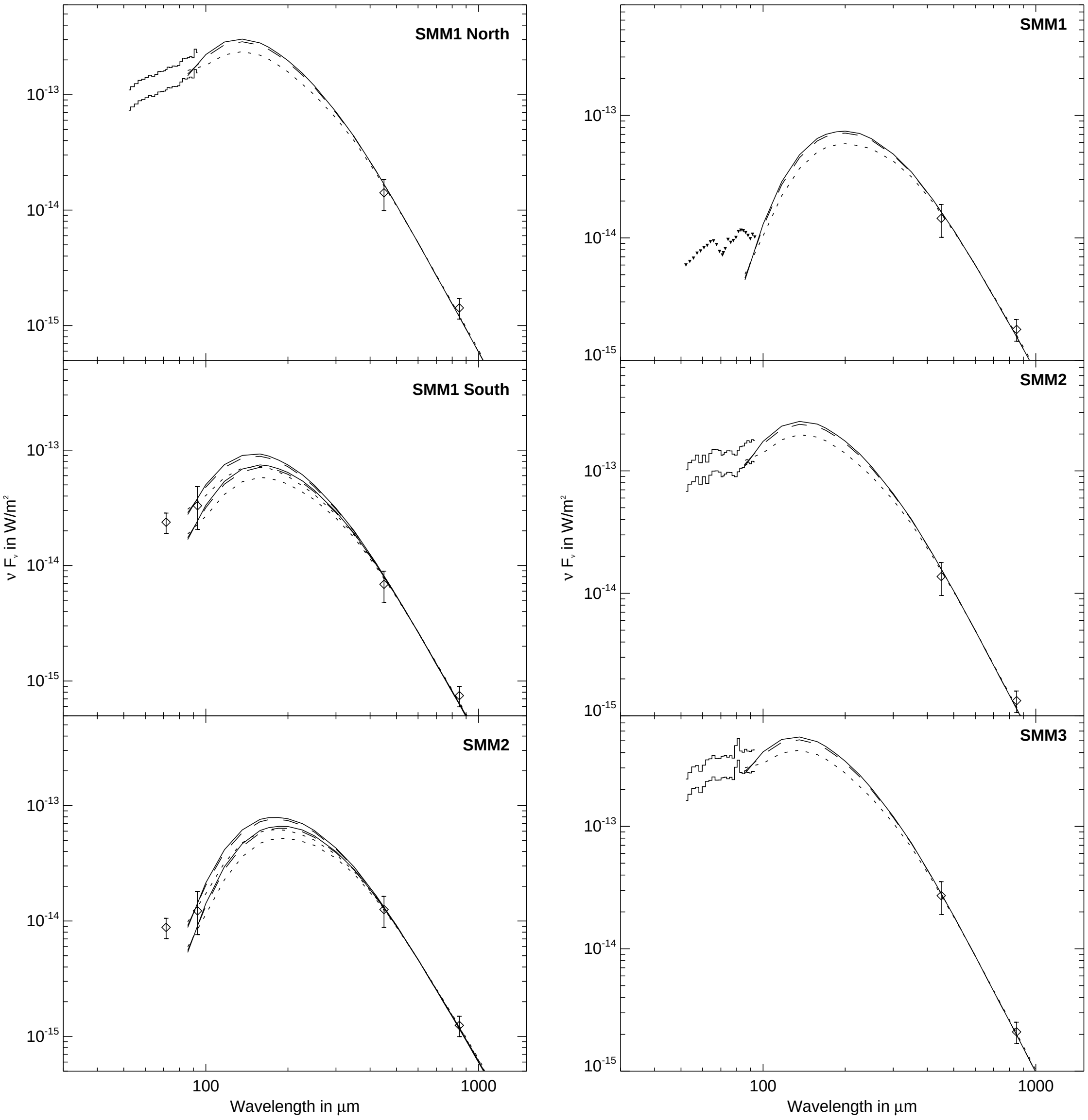

Figure 3.4: Spectral energy distributions of the submillimetre sources in the region ISOSS J19357+1950 (left) and J19486+2556 (right). The diamonds represent photometric data obtained with MIPS (70 $\mu$m) and SCUBA (450 and 850 $\mu$m), and extrapolated data at 93 $\mu$m for ISOSS J19357+2556 SMM1 South and SMM2. Histogram-like bars show the error range of the MIPS SED spectrophotometry (53 to 93 $\mu$m) for ISOSS J19357+2556 SMM1 North, J19486+2556 SMM2 and SMM3, upper limits for SMM1 are plotted with triangles. The lines show modified blackbody fits for $\lambda \geq 93\,\mu$m using different dust opacities (solid: no ice mantles; dotted: thick ice mantles; dashed: thin ice mantles). In the cases with extrapolated 93 $\mu$m data, two sets of curves are shown for spectral slopes of 0.3 and 2.0 between 70 and 93 $\mu$m.

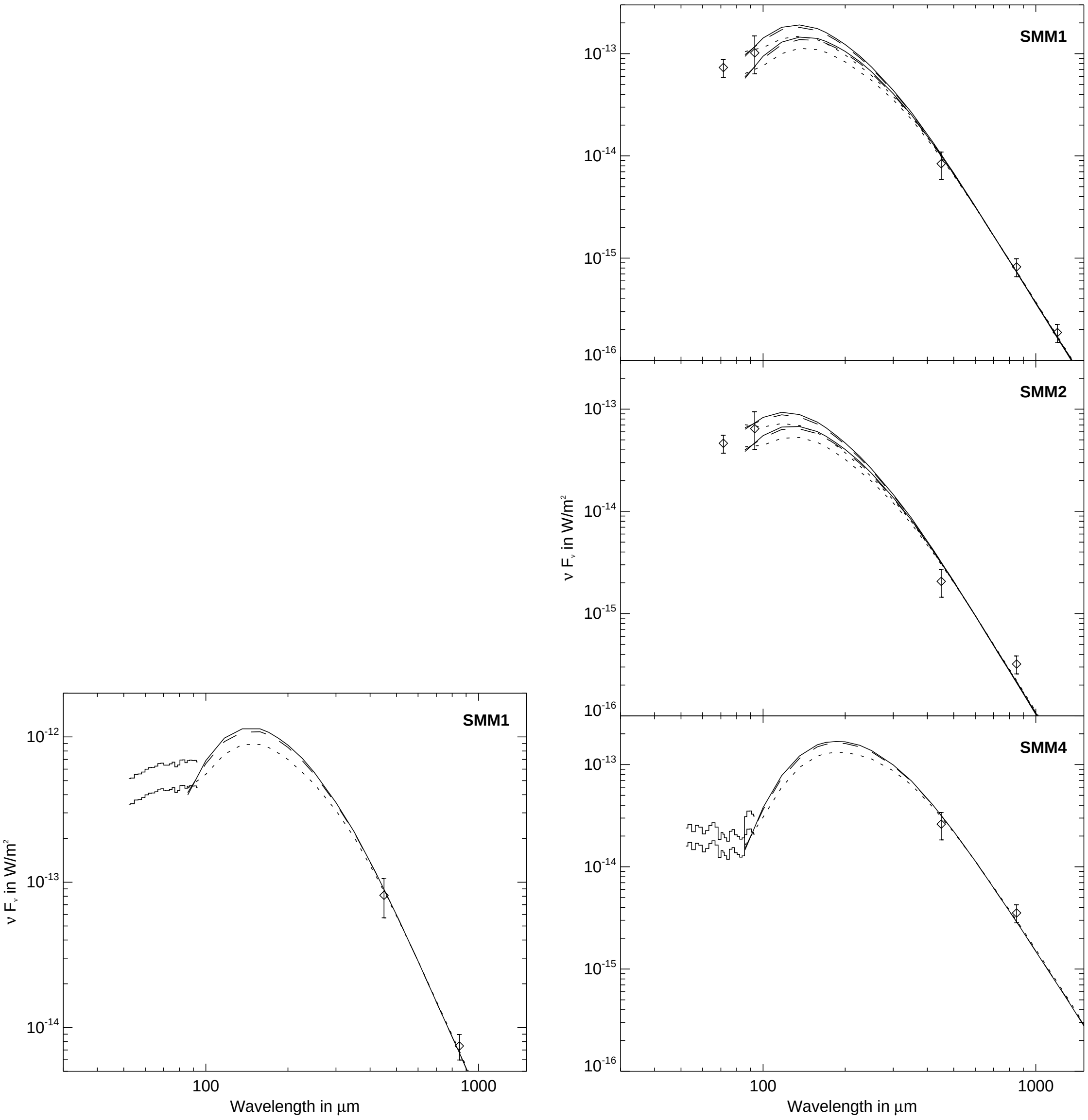

Figure 3.5: Spectral energy distributions of the submillimetre sources in the regions ISOSS J20153+3453 (left) and J20298+3559 (right). The diamonds represent photometric data obtained with MIPS (70 $\mu$m) and SCUBA (450 and 850 $\mu$m), extrapolated data at 93 $\mu$m for ISOSS J20298+3559 SMM1 and SMM2, and the datapoint at 1.2 mm for SMM1. Histogram-like bars show the error range of the MIPS SED spectrophotometry (53 to 93 $\mu$m) for SMM4 and ISOSS J20153+3453 SMM1. The lines show modified blackbody fits for $\lambda \geq 93\,\mu$m using different dust opacities (solid: no ice mantles; dotted: thick ice mantles; dashed: thin ice mantles). For ISOSS J20298+3559 SMM1 and SMM2 two sets of curves are shown for spectral slopes of 0.3 and 2.0 between 70 and 93 $\mu$m.

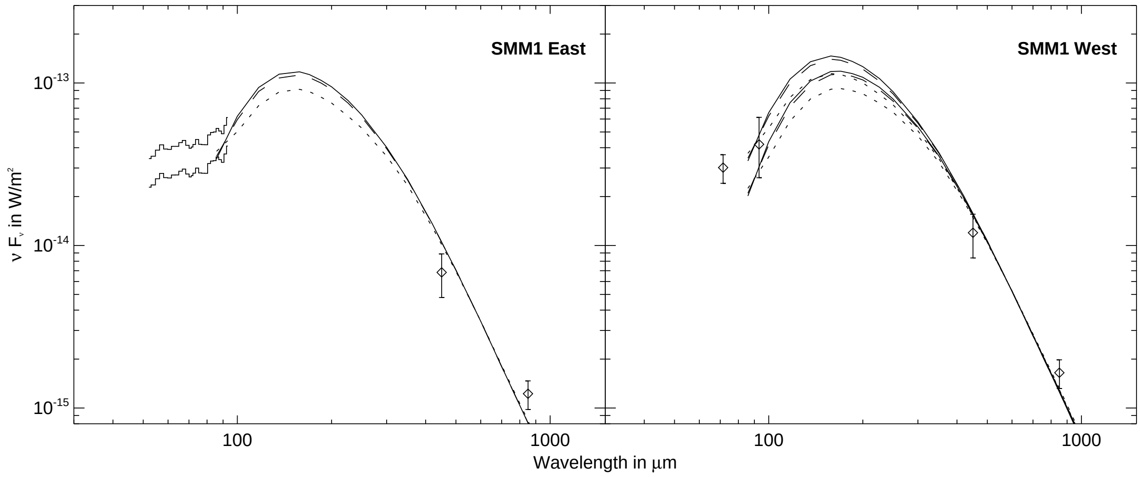

Figure 3.6: Spectral energy distribution of the submillimetre sources in the region ISOSS J22478+6357. The diamonds represent photometric data obtained with MIPS (70 $\mu$m) and SCUBA (450 and 850 $\mu$m) and extrapolated data at 93 $\mu$m for SMM1 West. Histogram-like bars show the error range of the MIPS SED spectrophotometry (53 to 93 $\mu$m) for SMM1 East. The lines show modified blackbody fits for $\lambda \geq 93\,\mu$m using different dust opacities (solid: no ice mantles; dotted: thick ice mantles; dashed: thin ice mantles). For SMM1 West two sets of curves are shown for spectral slopes of 0.3 and 2.0 between 70 and 93 $\mu$m.

## 3.5 Associated infrared sources

A number of sources at 24 $\mu$m and shorter wavelengths were detected that are associated with the submillimetre clumps. To evaluate their nature and relationship with the submillimetre condensations, the sources marked in the mid and right panels of Figures 3.1 to 3.3 were selected. There, singular counterparts can be identified. At distances of $2-4$ kpc, the resolution achieved in the Ks band corresponds to $1600-3200$ AU, and the confusion of sources could only be probed on larger scales than these. For sources that show no near-infrared counterpart, the IRAC resolution at 3.6 $\mu$m, which corresponds to $3000-6000$ AU, limits the search for multiplicity. In addition, checking for optical counterparts was done in Second Digitized Sky Survey DSS2-red maps. Sources without optical counterpart are the best candidates to represent embedded objects, and therefore the association with the molecular and dusty clumps is presumably not a projection effect. However, the actual positions of the sources with respect to the clumps and the foreground extinctions are unknown.

Robitaille *et al.* [2006] presented a grid of YSO model SEDs, which was used to analyse mid-infrared sources detected with *Spitzer* in starforming regions [Indebetouw *et al.*, 2007; Shepherd *et al.*, 2007]. Utilising a Monte-Carlo radiative transfer code, more than 20 000 2D models were computed for ten inclinations each. The different evolutionary phases in the modeled parameter space were ordered according to the Class system [André, 1994] into stages: Stage 0/I (hereafter: Stage I) are very young objects that are deeply embedded in an extended envelope with a cavity surrounding an accretion disk, Stage II contains disk-dominated models, and Stage III represents star-dominated systems. Via a web interface, measured fluxes of individual sources can be put into a model SED-fitting routine to constrain source parameters [Robitaille *et al.*, 2007]. This is applied below in the Discussion

| Region ISOSS... | Clump | Total flux (Jy) 70 $\mu$m | 93 $\mu$m | 450 $\mu$m | 850 $\mu$m | Size (pc) |
|---|---|---|---|---|---|---|
| J19357+1950 | SMM1 N | 3.3 | 6.0 | 2.1 | 0.40 | 0.37 |
| | SMM1 S | 0.57 | 0.80 – 1.3[a] | 1.0 | 0.21 | 0.31 |
| | SMM2 | 0.21 | 0.30 – 0.47[a] | 1.9 | 0.35 | 0.39 |
| J19486+2556 | SMM1 | $< 0.15$ | $< 0.26$ | 2.2 | 0.51 | 0.22 |
| | SMM2 | 2.7 | 4.6 | 2.1 | 0.38 | 0.14 |
| | SMM3 | 7.4 | 11 | 4.1 | 0.59 | 0.21 |
| J20153+3453 | SMM1 | 13 | 17 | 12 | 2.1 | 0.16 |
| J20298+3559 | SMM1 | 1.7 | 2.5 – 3.7[a] | 1.3[c] | 0.23[c] | 0.14[c] |
| | SMM2 | 1.1 | 1.6 – 2.4[a] | 0.31[c] | 0.091[c] | $< 0.07$[c] |
| | SMM4 | 0.41 | 0.81 | 3.9 | 1.0 | 0.34 |
| J22478+6357 | SMM1 E | 0.80 | 1.6 | 1.0 | 0.35 | 0.14 |
| | SMM1 W | 0.72 | 1.0 – 1.6[a] | 1.8 | 0.47 | 0.24 |

| Region ISOSS... | Clump | Dust temperature (K) | Gas mass ($M_\odot$) |
|---|---|---|---|
| J19357+1950 | SMM1 N | 16.6 – 18.7 | 54 – 92 |
| | SMM1 S | 14.1 – 16.5 | 34 – 66 |
| | SMM2 | 12.0 – 13.7 | 85 – 166 |
| J19486+2556 | SMM1 | 11.6 – 12.5[b] | 69 – 123[b] |
| | SMM2 | 16.1 – 18.1 | 28 – 49 |
| | SMM3 | 16.8 – 19.0 | 46 – 79 |
| J20153+3453 | SMM1 | 15.3 – 17.0 | 87 – 149 |
| J20298+3559 | SMM1 | 15.8 – 18.8[d] | 6 – 13[d] |
| | SMM2 | 17.3 – 21.3 | 2 – 3 |
| | SMM4 | 12.1 – 13.2 | 46 – 80 |
| J22478+6357 | SMM1 E | 14.7 – 16.4 | 47 – 81 |
| | SMM1 W | 13.4 – 15.5 | 79 – 153 |

---

[a] Extrapolated values.

[b] Derived using upper limit fluxes.

[c] Flux values and sizes from [Krause *et al.*, 2003].

[d] Derived from listed fluxes and 0.075 Jy at 1.2 mm [Krause *et al.*, 2003].

Table 3.2: Long-wavelength emission and derived properties of the cold component of the detected clumps.

section. As shown in Figure 3.7, the colour-colour diagram [3.6]-[5.8] versus [8]-[24] offers a good distinction between the stages. This combination of colours appears to work best compared to the near-infrared or IRAC colour-colour diagrams.

These colours have also been compiled in Reach *et al.* [2004] for a number of YSOs in the Elephant Trunk Nebula, which have been classified before according to the Class system [see Reach *et al.*, 2004, and references therein]. For a verification of the colour assessment, their data and the regions corresponding to the stages proposed by Robitaille *et al.* [2006] are plotted in the upper left panel of Figure 3.8. The foreground extinction appears to be small for these sources. The Class I/0 and I sources fall into the corresponding Stage I region with one exception. The colours of Class I/II and II sources lie in the Stage II region with one exception. The colours of the debris disk object $\beta$ Pictoris place it on the border between the Stage II and III regions. These accordances support the utility of the colours for classification, so this method was applied to the source samples to get an estimate of their evolutionary status. However, due to the presence of a significant amount of dust in the regions, an enhanced extinction is expected for these sources. In

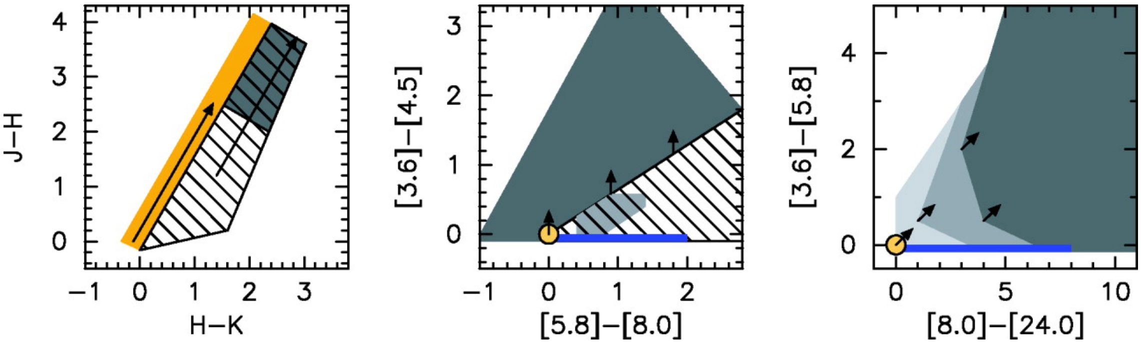

Figure 3.7: Approximate regions of JHK (left), IRAC (centre), and IRAC + MIPS 24 $\mu$m (right) colour-colour space where the different evolutionary stages lie. From dark to light gray: The regions where most models are Stage I, II, and III, respectively. The hashed region in the JHK and IRAC colour-colour plots are regions where models of all evolutionary stages can be present. The dark gray region in the JHK colour-colour plot is also hashed to indicate that this region, although never occupied by Stage II and III models in the absence of extinction, would easily be contaminated by Stage II and III models for high values of extinction. The Stage II area in the IRAC colour-colour plot is hashed to show that although most models in this region are Stage II models, Stage I models can also be found with these colours. The orange region in the JHK colour-colour plot represents the location of reddened stellar photospheres. The yellow disk in the IRAC and IRAC + MIPS 24 m colour-colour plots represents the approximate location of stellar photospheres in the absence of extinction. The blue rectangles show the approximate regions where only disks with large inner holes lie. The reddening vectors show an extinction of $A_V = 20$, assuming the Indebetouw *et al.* [2005] extinction law. Adopted from Robitaille *et al.* [2006].

the remaining five panels of Figure 3.8, the infrared colours of the sources that are marked (and numbered) in Figures 3.1 to 3.3 are plotted. Sources without an optical counterpart in DSS2-red maps are marked with crosses. Most of the evaluated sources exhibit colours lying in the Stage II region or in the vicinity of the Stage I/II transition. Interestingly, a few sources show very red colours that are consistent with Stage I even if a foreground extinction of $A_V \geq 100$ is assumed. Exhibiting [8]-[24] > 5, these sources are distinct from the sample in the upper left panel. Two red sources, Source 1 in ISOSS J19486+2556 and Source 6 in ISOSS J22478+6357, apparently show enhanced 5.8 $\mu$m emission but still lie within the Stage I region. Both are very faint in the near-infrared.

Several sources are associated with “fuzzy” green features in the IRAC composite images and/or extended emission features in the near-infrared: Source 2 in ISOSS J19486+2556, Source 2 in ISOSS J20153+3453, Source 8 in ISOSS J20298+3559 and also towards the SMM3 peak in ISOSS J19486+2556, where the appropriate counterparts to the detected 24 $\mu$m source cannot be identified, and towards the SMM1 peak in ISOSS J20298+3559, where the 24 $\mu$m source shows no counterparts at shorter wavelengths. These features probably trace outflow activity from young accreting objects, and this gives rise to shock-excitation of molecular hydrogen and CO. However, atomic hydrogen Br $\alpha$ line emission can also contribute to the IRAC 4.5 $\mu$m flux.

The most prominent features in the IRAC composite image of ISOSS J19486+2556 are two extended red emission features east of SMM2 and south of SMM3, which are also visible at the MIPS wavelengths. In the near-infrared very red objects are detected that are located towards the centres of the features that themselves are not traced. Extended low-density dust heated to higher temperatures could give rise to the mid- and far-infrared emission.

In the panel of Figure 3.8 corresponding to ISOSS J20298+3559, also the approximate colours of the brightest source in the region, located west of SMM1 are plotted. It was investigated in detail in Krause *et al.* [2003] and classified as a Herbig B2e star that is accreting from a disk that is optically thick. The 8 and 24 $\mu$m images seem to show nonlinear effects due to the brightness of the source which may affect the derived colours corresponding to Stage II.

## 3.6 The clump population

The simple approach toward reproducing the long-wavelength emission of the sample of submillimeter clumps by one component neglects any effects of the density and temperature distributions within the clumps, and the assumption of optically thin emission may be violated in the far-infrared if the (column) density is high enough. Assuming a density profile that is flat in the innermost region of 100 AU radius, follows a power-law ($\rho \propto \mathrm{r}^{-\alpha}$ with $\alpha = 1.5$) in between, and is cutoff exponentially at 20 000 AU, an optical depth of unity is reached at about 100 $\mu$m for a 100 $\mathrm{M}_\odot$ condensation (dust opacities from Draine and Lee [1984]; Steinacker, private communication). Therefore, the total emission at the shortest wavelengths used (93 $\mu$m) may be underestimated and also the mean dust temperatures. Setting the dust temperature to a canonical value of 20 K results in a decrease in the mass by up to a factor of about two for the coldest temperatures, but would require high optical depths at wavelengths around 100 $\mu$m to be consistent with the measured fluxes. However, the required mass scales in the same way as the optical depth. It therefore seems unlikely that this effect causes errors in the mass estimation of more than a factor of two.

The distances to the regions are mainly derived from radial velocities and therefore carry some uncertainty. In Krause *et al.* [2003] the distance to ISOSS J20298+3559 was constrained by an extinction study to 1.8 ± 0.3 kpc. The other distances are estimated to be reliable within $\sim$ 1 kpc, which results in possible mass changes by factors of 1.3 to 1.8. Another uncertainty factor on the order of two for the mass estimate arises from the unknown dust composition; e.g., the dust opacities given by Ossenkopf and Henning [1994] are about five times higher than those used for calculating the model SED grid [Whitney *et al.*, 2003]. It is obvious from the SED diagrams that the dust models used in combination with the one-component approach does not fit the data well for all sources. In the cases of SMM2 in J20298+3559 and SMM1 East in J22478+6357, it seems that dust models corresponding to a lower value of the emissivity index $\beta$ at long wavelengths or the introduction of several emission components would improve the fit. However, the latter approach would increase the number of variable parameters for the fit above the number of datapoints used. From the available measurements in the submillimeter range, no constraints can be placed on the dust properties.

The derived dust temperatures (see Table 3.2) lie between 11.6 and 21.3 K, approximately in the same range as the far-infrared color temperatures from ISO and IRAS fluxes of the whole regions (see Table 3.1). In comparison to other studies, the values are consistent with those of cold dust components derived and assumed for young dense clumps [e.g. Beuther and Steinacker, 2007; Sridharan *et al.*, 2005; Enoch *et al.*, 2007].

The estimated masses that reside in these cold dust and gas components range from 2 $\mathrm{M}_\odot$ up to 166 $\mathrm{M}_\odot$. Taking the mass estimates at face value, four of the clumps may be massive enough ($> 100\,\mathrm{M}_\odot$) to form a high-mass star and an accompanying cluster, if one

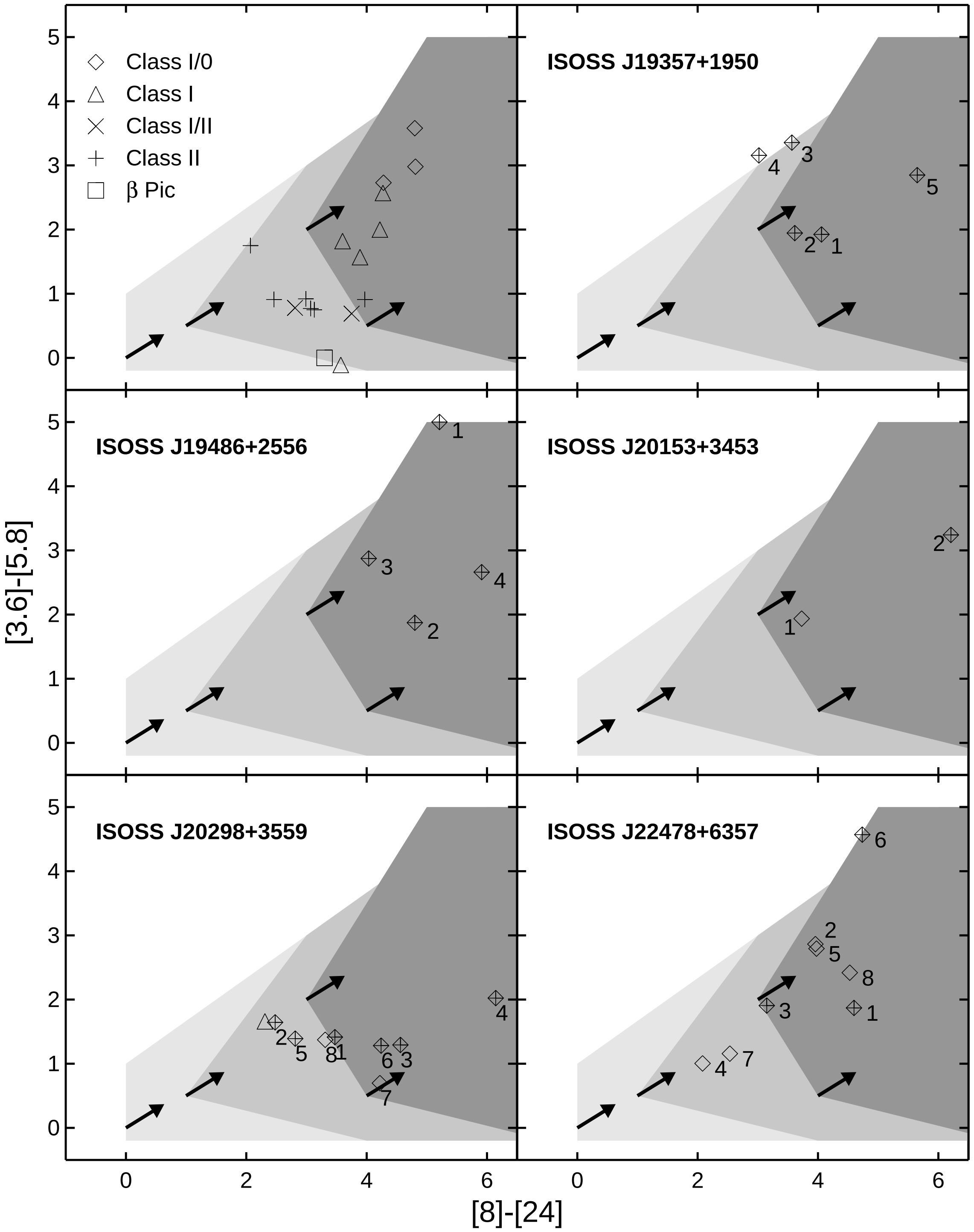

Figure 3.8: IRAC and MIPS infrared colour-colour diagram. The regions where most models are Stage I, II, and III according to Robitaille *et al.* [2006] are shaded from dark to light grey. The vectors show an extinction of $A_V$=20 [Indebetouw *et al.*, 2005]. In the upper left panel, young stellar objects corresponding to different evolutionary stages from Reach *et al.* [2004] are plotted. In the five remaining panels the mid-infrared sources associated with submillimetre emission in the ISOSS starforming regions are drawn (diamonds, numbering as in Figures 3.1 to 3.3). The sources without optical counterpart are marked by crosses. In the panel corresponding to ISOSS J20298+3559, the approximate colours of the Herbig B2e star are represented by the triangle.

assumes that a fraction of 10% of the total mass ends up in massive stars [Zinnecker and Yorke, 2007]. The star formation efficiency is observationally not well-constrained on the scales of individual clumps.

From the source sizes in Table 3.2, volume-averaged densities were derived for the clump sample under the assumption of spherical symmetry. The resulting densities $n_{H_2}$ are between $4 \cdot 10^4$ and $10^6\,cm^{-3}$ with a median value of $2 \cdot 10^5\,cm^{-3}$. Compared to studies of dense condensations found in IRDCs [Rathborne *et al.*, 2006, median density $3 \cdot 10^4\,cm^{-3}$] and in Cygnus X [Motte *et al.*, 2007, median density $2 \cdot 10^5\,cm^{-3}$], the evaluated clumps seem to be more similar to the latter sample based on a millimeter continuum survey. Both the mentioned samples seem to contain candidate objects representing very early stages of massive star formation (e.g. massive infrared-quiet cores). For the sample of Beuther *et al.* [2002b] based on IRAS measurements and containing luminous infrared sources, a lower mean density of $9 \cdot 10^3\,cm^{-3}$ is recalculated in Motte *et al.* [2007]. The direct comparison of these densities may be affected by systematically different derivation methods, but it suggests that the source selection based on longer wavelengths gives access to presumably less evolved sources. In the present case, the $170\,\mu$m band measurements constrain the average dust temperature to lower values than those that can be inferred from the IRAS bands.

## 3.7 The nature of the $24\,\mu$m sources

The majority of the clumps appear in a stage where $24\,\mu$m sources are present. In the following, their ability to generate high-mass star progenitors is discussed, and then selected subsamples are evaluated in more detail. During their formation high-mass stars develop high luminosities. According to the approach of McKee and Tan [2003], the stage where the luminosity exceeds $100\,L_\odot$ is already reached when one solar mass has been accreted. The corresponding timescale is around several $10^4$ years. Therefore young high-mass stars should stand out as luminous sources. However, due to the reprocessing of the short-wavelength radiation by the surrounding dusty envelopes (absorption and thermal reemission), only a fraction of the luminosity is released at the near- and mid-infrared wavelengths we probed (here we consider $\lambda \leq 24\,\mu$m). If the source is deeply embedded, its infrared colours are expected to be very red and the emission at optical wavelengths to be undetectable. By combining the classification from the colours with an estimate of the total luminosity, including the far-infrared and submillimetre data, the probability of a source being a high-mass star precursor can be assessed. Sources of Stage II or later should generate high luminosities to be considered candidate massive YSOs.

The sources' locations in the infrared colour-colour space are considered as qualitatively describing their evolutionary stages. From the sample of $24\,\mu$m sources that has been evaluated in the Analysis section the majority is estimated to be comparable to Stage II models. As the majority of the associated clumps do not substantially exceed a total luminosity of $200\,L_\odot$, most of these objects rather represent low-mass YSOs. Their association with the submillimetre clumps suggests that they have formed inside and that the clumps contain density substructures.

### 3.7.1 Very red protostar candidates

As described above, sources that display very red infrared colours and sources that are not detected in the shorter-wavelength bands are the best candidates to represent very young objects that may evolve to massive YSOs. Using Figure 3.8, Source 5 in ISOSS

J19357+1950, Source 1 in ISOSS J19486+2556, and Source 2 in ISOSS J20153+3453 was selected. The remaining sources with [8]-[24] $> 5$ are not associated with massive submillimetre clumps and probably will not be able to accrete enough material to end up as high-mass stars. Furthermore, the submillimetre source SMM1 in ISOSS J20298+3559 was found in Krause *et al.* [2003] to be a candidate Class 0 object. A 24 $\mu$m source was detected towards this peak, which is not seen at shorter wavelengths. Associated outflow-tracing emission supports its classification as young protostellar object.

Source 5 in ISOSS J19357+1950 is located towards the massive clump SMM2. The online model fitter was applied using the fluxes including upper limits in the H band, at 70, 450, and 850 $\mu$m. Source 2 found towards the massive clump ISOSS J20153+3453 SMM1 exhibits very red colours and is associated with a possible outflow. The online model fitter was fed with the fluxes including upper limits in the J band, at 70, 450, and 850 $\mu$m. For SMM1 in ISOSS J20298+3559, the fluxes measured at 24, 70, 450, and 850 $\mu$m and upper limits in the IRAC bands and in the Ks band were put in. The range of possible foreground extinction was selected to $\mathrm{A_V} \leq 500$. The fitting results for these three sources are listed in Table 3.3. From the inspection of the SED plots, a cut-off value of $\chi^2_{\mathrm{d}}$ ($\chi^2$ per datapoint) was established to select the models that fit the datapoints within reasonable margins. Furthermore, the total extinction to the central source by combining the fitted foreground extinction with the extinction along the line of sight from the model outer radii inwards is given. These parameters are degenerate to some extent and allow models with different envelope sizes to be fitted via compensating foreground extinctions. The results are consistent with the interpretation of the sources as young embedded stellar precursors. The observed outflow activity signatures accord with high accretion rates for the last two sources. In the cases of ISOSS J19357+1950 SMM2 and ISOSS J20153+3453 SMM1, the estimated high total masses of around 100 $\mathrm{M_\odot}$ residing in cold components of dust and gas should allow ongoing accretion and the build-up of high-mass stars. However, due to the multiplicity of near-infrared sources that are detected in the vicinity of ISOSS 20153+3453 SMM1, the further evolution of this object is not straightforward. Towards ISOSS J19357+1950 SMM2, there also is a second, more evolved source nearby. In the third case, the mass estimate of about 10 $\mathrm{M_\odot}$ for ISOSS J20298+3559 SMM1 is consistent with the source being an intermediate-mass star precursor.

The remaining very red, candidate Stage I source located towards the clump SMM1 in the region ISOSS J19486+2556 is particularly interesting because of the low infrared luminosity in comparison to the submillimetre, making it a candidate for a young and deeply embedded object. The photometric data were put into the online model fitter including upper limits in the Ks band, at 70, 450, and 850 $\mu$m. A cut-off at $\chi^2_{\mathrm{d}} < 49.6$ was chosen to select the acceptable fits. The results for this source are ambiguous. Among the selected models are several belonging to the Stage I category with central source masses of about 0.1 $\mathrm{M_\odot}$ but also a majority of Stage II models with central source masses between 3 and 4.5 $\mathrm{M_\odot}$, both with and without envelopes. There is no significant difference in the fitted total extinction towards the central sources. Therefore, the parameters of this source could not be assessed and constrained.

### 3.7.2 Evolved young stellar objects

Besides, also sources whose SEDs are dominated by emission at mid-infrared wavelengths have been detected. They exhibit higher total luminosities and may represent more massive YSOs. By comparing the spectral energies at 24 $\mu$m and 70 $\mu$m, two candidate sources were found, located towards SMM4 in ISOSS J20298+3559 (Source 8) and SMM1 East in ISOSS J22478+6357 (Source 3). In addition, the fluxes from Krause *et al.* [2003, IRS 6] for

| Region ISOSS... | J19357+1950 | J20153+3453 | J20298+3559 |
|---|---|---|---|
| Source | 5 | 2 | - |
| Associated clump | SMM2 | SMM1 | SMM1 |
| Selected cut-off | $\chi^2_\mathrm{d} < 14.2$ | $\chi^2_\mathrm{d} < 9.3$ | $\chi^2_\mathrm{d} < 12.5$ |
| Fitted models | Stage I | Stage I | Stage I |
| Total extinction | $\mathrm{A_V} \sim 85$ | $\mathrm{A_V} \sim 100$ | $\mathrm{A_V} > 200$ |
| Central mass ($\mathrm{M_\odot}$) | 0.2 – 2.1 | 0.7 – 2.3 | 0.2 – 4.6 |
| Envelope accretion rate ($\mathrm{M_\odot}$/yr) | $1.6 \cdot 10^{-6} - 8.9 \cdot 10^{-5}$ | $1.5 \cdot 10^{-6} - 3.4 \cdot 10^{-4}$ | $4 \cdot 10^{-6} - 7 \cdot 10^{-4}$ |

Table 3.3: Results of the SED fitting for three very red young stellar objects.

the I, J, H, and Ks bands as well as upper limits at 70, 450, and 850 $\mu$m were used for the former, and upper limits in the J band, at 70, 450 and 850 $\mu$m for the latter source. The fitting results are compiled in Table 3.4. The first source is considered to be an embedded proto- or pre-main-sequence star of intermediate mass as also suggested by Krause *et al.* [2003]. It was probably formed in the SMM4 clump. The results for the second source are consistent with the source representing an evolved YSO of at least intermediate mass that is still embedded and presumably has been formed within the clump SMM1 East.

| Region ISOSS... | J20298+3559 | J22478+6357 |
|---|---|---|
| Source | 8 | 3 |
| Associated clump | SMM4 | SMM1 East |
| Selected cut-off | $\chi^2_\mathrm{d} < 3.3$ | $\chi^2_\mathrm{d} < 2.1$ |
| Fitted models | Stage II[a] | Stage II[b] |
| Total extinction | $6 < \mathrm{A_V} < 9.4$ | $29 < \mathrm{A_V} < 41$ |
| Total luminosity ($\mathrm{L_\odot}$) | $\sim 150$ | $\sim 2000$ |
| Central mass ($\mathrm{M_\odot}$) | 3.2 – 4.9 | 6 – 8.5 |
| Preferred inclination | low | - |
| Disk mass ($\mathrm{M_\odot}$) | $4 \cdot 10^{-6} - 10^{-1}$ | $10^{-5} - 10^{-1}$ |
| Accretion rate ($\mathrm{M_\odot}$/yr) | $10^{-11} - 10^{-6}$ | $5 \cdot 10^{-11} - 2 \cdot 10^{-5}$ |
| System age (yr) | $10^6 - 10^7$ | $10^6 - 6 \cdot 10^6$ |

[a] $\mathrm{M_{disk}/M_* \geq 7.7 \cdot 10^{-7}}$
[b] $\mathrm{M_{disk}/M_* \geq 9.5 \cdot 10^{-7}}$

Table 3.4: Results of the SED fitting for two evolved young stellar objects.

## 3.8 Conclusions

In this chapter, the analysis of multi-wavelength observations towards five star-forming regions that were identified using the ISOPHOT Serendipity Survey at 170 $\mu$m are presented. The results can be summarised as follows:

1. One to four compact ($\sim$ 0.2 pc) submillimetre condensations were found in every region. They represent molecular clumps containing a cold component of gas and dust. The dust temperature estimates vary between 11.6 and 21.3 K and accord with the large-scale colour temperatures measured in the far-infrared.

2. The resulting estimated clump masses that reside in these cold components range from 2 to 166 $\mathrm{M}_\odot$. Four out of twelve clumps may be massive enough ($> 100\,\mathrm{M}_\odot$) to be promising as birthplaces for high-mass stars.

3. Multiple associated mid-infrared sources were identified for the majority of the clumps, suggesting that they embody significant density substructures on smaller scales than probed by the submillimetre observations ($\gtrapprox 0.1\,\mathrm{pc}$). Since the emission of most clumps is dominated by the cold material, thriving star formation from further collapse of overdensities is expected.

4. Most of the associated sources are considered as low-mass YSOs in an evolutionary state later than Class 0/I partly embedded in the clumps where they have formed.

5. In the region ISOSS J19357+1950, a massive clump of around 100 $\mathrm{M}_\odot$ is present. A probably deeply embedded accreting Class 0/I protostar of $\sim 1\,\mathrm{M}_\odot$ was detected adjacent to a more evolved YSO. Similarly, one massive clump of about 100 $\mathrm{M}_\odot$ is present in ISOSS J20153+3453 and a cluster of sources was detected in the vicinity that contains a presumably deeply embedded accreting protostar with a current mass of $\sim 1.5\,\mathrm{M}_\odot$. Its evolutionary state corresponds to Class 0/I, and there is evidence of outflow activity from this object.

6. The source SMM1 in ISOSS J20298+3559 likely represents a young accreting intermediate-mass star precursor embedded in a molecular clump of $\sim 10\,\mathrm{M}_\odot$. Towards SMM4 in the same region, an embedded proto- or pre-main-sequence star of $3.2 - 4.9\,\mathrm{M}_\odot$ was identified that probably evolved from the associated clump of $\sim 60\,\mathrm{M}_\odot$.

7. In the region ISOSS J22478+6357, a candidate protostar of $6 - 8.5\,\mathrm{M}_\odot$ was found that is embedded in the associated SMM1 East clump ($\sim 60\,\mathrm{M}_\odot$).

8. No stellar precursors that could have current masses of 10 $\mathrm{M}_\odot$ or more were identified. Therefore, whether such objects will emerge within the identified clumps remains unsettled. However, the presence of intermediate-mass proto- or pre-main-sequence star candidates and the large clump masses indicate that one can expect that high-mass stars are also formed in these systems.

9. The presented study reveals that the search for regions containing large fractions of cold material in the far-infrared has successfully identified starforming regions associated with cold and massive clumps. Compared to sources selected at shorter wavelengths, they may represent less evolved stages of high-mass star formation. Furthermore, this study demonstrates that the detailed star-forming content can only be accessed with a multi-wavelength approach including sensitive mid- and far-infrared observations and sufficient angular resolution.

# Chapter 4

# Star-forming cores embedded in the massive cold clump ISOSS J18364-0221 SMM1: Fragmentation, collapse, and energetic outflows

## 4.1 Motivation and outline

### 4.1.1 Star formation in massive cold clumps

To explore the origin of high-mass stars, stellar associations and clusters, the onset of star formation in massive cold clumps has to be investigated in detail. Interferometric observations provide the essential spatial resolution to study the substructure of clumps. To infer the properties of embedded cores further requires a good coverage of their spectral energy distribution. This chapter presents such a detailed study of a preselcted clump located in the region ISOSS J18364-0221. In particular, the amount of fragments in the clump and their properties, the arising outflow activity, and the indications for collapse were investigated. These properties are crucial to evaluate the fate of the clump and compare it to the results of recent theoretical prospects.

### 4.1.2 The ISOSS J18364-0221 star-forming region and the SMM1 clump

The star-forming region ISOSS J18364-0221 (R.A. $18^h36^m24.7^s$, Decl. -02°21′49″[J2000]) was initially studied by Birkmann *et al.* [2006]. It is located at a distance of about 2.2 kpc. Derived from the near-infrared extinction over a $15' \times 15'$ field ($\sim 100\,\mathrm{pc}^2$), the cloud complex associated with the star-forming region comprises a mass $\mathrm{M} \approx 3200\,\mathrm{M}_\odot$. In the same manner, a lower mass limit $\mathrm{M} \geq 460\,\mathrm{M}_\odot$ was found for the central region ($\sim 1\,\mathrm{pc}^2$), while the far-infrared and submillimetre measurements give a luminosity $\mathrm{L} \approx 800\,\mathrm{L}_\odot$, an average dust temperature of about 15 K and a mass of $900^{+450}_{-330}\,\mathrm{M}_\odot$. This region contains two clumps detected in the submillimetre continuum named SMM1 and SMM2 that are separated by about $1.5'$ along the east-west direction. The effective radius of the SMM1 clump is about 0.2 pc, and from the thermal emission a characteristic dust temperature of $16.5^{+6}_{-3}\,\mathrm{K}$ and a clump mass of $\mathrm{M}_{\mathrm{SMM1}} = 75 \pm 30\,\mathrm{M}_\odot$ were found. Molecular line observations show that the clump is collapsing and that at least one outflow is present.

The outflow properties resulting from the single-dish observations, i.e. the outflow mass of about $18\,\mathrm{M}_\odot$ and the mass outflow rate of $10^{-3}\,\mathrm{M}_\odot\,\mathrm{yr}^{-1}$, are comparable to values derived for outflows from presumed high-mass star precursors. These results render the SMM1 clump a promising object to study the early phases of collapse and fragmentation occurring in massive cold cores.

The detailed study of this source presented here made use of recently collected infrared and (sub-)millimetre data described in the next section. They reveal two star-forming cores and molecular outflows (Section 4.3). In Section 4.4, the core properties are discussed in the context of early-stage star formation and a comparison of the observed HCN spectra with simple radiative transfer models is presented. Finally, the results are summarised in Section 4.5.

## 4.2 Observations and data reduction

### 4.2.1 Near-infrared observations

Imaging observations in the J, H, and Ks band towards ISOSS J18364-0221 have been obtained and are described in Birkmann *et al.* [2006]. Additional near-infrared images in the $H_2$ $\nu = 1\text{-}0$ S(1) line ($\lambda = 2.122\,\mu\mathrm{m}$) were taken with the Calar Alto 3.5 m telescope in October 2005 using the prime-focus wide-field camera Omega-2000 [Baumeister *et al.*, 2003]. Omega-2000 features a field of view (FOV) of $15.4 \times 15.4\,\mathrm{arcmin}^2$ with a pixel scale of $0.4496''\,\mathrm{pix}^{-1}$. The exposures were dithered on source to allow for sky subtraction. The data reduction was done using IRAF.

### 4.2.2 Mid- and far-infrared observations

IRAC [Fazio *et al.*, 2004] imaging in all four photometric bands, MIPS [Rieke *et al.*, 2004] imaging at $24\,\mu\mathrm{m}$ and $70\,\mu\mathrm{m}$ and MIPS spectral energy distribution (SED) mode observations were undertaken with *Spitzer* [Werner *et al.*, 2004]. The basic flux calibrated imaging data of the *Spitzer Science Center* (SSC) pipeline were used for further data reduction and analysis. Cosmetic corrections and astrometric refinement were performed with the MOPEX software [Makovoz and Marleau, 2005], and the final images were combined using scripts in IRAF. Aperture photometry and PSF fitting (FWHM about $1''$, $1.3''$, $1.6''$, $2''$, $6''$, and $17''$) was done with the aperture corrections given in the IRAC data handbook and on the SSC website[1]. The MIPS SED mode calibration is based on a spectrum of $\alpha$ Boo [Low *et al.*, 2005] and the measured MIPS $70\,\mu\mathrm{m}$ fluxes. The calibration uncertainties are about 2% (IRAC, Reach *et al.* [2005]), 4% (MIPS 24, Engelbracht *et al.* [2007]), and 10% (MIPS 70, Gordon *et al.* [2007]). The resulting photometric accuracy is estimated to 5% (IRAC), 10% (MIPS 24), and 20% (MIPS 70 and SED).

### 4.2.3 Submillimetre observations

The submillimetre continuum observations with SCUBA at the JCMT are outlined in Birkmann *et al.* [2006]. In light of the results from the interferometric observations that are described in the next section, the jiggle maps were reanalysed. The ORAC-DR [Jenness and Economou, 1999] and SURF [Jenness and Lightfoot, 1998] software were used for data reduction and the photometric calibration based on maps of Uranus acquired shortly before and after the observations. Further analysis as described in Sandell and Weintraub [2001] used the MIRIAD software [Sault *et al.*, 1995]. The deviations of the JCMT beam from a

---

[1] `http://ssc.spitzer.caltech.edu/mips/apercorr/`

single Gaussian have been considered by using the Uranus maps to construct symmetric beam models and deconvolve the maps of the target regions. The derived beam sizes are $8.2''$ at $450\,\mu$m and $14.8''$ at $850\,\mu$m. The maps were restored with Gaussian beams of $8''$ and $14''$, respectively, and fluxes as well as deconvolved source sizes have been derived by fitting Gaussian components. The noise levels ($1\sigma$) in the restored maps are $100\,\mathrm{mJy\,beam^{-1}}$ at $450\,\mu$m and $23\,\mathrm{mJy\,beam^{-1}}$ at $850\,\mu$m. The photometric accuracy obtained is estimated to 30% at $450\,\mu$m and 20% at $850\,\mu$m. For a large aperture covering the SMM1 clump, the photometric results reproduce those of Birkmann *et al.* [2006] within the uncertainty ranges.

### 4.2.4 Millimetre observations

Millimetre observations using the IRAM 30m and Plateau de Bure Interferometer (PdBI) have been carried out. The molecular lines CO(2-1), $\mathrm{HCO^+}$(1-0) and HCN(1-0) have been observed together with the continuum at 1.3 mm and 3.4 mm. CO line emission commonly traces outflowing molecular gas of low density while the $\mathrm{HCO^+}$ and HCN lines probe dense regions. The latter usually trace internal motions, with the HCN emission originating from deeper embedded parts. The line frequencies are 230.538 GHz for CO(2-1) and 89.188526 GHz for $\mathrm{HCO^+}$(1-0). The HCN(1-0) transition includes three hyperfine components within 4 MHz at 88.630416 GHz ($\mathrm{F_{1\rightarrow1}}$), 88.631847 GHz ($\mathrm{F_{2\rightarrow1}}$), and 88.633936 GHz ($\mathrm{F_{0\rightarrow1}}$)[2]. The PdBI configurations C and D were utilised; D was observed in September 2006 and C in April 2007 with the new generation facility receivers. Spectral resolutions of 40 kHz (3 mm lines), 160 kHz (CO(2-1)), 1.25 MHz (3.4 mm continuum, $3 \times 160$ MHz bandwidth), and 2.5 MHz (1.3 mm continuum, $2 \times 320$ MHz bandwidth) were used. Phase calibrators were 1749-096 and 1741-038, additional amplitude calibrators were MWC349 and 3C273. Corresponding short-spacing observations were accomplished in February 2007 at the IRAM 30m as On-the-fly maps using the single pixel heterodyne receivers with the VESPA correlator and spectral resolutions of 80 kHz (1 mm lines, 80 MHz bandwidth) and 20 kHz (3 mm lines, 40 MHz bandwidth). The data were reduced and calibrated with the GILDAS[3] software. GILDAS was also used to combine the short-spacing and interferometric data for the lines. In the case of CO, the conversion of the measured visibilities to maps used a weighting scheme that achieves the highest spatial resolution (synthesised beam size of $1.85'' \times 1.33''$) at the expense of sensitivity for extended emission. Therefore the combined CO map does not recover the complete flux. Compared to the single-dish spectra, the line wing fluxes in the combined map are lower by a factor of $5 \pm 1$. For HCN, the comparison of the extracted spectra shows that the flux measured in the single-dish data is reproduced in the combined map. The synthesised continuum beam sizes are $1.9'' \times 1.0''$ (PA 11.6°) at 1.3 mm and $4.6'' \times 3.2''$ (PA 6.1°) at 3.4 mm. The reached noise levels ($1\sigma$) in the cleaned maps are $0.6\,\mathrm{mJy\,beam^{-1}}$ (1.3 mm continuum), $0.13\,\mathrm{mJy\,beam^{-1}}$ (3.4 mm continuum), $0.5\,\mathrm{Jy\,beam^{-1}\,km\,s^{-1}}$ (CO(2-1)), $0.07\,\mathrm{Jy\,beam^{-1}\,km\,s^{-1}}$ ($\mathrm{HCO^+}$(1-0)), and $0.1\,\mathrm{Jy\,beam^{-1}\,km\,s^{-1}}$ (HCN(1-0)). Assuming a dust temperature of 15 K, the sensitivity corresponds to total masses of about $0.3\,\mathrm{M_\odot}$ ($3\sigma$ in the 1.3 mm continuum). The noise level ($1\sigma$) in the individual HCN(1-0) spectra used for the modelling is 0.1 K. The 1.2 mm continuum was observed with the MAMBO-2 bolometer array in March 2007. The MOPSIC software was used for data reduction and the noise level ($1\sigma$) in the resulting map is $10\,\mathrm{mJy\,beam^{-1}}$. The photometric accuracy is estimated to 20%.

---

[2] NIST Recommended Rest Frequencies for Observed Interstellar Molecular Microwave Transitions: `http://physics.nist.gov/restfreq`

[3] `http://www.iram.fr/IRAMFR/GILDAS`

## 4.3 Results

### 4.3.1 Multiwavelength maps of SMM1

In Figs. 4.1 and 4.2 multiwavelength maps observed towards ISOSS J18364-0221 SMM1 are shown. In the interferometric millimetre continuum observations SMM1 is resolved into two cores SMM1 North and SMM1 South (Fig. 4.1 lower panels), separated by 9.5″ (ca. 21000 AU). In the near-infrared (Fig. 4.1 upper left), noticeable extinction and reddening is present in the surrounding of SMM1. There are no near-infrared sources detected towards the (sub-)millimetre peaks. The mid-infrared measured with IRAC (Fig. 4.1 upper right) is dominated by extended emission in the 8 $\mu$m band along the outer rim of SMM1. Towards the centre of SMM1, a filamentary structure is observed in absorption, and no stellar objects are associated. At 24 $\mu$m (Fig. 4.1 lower left) a point source at SMM1 South shows up. At this wavelength, the extended emission around SMM1 is also visible, and in the north-west a dip remains, but the absorption feature is superposed by the PSF of the southern source. No obvious 24 $\mu$m source towards SMM1 North is detected. Similarly, SMM1 South emits at 70 $\mu$m (Fig. 4.1 lower right). The wide PSF overlays possible extended emission at the rim of SMM1, and no obvious emission at SMM1 North is detected.

In the interferometric 1.3 mm continuum map (Fig. 4.2 top row), both SMM1 North and South appear slightly extended to the north, but the beam sidelobes may affect the morphology. At 3.4 mm they appear unresolved (Fig. 4.2 bottom row), and none of the extensions are traced. The contours in Fig. 4.2 derived from the emission in the line wings of the CO(2-1) and $HCO^+$(1-0) transitions reveal two molecular outflows. SMM1 South constitutes the origin of a north-east-to-south-west (PA ca. 50°) outflow that also gives rise to the mid-infrared features. Towards SMM1 North an outflow in east-to-west direction (PA ca. -80°) is found. Its red lobe blends into the red lobe of the SMM1 South outflow. Most prominent in CO(2-1) is the SMM1 South blue outflow lobe that appears collimated. In $HCO^+$(1-0), the blue lobe of the SMM1 North outflow is strongest and it also shows a rather low outflow opening angle, but in both cases the outflows are traced only close to the cores and no accurate quantitative measure could be derived.

Fig. 4.3 shows the near-infrared $H_2$ $\nu = 1\text{-}0$ S(1) ($\lambda = 2.122\,\mu$m) line emission map. This map has been derived by subtracting the scaled K band image from the narrow-band image so that stars cancelled out. Stars that were not properly subtracted have been masked afterwards for clarity. As shown in the inlay of Fig. 4.3, towards the blue and red lobes of the molecular outflow driven by SMM1 South there is patchy near-infrared $H_2$ emission. Such features trace protostellar jets, and the emission probably arises from collisionally excited $H_2$ in shocked gas [Elias, 1980; Reipurth and Bally, 2001, and ref. therein]. This is supported by faint filamentary emission in the 4.5 and 5.8 $\mu$m bands detected lateral to SMM1 South along north-east-to-south-west and in the vicinity of SMM1 North (yellowish features in Fig. 4.1 top right). These bands contain several $H_2$ lines [Noriega-Crespo *et al.*, 2004; Smith and Rosen, 2005]. Only a weak near-infrared feature is detected close to the blue lobe of the SMM1 North outflow. On the large-scale map, additional filaments of $H_2$ emission are visible. Though they are not exactly aligned with the molecular outflows, they can be assigned to individual lobes which would make it necessary that the proposed jets show bending resulting in S-shapes. The outermost features in the North-East and South-West are located at a projected distance of about 6.7 pc from each other, and the South-West feature is at a projected distance of about 4.6 pc from SMM1 South. Among the sources detected in the vicinity of the features, no other candidates for jet-driving young stellar objects are obvious.

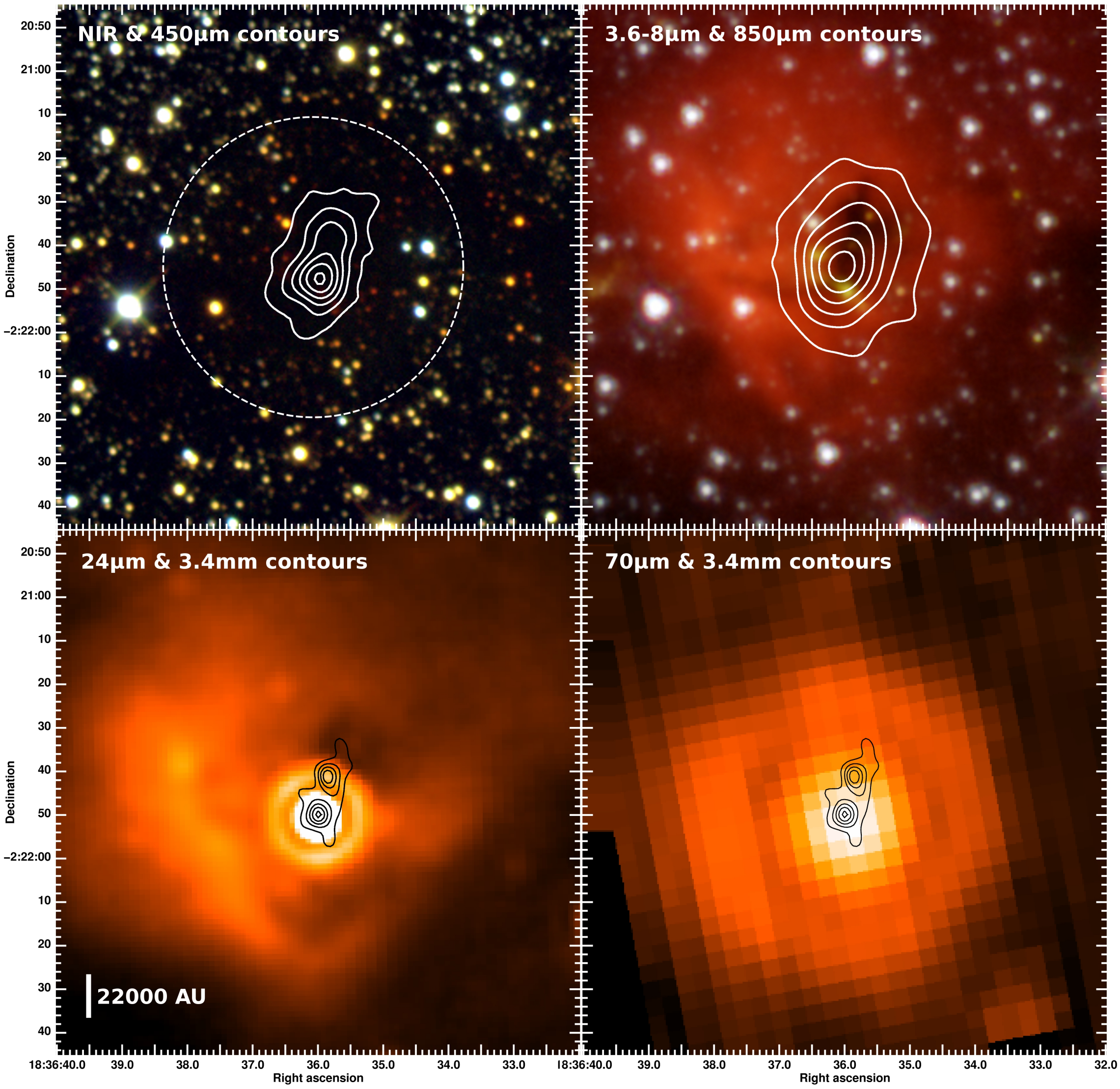

Figure 4.1: Multiwavelength $2' \times 2'$ maps towards ISOSS J18364-0221 SMM1. Upper left: Near-infrared colour composite of J, H, and Ks band observations with Omega-2000 and solid contours of the SCUBA 450 $\mu$m map ($5\sigma$, $10\sigma, \ldots$). The dashed contour shows the region used for background subtraction in the 450 and 850 $\mu$m maps. Upper right: Mid-infrared colour composite of the 4 *Spitzer* IRAC channels and contours of the SCUBA 850 $\mu$m map ($5\sigma$, $10\sigma, \ldots$). Lower left: *Spitzer* MIPS 24 $\mu$m map and contours of the PdBI 3.4 mm continuum observations ($3\sigma$, $6\sigma, \ldots$). Lower right: *Spitzer* MIPS 70 $\mu$m map and contours of the PdBI 3.4 mm continuum observations ($3\sigma$, $6\sigma, \ldots$). The 3.4 mm contours in the lower panels reveal the two cores SMM1 North and South.

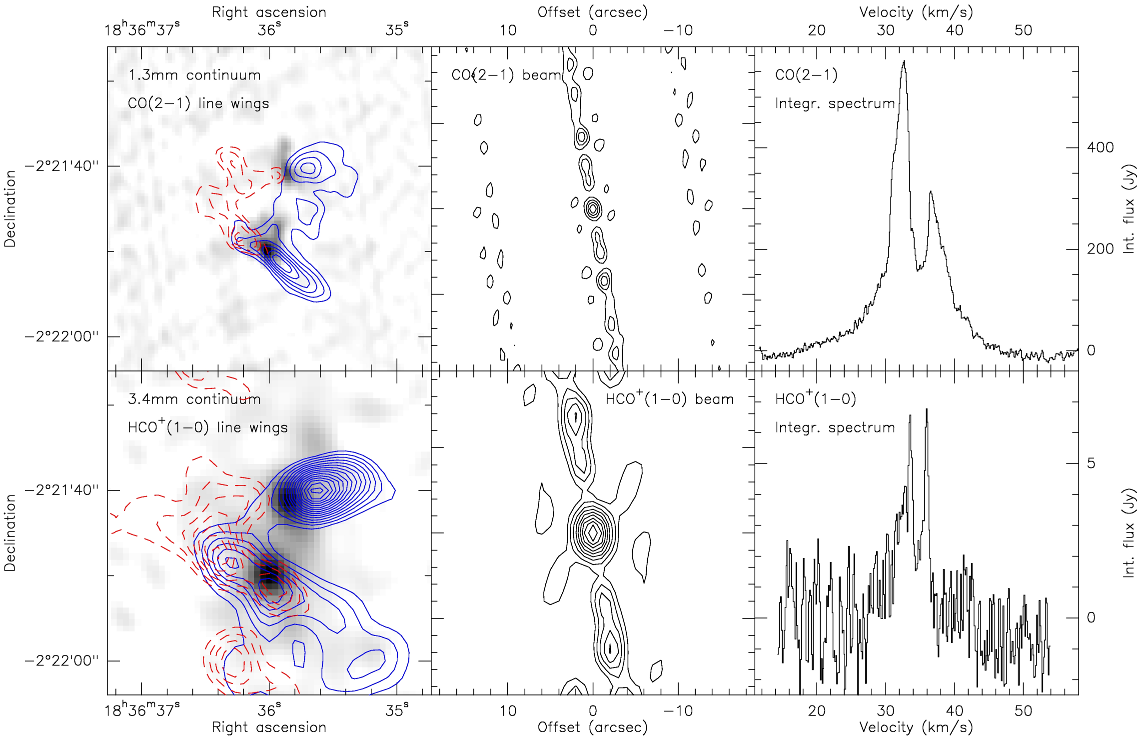

Figure 4.2: ISOSS J18364-0221 SMM1 CO(2-1) and HCO$^+$(1-0) observations. Top row: Observations at 1.3 mm; continuum emission is shown in grey-scale, and CO(2-1) line emission in dashed red (velocity range 20. . . 30 km s$^{-1}$; contours at 2, 3, . . . , 7 Jy beam$^{-1}$ km s$^{-1}$) and solid blue (40. . . 50 km s$^{-1}$; contours at 3, 4, . . . , 9 Jy beam$^{-1}$ km s$^{-1}$). Besides, the beam pattern in steps of 20% and the integrated CO(2-1) spectrum are plotted. Bottom row: Observations at 3.4 mm; continuum emission is shown in grey-scale, and HCO$^+$(1-0) line emission in dashed red (velocity range 20. . . 30 km s$^{-1}$; contours at 60, 80, . . . , 200 mJy beam$^{-1}$ km s$^{-1}$) and solid blue (40. . . 50 km s$^{-1}$; contours at 100, 120, . . . , 400 mJy beam$^{-1}$ km s$^{-1}$). Besides, the beam pattern in steps of 10% and the integrated HCO$^+$(1-0) spectrum are plotted.

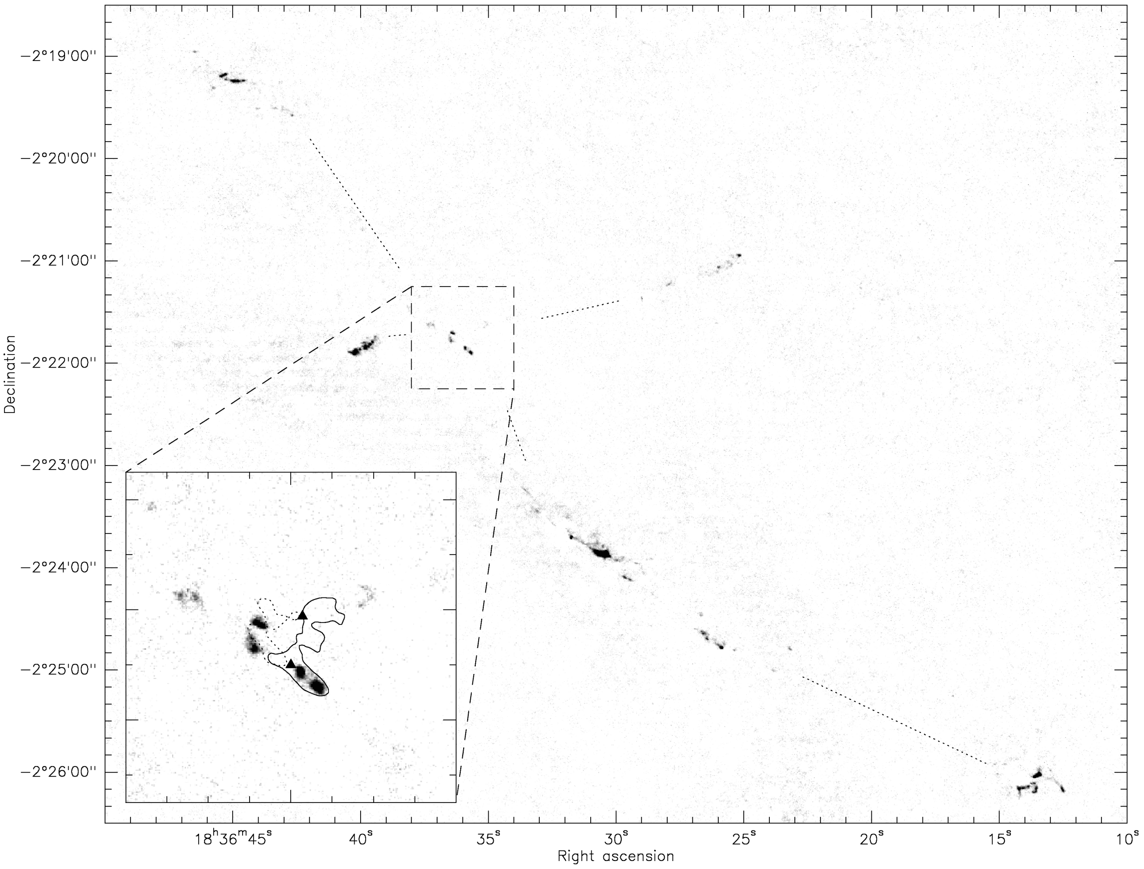

Figure 4.3: $H_2$ ($\lambda = 2.122\,\mu$m) emission map towards ISOSS J18364-0221. The dotted lines indicate the proposed connection of the emission features to the different outflow lobes. The inlay shows a magnification of the region around SMM1. The positions of the SMM1 North and South cores are marked with filled triangles, and the CO(2-1) line wing emission of the red (dotted contour, $2.5\,\mathrm{Jy\,beam^{-1}\,km\,s^{-1}}$) and blue (solid contour, $3.5\,\mathrm{Jy\,beam^{-1}\,km\,s^{-1}}$) molecular outflow lobes are over-plotted (cf. Fig. 4.2 top row).

### 4.3.2 SEDs and core sizes

In the J, H, K bands, and at 3.6 $\mu$m no emission is coinciding with SMM1 North or South and upper flux limits were derived from the maps. Close to SMM1 North, the emission in the 4.5 and 5.8 $\mu$m IRAC bands were measured on levels of 71 and 155 $\mu$Jy. In the 4.5 $\mu$m band there is extended emission overlapping with the SMM1 South position, where the flux is about 1.2 mJy. At 8 $\mu$m no counterparts corresponding to SMM1 North or South are detected.

The source towards SMM1 South clearly dominates the emission at 24 and 70 $\mu$m. Due to the separation of about $9''$ between SMM1 North and South, the derivation of fluxes at these wavelengths is impaired towards SMM1 North (PSF FWHM of about $6''$ and $17''$). The emission of SMM1 South was removed via PSF subtraction. At both 24 and 70 $\mu$m the residual maps do not reveal a second compact source at SMM1 North. The $3\sigma$ upper limits for SMM1 North were derived from the residual scatter at its position. The resulting fluxes are 199 mJy and 15.7 Jy for SMM1 South and upper flux limits of 5.3 mJy and 177 mJy for SMM1 North at 24 and 70 $\mu$m respectively.

To derive submillimetre fluxes for the two internal SMM1 components, Gaussians were fitted to each peak on the 450 $\mu$m map and in addition one extended Gaussian to account for the surrounding clump emission. The same sizes convolved with the $14''$ Gaussian were then used as fixed parameters to extract 850 $\mu$m fluxes. The clump background is well fit with a deconvolved FWHM size of $68''$ and total fluxes of 12.3 Jy (450 $\mu$m) and 2.02 Jy (850 $\mu$m). For SMM1 South the deconvolved FWHM size is $5.9''$ and the fluxes are 4.42 Jy (450 $\mu$m) and 622 mJy (850 $\mu$m), and for SMM1 North a size of $7.0''$ and fluxes of 2.66 Jy (450 $\mu$m) and 476 mJy (850 $\mu$m) was found. The total fluxes are higher than those given in Birkmann *et al.* [2006] because the background was fitted over a larger region and thus includes more extended emission. As in the 850 $\mu$m map (Fig. 4.1), SMM1 North and South blend into a single elongated maximum in the single-dish 1.2 mm map. Therefore the fluxes were extracted in the same way for both sources, using the positions from the submillimetre and allowing for a pointing offset. The derived fluxes are 151 mJy for SMM1 South and 156 mJy for SMM1 North.

The continuum fluxes for both cores are listed in Table 4.1. Fig. 4.4 shows the spectral energy distributions of the continuum emission towards the two sources including the jet features in the IRAC bands. The curves fitted to the data are described in the next subsection.

Also from the interferometric continuum maps fluxes for both sources have been derived by fitting Gaussian components. In the case of SMM1 South, 80 mJy (1.3 mm) and 4.1 mJy (3.4 mm) and FWHM dimensions of $4.4'' \times 3.6''$ (PA -50°) were measured, corresponding to a core size of $\sim$9000 AU. For SMM1 North the fluxes are 49 mJy (1.3 mm) and 3.9 mJy (3.4 mm) and FWHM sizes of $6.3'' \times 3.1''$ (PA 34°) were measured, corresponding to a more elliptical core of $14000 \times 7000$ AU.

The bolometric luminosities were estimated from the two SEDs. SMM1 South has a luminosity $L \approx 180\,L_\odot$, and SMM1 North exhibits $L \approx 20\,L_\odot$ using the upper limit fluxes in the infrared.

### 4.3.3 Dust temperatures and masses

Ossenkopf and Henning [1994] have derived dust opacities for dense protostellar cores. For the analysis the model with thin ice mantles and coagulation at a gas density of $n_H = 10^6\,\mathrm{cm}^{-3}$ (OH5, $\kappa_{1.3\mathrm{mm}} = 0.9\,\mathrm{cm}^2\,\mathrm{g}^{-1}$) was used. To estimate the temperature uncertainties, also applied the model without ice mantles (OH2) and the initial, non-

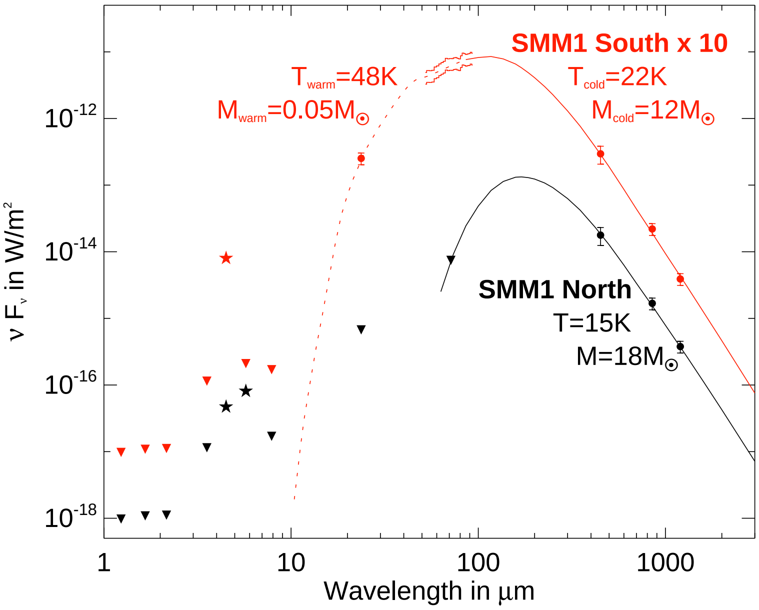

Figure 4.4: Spectral energy distributions of ISOSS J18364-0221 SMM1 North (black) and South (red, scaled up by 10). Upper limits are indicated by triangles. The dots represent the data points obtained with SCUBA (850 and 450 $\mu$m) and MIPS (24 $\mu$m). Histogram-like bars show the error range of the MIPS SED spectrophotometry (53 to 93 $\mu$m) for SMM1 South. Stars represent emission in the IRAC bands (3.6, 4.5, 5.8 and 8.0 $\mu$m) associated with the core positions that stems from jet features (see text). The J, H and Ks bands were observed with Omega-2000. The lines represent fits to the SEDs via modified Planck components (see text).

coagulated opacities (OH1) was applied. Fig. 4.4 shows the OH5 fit to the emission of SMM1 South using two modified Planck components assuming optically thin emission. The long-wavelength SED is matched by thermal dust emission at $22^{+4}_{-1}$ K (solid line). A dust mass of $M_d^{cold} = 0.12\,M_\odot$ results from the fit. The fluxes at shorter wavelengths are reproduced by a dust component at 48 K with a dust mass of $M_d^{warm} = 5 \times 10^{-2}\,M_\odot$ (dashed line). For the SMM1 North source the upper flux limit at 70 $\mu$m was used to derive an upper limit dust temperature of $15^{+1}$ K from a single component fit also shown in Fig. 4.4. The corresponding dust mass is $M_d = 0.18\,M_\odot$. Assuming a canonical gas-to-dust mass ratio of 100, the masses of the cores are ca. $12\,M_\odot$ (SMM1 South) and $18\,M_\odot$ (SMM1 North), with an uncertainty of about a factor two (see 4.4.2).

Preserving the dust temperatures and masses, the expected continuum fluxes at 3.4 mm are 4.9 mJy (SMM1 South) and 4.8 mJy (SMM1 North), thus the measured fluxes trace about $10\,M_\odot$ for SMM1 South and about $15\,M_\odot$ for SMM1 North as compact components. The differences stem from the filtering in the interferometric observations. Using these masses and the core FWHM sizes of 9000 AU and 10000 AU, volume-averaged densities $\langle n_{H_2} \rangle$ can be calculated from $\langle n_{H_2} \rangle = 3M/(4\pi\,FWHM^3)$. They are $4 \times 10^5\,cm^{-3}$ for SMM1 South and $5 \times 10^5\,cm^{-3}$ for SMM1 North. The remaining mass of the SMM1 clump is located in a more extended envelope. From the dust temperatures and peak fluxes in the interferometric 1.3 mm continuum map the peak column densities are $2.7 \times 10^{23}\,cm^{-2}$ (SMM1 North) and $2.4 \times 10^{23}\,cm^{-2}$ (SMM1 South). Table 4.1 summarises the properties of the two detected cores.

| Parameter | SMM1 North | SMM1 South |
|---|---|---|
| 24 $\mu$m flux (mJy) | <5.3 | 199 |
| 70 $\mu$m flux (mJy) | <177 | 15700 |
| 450 $\mu$m flux (mJy) | 2660 | 4420 |
| 850 $\mu$m flux (mJy) | 476 | 622 |
| 30m 1.2 mm flux (mJy) | 156 | 151 |
| PdBI 1.3 mm flux (mJy) | 49 | 80 |
| PdBI 3.4 mm flux (mJy) | 3.9 | 4.1 |
| FWHM size (AU) | 14000×7000 (PA 34°) | 10000×8000 (PA -50°) |
| Luminosity ($L_\odot$) | 20 | 180 |
| Dust temperature[a] (K) | 15 | 22 |
| $N_{H_2}^{peak\,b}$ ($cm^{-2}$) | $2.7 \times 10^{23}$ | $2.4 \times 10^{23}$ |
| Mass[c] ($M_\odot$) | 15 | 10 |
| $\langle n_{H_2} \rangle$ ($cm^{-3}$) | $5 \times 10^5$ | $4 \times 10^5$ |

[a] Derived from the single-dish continuum flux measurements or upper limits between 70 and 1200 $\mu$m.

[b] Derived from the interferometric 1.3 mm continuum map and the given dust temperatures.

[c] Derived from the interferometric 3.4 mm continuum map and the given dust temperatures.

Table 4.1: Continuum flux measurements and derived core properties.

### 4.3.4 Properties of the molecular outflows

From the CO(2-1) map the properties of the outflows were inferred. For this purpose it is necessary to convert the measured CO emission into molecular hydrogen column densities $N_{H_2}$, and the relation $N_{H_2} = 3 \times 10^{20}\,cm^{-2}\,K^{-1}\,km^{-1}\,s \times \int T_{mb}\,dv$ from Osterloh *et al.* [1997] was used. The mass was then calculated as $M = \mu m_{H_2} d^2 \sum N_{H_2} \Delta\Omega$, where $\mu$ is the ratio of gas mass to hydrogen mass (taken to be 1.36), $m_{H_2}$ is the mass of the hydrogen molecule, and $\Delta\Omega$ is the solid angle covered by $N_{H_2}$. The integrated emission in the CO map towards SMM1 traces $4.8\,M_\odot$, compared to a mass of $75 \pm 30\,M_\odot$ derived from the dust continuum emission [Birkmann *et al.*, 2006]. This discrepancy probably stems from the uncertainty of the above relation in combination with the missing flux in the CO map (see 4.2.4). Apparent also in the integrated CO(2-1) spectrum in Fig. 4.2, the optical depth in the line is significant. Other outflow studies have found CO(2-1) optical depths on the order of 10 referring to a comparison with $^{13}$CO emission as described in Choi *et al.* [1993]. In the case of SMM1 South, the fact that near-infrared $H_2$ emission is observed towards both molecular outflow lobes indicates that the difference in extinction is not very large. This suggests a high inclination $i$ of the outflow axis with respect to the line-of-sight. Because it is not possible to further constrain the inclination, $i = 57.3°$ is assumed for both outflows in the following, corresponding to the mean of a random distribution of outflow orientations. Table 4.2 lists the parameters derived as described in Henning *et al.* [2000a] for the different outflow lobes, corresponding to line emission above $3\sigma$. Mean outflow velocities were derived from the mechanical momenta P and the masses using $<v>=P/M$, and halves of the lobe extents in outflow direction were taken as travelled distance to calculate the dynamical timescales. The given masses represent lower limits, and as described in 4.2.4, the true masses are probably higher by roughly a factor of five. The same applies to the mechanical momenta and the kinetic energies. While the mass derivation may be precise within factors of 2 to 4 [cf. Cabrit and Bertout, 1990], the dynamical parameters are less certain and can be considered as order of magnitude estimates. Besides, the blending of the two red outflow lobes hampered the parameter derivation, so the values derived for the blue lobes are regarded more precise.

| Outflow Parameter | South Red Lobe | South Blue Lobe | North Red Lobe | North Blue Lobe |
|---|---|---|---|---|
| Proj. Velocities ($km\,s^{-1}$) | 40…50 | 20…30 | 40…50 | 20…30 |
| Solid Angle ($as^2$) | 86 | 195 | 27 | 119 |
| Mass[a] ($M_\odot$) | 0.066 | 0.15 | 0.023 | 0.12 |
| Mech. Momentum[b] ($M_\odot\,km\,s^{-1}$) | 0.85 | -2.3 | 0.30 | -1.8 |
| Kin. Energy[b] (J) | $1.7\times10^{38}$ | $2.5\times10^{38}$ | $1.8\times10^{38}$ | $2.4\times10^{38}$ |
| Dyn. Timescale[b] (yr) | $7.7\times10^{3}$ | $7.0\times10^{3}$ | $3.8\times10^{3}$ | $5.8\times10^{3}$ |
| Mass Outflow Rate[b] ($M_\odot\,yr^{-1}$) | $8.6\times10^{-6}$ | $2.1\times10^{-5}$ | $6.0\times10^{-6}$ | $2.1\times10^{-5}$ |
| Mech. Luminosity[b] ($L_\odot$) | 1.8 | 2.9 | 3.9 | 3.4 |

[a] Masses are lower limits because of missing flux.

[b] Assuming an inclination $i = 57.3°$ of the outflow axes.

Table 4.2: Outflow parameters derived from the CO(2-1) map.

### 4.3.5 HCN emission towards SMM1

The three HCN(1-0) hyperfine components $F_{1\rightarrow1}$, $F_{2\rightarrow1}$, and $F_{0\rightarrow1}$ lie within 4 MHz and the expected line ratios are 3:5:1 in the optically thin case for local thermal equilibrium (LTE). The HCN(1-0) map integrated over all three components (Fig. 4.5 left) shows a pronounced maximum towards SMM1 South, whereas only weak emission is detected at SMM1 North. It is possible that the minor peaks that are offset from SMM1 North stem from the molecular outflows, because it has been shown recently that HCN can be present there as well [Zhang *et al.*, 2007]. The HCN(1-0) spectra towards the centre positions of SMM1 South and North are shown in the middle panels of Fig. 4.5.

In the case of SMM1 North, the signal-to-noise ratio of HCN(1-0) is rather low ($\approx 6$) and the line shapes are uncertain. As indicated in the plot, the positions of the peaks are consistent with a systemic velocity $v_{LSR} = 36.1\,km\,s^{-1}$. The observed line ratios (neglecting the noise) depart from the expected optically thin LTE ratios: $F_{0\to1}/F_{2\to1} = 0.6$ and $F_{1\to1}/F_{2\to1} = 0.75$ compared to 0.2 and 0.6 in the LTE case. Such hyperfine "anomalies" have also been observed towards star-forming clouds in the past [Walmsley *et al.*, 1982]. Gonzalez-Alfonso and Cernicharo [1993] have investigated this numerically and found that the velocity structure in the emitting cloud core could strongly affect the line ratios. In particular, they found that an increased $F_{1\to1}/F_{2\to1}$ ratio indicates inward motion in the core. Line ratios similar to the SMM1 North spectrum were predicted for a subset of their models.

In the case of SMM1 South the HCN(1-0) spectrum is detected with a higher signal-to-noise ratio of up to 40. Fitting the line wings with a symmetric profile results in $v_{LSR} = 34.8\,km\,s^{-1}$. The hyperfine components are characterised by complex line shapes and cannot be described within the optically thin LTE approximation. The main features of the line profiles are strong dips near the line centres. In essence, such dips can be interpreted: 1) as an artifact of the data combination, i.e. the short-spacing flux is not recovered when combining the interferometric and single-dish data; 2) as a physical effect, namely, as a result of the self-absorption of the internal radiation in the envelope. To illustrate that this is not an artifact of data reduction, the single-dish and interferometric HCN(1-0) spectra (integrated over $20'' \times 20''$) before their combination are shown in the right panels of Fig. 4.5. If the dips in the interferometric spectrum are a result of the missing short-spacing flux, then prominent emission should arise near the line centres in the single-dish data. However, both interferometric and single-dish spectra have strong dips that indicate that these line features are real.

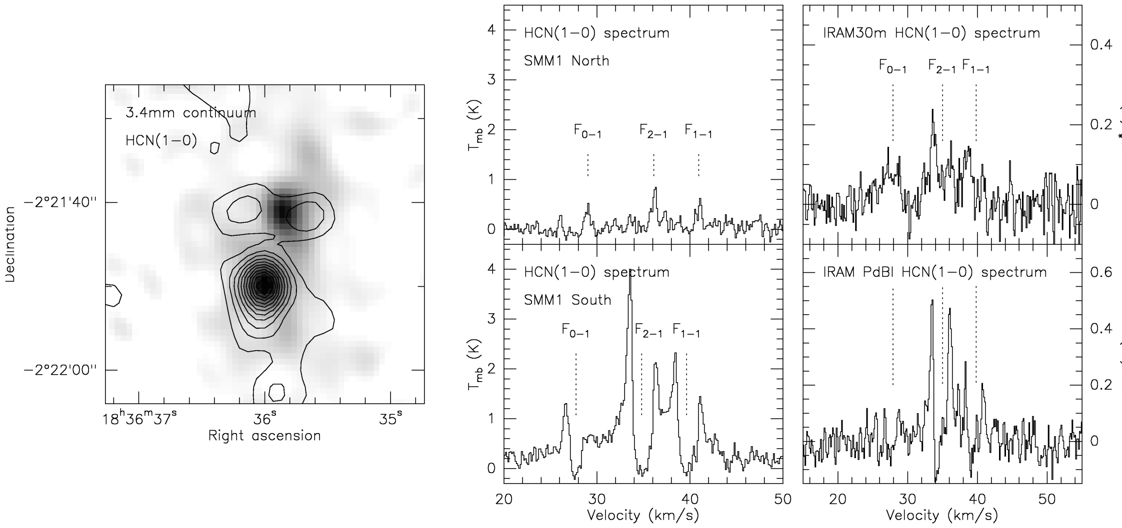

Figure 4.5: ISOSS J18364-0221 SMM1 HCN(1-0) observations. Left panel: The 3.4 mm continuum emission is shown in grey-scale, and the contours give the integrated HCN(1-0) line emission at 0.1, 0.2, ..., 1.1 $Jy\,beam^{-1}\,km\,s^{-1}$. The middle panels show the HCN(1-0) spectra towards SMM1 North and South. The hyperfine components are marked for $v_{LSR} = 36.1\,km\,s^{-1}$ (SMM1 North) and $v_{LSR} = 34.8\,km\,s^{-1}$ (SMM1 South). In the right panels the IRAM 30m single-dish spectrum and the IRAM PdBI spectrum before combination are plotted. There, the hyperfine components are marked for $v_{LSR} = 35\,km\,s^{-1}$.

## 4.4 Discussion

### 4.4.1 The fragmentation and column density of the SMM1 clump

The presented observations reveal two major fragments towards the SMM1 clump. Its mean FWHM extent of 30000 AU [Birkmann *et al.*, 2006] gives a volume-averaged density of $n_{H_2} = 9 \times 10^4\,cm^{-3}$ for SMM1. The dust temperature of 16.5 K gives a Jeans length of about 17000 AU and a Jeans mass of $0.7\,M_\odot$ [Stahler and Palla, 2005]. This indicates that the two cores with masses more than one magnitude higher are not the direct result of thermal fragmentation, because one would then expect a number of cores with about one Jeans mass to form [e.g. Jappsen *et al.*, 2005; Bonnell *et al.*, 2006]. The projected distance of the two cores is 21000 AU. It is rather large compared to the radius of influence of radiative feedback from protostellar objects. The simulations of Krumholz *et al.* [2007] show that the latter is around 1000 AU in the first 20000 yr of core collapse. This suggests that the two cores evolve individually in terms of radiative feedback, however a kinematic influence is not excluded. Krumholz and McKee [2008] proposed a lower column density threshold of $1\,g\,cm^{-2}$ ($N_{H_2} = 2 \times 10^{23}\,cm^{-2}$) for the formation of high-mass stars. For the SMM1 clump the peak column density of $7 \times 10^{22}\,cm^{-2}$ was derived from the single-dish 1.2 mm map peak flux. It does not reach the proposed limit. However, the core peak column densities lie beyond the threshold (see Table 4.1). This shows that observations with high spatial resolution are required to evaluate the core properties.

### 4.4.2 Properties of the two millimetre cores

#### Uncertainty of the core masses

The two detected cores SMM1 North and South appear quite similar at long wavelengths because they are of nearly the same size and exhibit comparable continuum emission. However, the derived core masses depend crucially on the assigned dust temperatures, and these are determined by the flux levels in the far-infrared. At wavelengths below $\sim 100\,\mu m$ the SMM1 clump of about $75\,M_\odot$ is expected to become optically thick for continuum emission, and the Planck component fit does not take this into account. Therefore, the fitted warm component for SMM1 South is neglected in the rest of the discussion. Also for the cold components, the characteristic dust temperature may have been underestimated. However, because of its mass the far-infrared continuum optical depth of SMM1 is expected to be of the order of unity only. This means that a significantly higher dust temperature, corresponding to a lower mass and in consequence to a lower optical depth, would not be consistent with the far-infrared fluxes. Thus, the resulting uncertainty of the masses are about a factor of two, but the general averaging along the line-of-sight could introduce larger errors. Furthermore, the mass derivation relies on the used dust opacities. While the choice of the OH5 model is rather conservative and the results can be compared to other studies, the true opacities may well differ. In the following, the derived masses are taken at face value.

#### Core properties in comparison to other sources

Both SMM1 North and South are compact and appear to drive individual outflows. Therefore they are suspected to form individual stars or stellar systems of a few. With about 10 and $15\,M_\odot$, SMM1 South and North represent cores of intermediate mass. From the comparison of core and stellar mass distributions, there are tentative indications that the star-forming efficiency on the scales of individual cores is between 25 and 50% [see e.g.

Krumholz, 2008, and ref. therein]. Under this assumption, one would expect both cores to form intermediate-mass protostars or protostellar systems in case none of the surrounding matter enters in the core collapse. However, the latter is probable because of the large-scale collapse motions that have been observed towards SMM1. In comparison to samples of low-mass dense cores, SMM1 North and South are denser by a factor of 10 [cf. Motte *et al.*, 2007]. The peak column density values derived from the interferometric 1.3 mm peak fluxes are regarded as lower limits because of the filtering in the interferometric map. For low-mass dense cores, peak column densities of $10^{23}\,\mathrm{cm}^{-2}$ or lower were reported [Ward-Thompson *et al.*, 1999], so both cores lie above. They rather resemble the objects found in IRDCs by Rathborne *et al.* [2007]. While their sample of four clumps (they used a different nomenclature) have masses of $100\,\mathrm{M}_\odot$ and greater, the small scale cores are several thousand AU in size and their masses are 2 to $21\,\mathrm{M}_\odot$ with the exception of one hot molecular core candidate. As in the case of SMM1 South, $24\,\mu$m sources are associated with those cores. Similar findings have been reported by Beuther and Steinacker [2007] for the more massive core in IRDC 18223-3, in particular the remarkable low luminosity.

#### SMM1 South

The SED of SMM1 South at wavelengths below about $80\,\mu$m (Fig. 4.4) does not resemble the single thermal emission component reproducing the submillimetre and millimetre fluxes. A similar result was also derived in the study of a sample of 12 clumps detected in five other ISOSS star-forming regions (see Chapter 3) and for one core in the ISOSS J23053+5953 region [Birkmann *et al.*, 2007]. Warm and hot dust components are required to explain the emission down to $24\,\mu$m, and also emission from very small grains may contribute in this wavelength regime. The fact that SMM1 South appears as point source at 24 and $70\,\mu$m shows that this core contains a compact region of heated dust. Assuming half of the PSF FWHM ($6''$ at $24\,\mu$m) as an upper limit, the emitting region has a size of less than 7000 AU. This is consistent with an embedded young stellar precursor that constitutes the driving source of the SMM1 South outflow.

#### SMM1 North

SMM1 North lacks emission in the infrared. The only sign of star formation is the SMM1 North outflow, indicating that this core is also further evolved than a supposed prestellar stage. The characteristic dust temperature is constrained to an upper limit, and therefore in this case the derived core mass represents only a lower limit.

#### Relative motion

Regarding the motion of the two cores with respect to each other, their systemic velocities derived from the HCN spectra differ by about $1.3\,\mathrm{km\,s^{-1}}$ and SMM1 North appears to be receding. The estimated uncertainty is $0.5\,\mathrm{km\,s^{-1}}$. Nevertheless, the value is relatively high compared to the velocity dispersions of up to $0.5\,\mathrm{km\,s^{-1}}$ measured for the core-to-core motions e.g. in NGC 1333 and Perseus [Walsh *et al.*, 2007; Kirk *et al.*, 2007]. It corresponds to roughly $0.3\,\mathrm{AU\,yr^{-1}}$, and on a timescale of about $10^5$ yr the cores would cover their projected distance.

### 4.4.3 The star-forming process within the cores

The SEDs of both cores are dominated by the emission at long wavelengths arising from cold dust. This emission does not disclose much information about the internal structure of the cores. The lack of mid-infrared emission and the low spatial resolution in the far-infrared, when compared to the expected scales of emitting regions, do also prevent clarification of the properties of the embedded source in the case of SMM1 South. SMM1 North is very likely less evolved, but projection effects cannot be excluded. More observations are needed to further constrain the star formation process in the detected cores: The core emission morphology in the far-infrared will be explored with the ESA Herschel mission. In the case of SMM1 South, high spatial resolution imaging beyond $20\,\mu$m combined with high sensitivity, possible with the MIRI instrument on JWST, will severely constrain the properties of the embedded protostellar object. In the following, the implications given by the derived outflow properties and the modelling of the HCN spectra are discussed.

### Outflow activity

Collimated outflows have been observed for low-mass cores and, more recently, also for young high-mass objects, supporting the disk accretion scenario [see Beuther and Shepherd, 2005, and ref. therein]. In the former case, a high degree of collimation is linked to early stages and a widening of the outflow opening angle follows during further evolution [Arce and Sargent, 2006]. According to some observational evidence, this holds for high-mass sources as well and may provide a basis for their evolutionary classification.

The fact that rather collimated outflows were observed close to their proposed origins SMM1 North and South is consistent with the idea that the embedded driving sources have formed and launched the outflows recently. This is supported by the estimated dynamical timescales of less than $10^4\,$yr.

The outflow energetics change by orders of magnitude from low-mass cases to luminous high-mass driving sources [e.g. Wu *et al.*, 2004; Henning *et al.*, 2000b], and the span of outflow kinetic energies that have been derived is $10^{31}\,\mathrm{J} \leq \mathrm{E_{kin}} \leq 10^{41}\,\mathrm{J}$. For the sample of Beuther *et al.* [2002c] with $\mathrm{L} > 10^3\,\mathrm{L}_\odot$, they got values on the order of $\mathrm{E_{kin}} \approx 10^{39}\,\mathrm{J}$. With $\mathrm{E_{kin}} \approx 5 \times 10^{38}\,\mathrm{J}$, the outflows of the SMM1 cores reach the same order of magnitude, in particular because the adopted masses are lower limits. They exceed those of low-mass cores.

So far, only the molecular outflows close to the cores have been considered. The traced molecular gas has probably been entrained by collimated jets. Under the assumption that the $\mathrm{H_2}$ emission features at larger distances stem from these jets, which is supported by the rough alignment with the molecular outflows, a second timescale for the outflow activity of the cores can be derived. However, the jet velocities are not constrained from observations. Beuther *et al.* [2002c] used a ratio of jet velocity to molecular outflow velocity of 20, and for the SMM1 cores the resulting jet velocities are about $300\,\mathrm{km\,s^{-1}}$. This is in the range of velocities that have been observed for Herbig-Haro flows from low-luminosity sources [Reipurth and Bally, 2001]. The measured offsets of the outermost $\mathrm{H_2}$ feature in the south-west results in a timescale of approximately $1.8 \times 10^4\,$yr for the SMM1 South jet. This is above the molecular outflow timescale of approximately $7 \times 10^3\,$yr. For the SMM1 North jet, the outermost feature in the west gives a timescale of about $7 \times 10^3\,$yr, which agrees with the molecular outflow timescale. Accounting for the overall uncertainties, these values are consistent with the proposed relation of jets and molecular flows, which of course does not exclude other scenarios.

Parsec-scale jets and outflows have been found towards many young low-mass stellar objects, mostly traced by optical or near-infrared line emission [Reipurth and Bally, 2001]. The more energetic outflows in the high-mass regime are therefore expected to also extend to these sizes, although few observations were reported to date [e.g. Bally, 2008; Beuther *et* *al.*, 2002a]. The presumed jets from SMM1 support this idea. The filamentary and patchy structure observed in $H_2$ can be caused by different factors. Besides the varying line-of-sight extinction, the local $H_2$ abundance may play an important role in determining where the shock-excited emission arises, and the kinematics of internal shocks is presumably influenced by the penetrated medium. An interesting possibility is the connection to the mass ejection history of the driving source, which is linked to the accretion history for disk-driven outflows. The several detected features indicate a varying mass-loss rate for the SMM1 cores. Such a burst mode of accretion may result from disk instability driven by infall [Vorobyov and Basu, 2006].

The S-shape observed for the presumed SMM1 South jet can be interpreted as a precession of the outflow axis. The outermost feature found in the south-west approximately lies on the projected outflow axis with PA $\approx 50^\circ$ that has been derived from the molecular outflow lobes close to the core, while the features in between are offset to lower PA. This means the core rotation axis is not along the line-of-sight, but rather has a high inclination.

### Modelling of the HCN emission

HCN appears to be more resistant to freeze-out in cold dense cores compared to CO-related molecules as $HCO^+$ [Redman *et al.*, 2008]. Assuming that the HCN emission traces the dense gas in the cores, the following investigation explores if the observed HCN(1-0) spectra can be, in principle, reproduced by simple models for the core.

**One-layer model** First, the “one-layer” model was considered where the core is spherically symmetric and homogeneous. The observed spectrum was assumed to stem from the centre of the core as the antenna beam size is little smaller than the spatial extent of the core. The parameters of the model are: the hydrogen density $n_{H_2}$, the temperature $T_{kin}$, the molecular column density $N_{HCN}$, the turbulent velocity $v_{turb}$, and the regular velocity $v_{rad}$ which characterises the radial expansion or contraction of the core. Note that the radius of the core as well as the actual abundance of HCN is not specified since the emergent spectrum for such a core depends on their product [cf. Pavlyuchenkov *et al.*, 2008]. Therefore, in the frame of this model the relative HCN abundance, the radius of the core, or its mass cannot be independently constrained.

Having specified the above parameters, the model core was generated and a line radiative transfer (LRT) simulation with the non-LTE code of Pavlyuchenkov and Shustov [2004] using molecular line data from Schöier *et al.* [2005] was performed. A synthetic spectrum of HCN(1-0) was calculated from the LRT simulation. In principle, the systemic velocity $v_{LSR}$ is an additional parameter. The values of $36.1\,\mathrm{km\,s^{-1}}$ (SMM1 North) and $34.8\,\mathrm{km\,s^{-1}}$ (SMM1 South) derived from the positions of the spectral features were assumed. The consistency between calculated and observed spectra was evaluated with a $\chi^2$-criterion and took into account all the velocity channels of the combined HCN(1-0) spectrum.

To search for the best set of the model parameters, Powell's minimisation algorithm was applied [Press *et al.*, 1992]. This required specified parameter ranges for the search for the best-fit model. The ranges given in the Table 4.3 were used to derive the best-fit parameter sets. The ranges resulted from several runs where parts of the adjacent parameter space were specified and no good reproductions of the observed spectra were found. Though unlikely, the existence of additional compatible sets of parameters cannot be excluded. In order to assure that the minimisation routine was not trapped in a local minimum, the calculations were repeated starting with several sets of initial parameters.

The best-fit spectra obtained for the one-layer model with the corresponding parameters are shown in Fig. 4.6 in the top row.

In the case of SMM1 North, the observed line ratios were reproduced fairly well. A degeneracy occured between the hydrogen density, the kinetic temperature and the HCN column density and therefore $n_{H_2} = 10^5\,cm^{-3}$ was fixed. This resulted in $T_{kin} = 10\,K$ and $N_{HCN} = 7 \times 10^{12}\,cm^{-2}$. Furthermore, given the assumption that the observed HCN(1-0) components are indeed single-peaked and relatively narrow, the effect of the regular and turbulent velocities cannot be distinguished. Therefore, the regular velocity was set to zero. The derived value of the turbulent velocity is $0.4\,km\,s^{-1}$. Note that in contrast to the study of Gonzalez-Alfonso and Cernicharo [1993], it was not needed to introduce regular velocity to explain the "anomalous" line ratios. The obtained ratios naturally appeared as a result of the non-LTE excitation in the subcritical density.

In the case of SMM1 South, the one-layer model could not reproduce the maximal intensities and the strength of the self-absorption dips at the same time. One representative spectrum from the one-layer model is shown in Fig. 4.6.

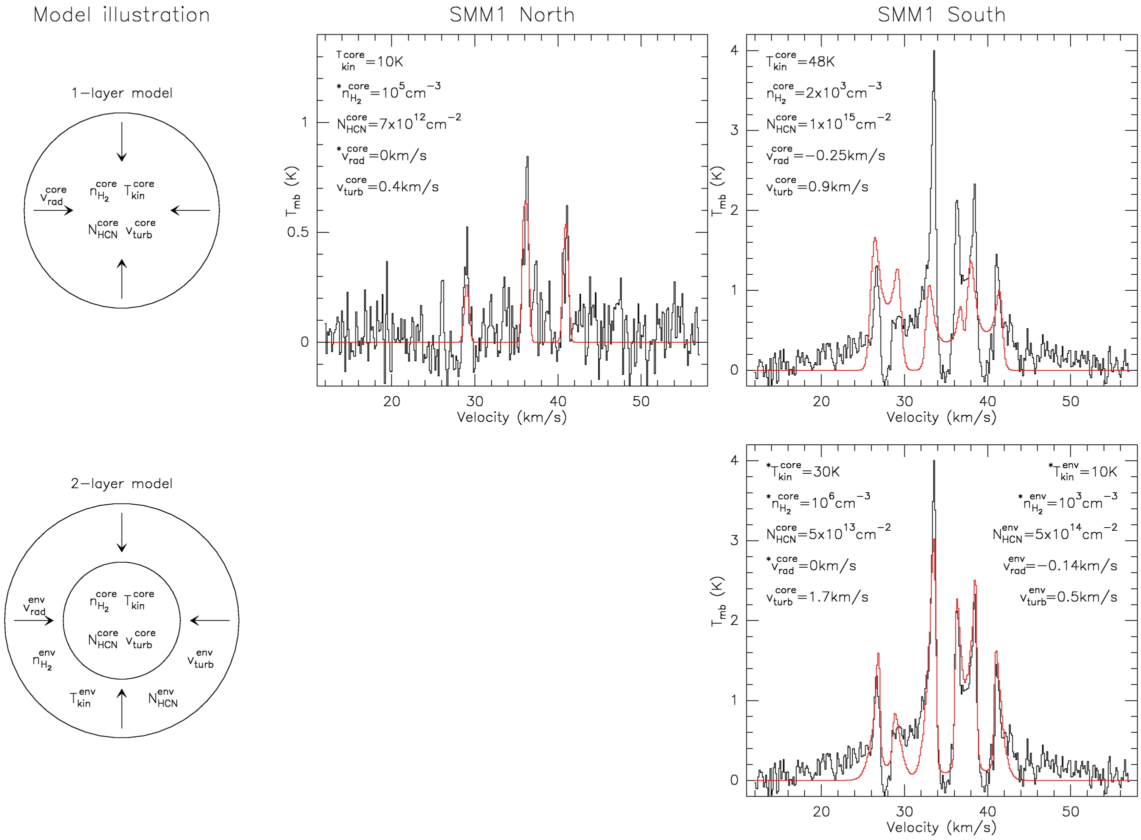

Figure 4.6: Model illustration, observed and modelled HCN(1-0) spectra towards the two SMM1 cores. In the top row, the one-layer model is illustrated and the resulting best fit spectra (red curves) are shown with the corresponding model parameters. The bottom row shows the two-layer model and the resulting best fit of the SMM1 South spectrum (red curve) as well as the corresponding model parameters. Parameters that have been fixed are marked with a preceding asterisk (*).

**Two-layer model** A natural way to reproduce the observed spectrum of SMM1 South is to include a low-density envelope in the model which should lead to self-absorption. This was checked by constructing a "two-layer" model with 5+5 parameters, and chose a configuration where a static core ($v_{rad}^{core} = 0$) is surrounded by a spherically symmetric, homogeneous envelope. The increased number of parameters makes it difficult to identify a best set through the minimisation routine. Therefore some of the parameters were fixed based on the following arguments. First, the assumption that the hydrogen density in the core is higher while in the envelope it is lower than the critical density for HCN(1-0) was made. Given this, the formation of strong self-absorption dips is expected if the HCN column density in the envelope is high enough. The densities were set to $n_{H_2}^{core} = 10^6\,cm^{-3}$ and $n_{H_2}^{env} = 10^3\,cm^{-3}$. The temperature in the envelope was also fixed to $T_{kin}^{env} = 10\,K$, assuming that it is not heated by the inner (most probably warmer) part of the core, for which $T_{kin}^{core} = 30\,K$ was chosen. Changes in the core temperature do not affect the derived model spectra significantly. Thus, the five parameters that were varied are $N_{HCN}^{core}$, $v_{turb}^{core}$, $N_{HCN}^{env}$, $v_{turb}^{env}$, $v_{rad}^{env}$. They were constrained using the minimisation routine.

The best-fit spectrum obtained from the two-layer model is presented in Fig. 4.6 (bottom). The two-layer model could reproduce the intensity, the strong self-absorption dips and asymmetry of the observed spectrum quite well. The line wings may stem from outflowing gas, or also be due to a more complex velocity profile not incorporated in the model. The important outcome of this model can be summarised as follows: First, the strong self-absorption in the line profiles can be reproduced by the high-density core together with the low-density envelope. Second, the asymmetry of the line profiles can be explained by the infalling envelope ($v_{rad}^{env} = -0.14\,km\,s^{-1}$), given the relatively high turbulent velocities in the core ($v_{turb}^{core} = 1.7\,km\,s^{-1}$) and in the envelope ($v_{turb}^{env} = 0.5\,km\,s^{-1}$). However, this configuration is not the only way to fit the line asymmetries. In particular, it is possible to reproduce the line asymmetries by the combination of an expanding core and a static envelope because of the similar relative velocities. This scenario seems implausible, though, because of the short outflow timescales.

Finally, the considered simple models did not reliably constrain the other parameters of the cores, but they illustrated that the observed spectra can indeed be explained theoretically. In order to get more reliable information about the core properties one has to consider a set of molecular lines and transitions together with more physical models of the source. Unfortunately, the available data, in particular the $HCO^+$(1-0) measurements, are not sufficient to enable this. Indeed, if the $HCO^+$(1-0) was used in addition to HCN(1-0) in the fitting routine, two more parameters would be required for the $HCO^+$ abundance (in the core and in the envelope), while $HCO^+$(1-0) alone will not allow to further constrain the excitation conditions. For the latter, at least a few more transitions of $HCO^+$ or its isotopomers were necessary. On the other hand, a more physical model of the core (e.g. with smooth distributions) has more parameters to fit which makes such a model even more uncertain. Thus, the usage of more sophisticated models is required when detailed spectral maps of the sources are available.

### Collapse of SMM1 South

The modelling of the HCN emission showed that the spectrum of SMM1 South can be explained with a collapse of the core. The resulting velocity gives an estimate for the mass infall rate using $dM/dt \approx M/t = M\,v_{in}/r$. For SMM1 South, $v_{in} = 0.14\,km\,s^{-1}$ is the regular velocity of the envelope in the two-layer model. Together with the mass and radius from Table 4.1 this results an infall rate of $3 \times 10^{-5}\,M_\odot\,yr^{-1}$. This is consistent with the mass outflow rates, but is only a crude estimate.

| One-layer Model<br>Parameter | SMM1 North | SMM1 South |
|---|---|---|
| $n_{H_2}$ ($cm^{-3}$) | $10^5$ | $10^3 \ldots 10^5$ |
| $T_{kin}$ (K) | $10 \ldots 50$ | $10 \ldots 50$ |
| $N_{HCN}$ ($cm^{-2}$) | $10^{12} \ldots 10^{15}$ | $10^{13} \ldots 10^{15}$ |
| $v_{turb}$ ($km\,s^{-1}$) | $0 \ldots 1.0$ | $0 \ldots 1.0$ |
| $v_{rad}$ ($km\,s^{-1}$) | $0$ | $-0.25 \ldots 0$ |

| Two-layer Model for SMM1 South<br>Parameter | Core | Envelope |
|---|---|---|
| $n_{H_2}$ ($cm^{-3}$) | $10^6$ | $10^3$ |
| $T_{kin}$ (K) | $30$ | $10$ |
| $N_{HCN}$ ($cm^{-2}$) | $10^{13} \ldots 10^{15}$ | $10^{13} \ldots 10^{15}$ |
| $v_{turb}$ ($km\,s^{-1}$) | $0 \ldots 3.0$ | $0 \ldots 1.0$ |
| $v_{rad}$ ($km\,s^{-1}$) | $0$ | $-1 \ldots 1$ |

Table 4.3: Parameter ranges used in the HCN(1-0) emission modelling for the one-layer and two-layer models.

**Internal turbulence**

Additional parameters obtained from the HCN emission are the internal turbulent velocities of the cores that reproduced the observed line widths. However, in both cases rotational motions, more complex velocity profiles, and also outflows may contribute to the line widths. Such effects were not considered in the considered models. In the case of SMM1 South, the fitted model shows a very turbulent core and less turbulence in the envelope. When compared to the isothermal sound speed of around 0.2 $km\,s^{-1}$ for cold cores ($T \approx 20\,K$), the core turbulence of 1.7 $km\,s^{-1}$ is highly supersonic. The turbulent velocity in the envelope of 0.5 $km\,s^{-1}$ is on the scale of the sound speed but still in the supersonic regime. The SMM1 North HCN spectrum indicates a more quiescent state of this core. The linewidths are reproduced with a turbulent velocity of 0.4 $km\,s^{-1}$.

## 4.5 Summary and conclusions

In this chapter, the onset of star formation in the massive cold clump ISOSS J18364-0221 SMM1 was investigated. The derived results regarding the clump fragmentation, the core and outflow properties, and the collapse indications are summarised as follows:

1. Two compact, embedded cores are the only objects identified. Thus, this clump shows little fragmentation, but seems to rather produce a low number of compact objects.

2. The cores dubbed SMM1 North and South are of about 10000 and 9000 AU radius. The dust temperatures are 15 and 22 K and they have masses of about 15 and 10 $M_\odot$, respectively. SMM1 South harbours an infrared source not detected at 8, but at 24 and 70 $\mu$m. The luminosity of SMM1 South is about 180 $L_\odot$ and a molecular outflow is detected in its vicinity. SMM1 North lacks infrared emission, but a second molecular outflow is emerging from this core. The luminosity of SMM1 North is approximately 20 $L_\odot$. Both outflows appear collimated, and the lower outflow mass limits of about 0.2 and 0.3 $M_\odot$ of presumably entrained gas, and mass outflow rates

of about $4 \times 10^{-5}\,\mathrm{M}_\odot\,\mathrm{yr}^{-1}$ were derived. Fig. 4.7 schematically illustrates these results.

3. Filaments of shock-excited $H_2$ emission at $2.122\,\mu$m towards the lobes of the SMM1 South molecular outflow was detected, and also at distances up to 4.6 pc from SMM1. Each filament is roughly aligned with one of the outflow axes. They are possibly tracing the outflow-generating jets, and the dynamical timescales are consistent with those of the molecular outflows considering the uncertain jet velocities. For both molecular outflows, ages of less than $10^4$ yr were found.

4. SMM1 South is bright in HCN(1-0) and the modelling results support that the core is collapsing. The infall velocity is fitted to $0.14\,\mathrm{km\,s}^{-1}$. This results in a mass infall rate estimate of $3 \times 10^{-5}\,\mathrm{M}_\odot\,\mathrm{yr}^{-1}$. For both cores the spectra can be interpreted with turbulent internal motions, and in the case of SMM1 South the innermost part appears highly supersonic.

Both SMM1 North and South are of intermediate mass, but are embedded in the contracting $75\,\mathrm{M}_\odot$ SMM1 clump. The presence of a $24\,\mu$m source, a very turbulent central region and the jet features at large distances to the core support that SMM1 South is more evolved than SMM1 North. It probably harbours an embedded young stellar precursor that constitutes the driving source of the outflow. The outflows as well as the infall indicate that it is accreting. The associated outflow indicates that SMM1 North is also a star-forming core, and the outflow energetics are similar. However, the forming object remains undetected, and the relatively low level of turbulence implies that it has only marginally affected the surrounding core. When compared to the classification generally adopted for low-mass cores (Figure 1.1), both cores represent analogues of the Class 0 stage. Forbrich *et al.* [2008] have discovered a similar double protostellar system, but scaled down to intermediate masses of 1.2 and $3.5\,\mathrm{M}_\odot$. This system presumably bridges the gap from Class 0 low-mass cores to the discussed cores. The presumed difference in evolution of the forming objects contrasts with the similar sizes, densities and outflow properties of the cores. These findings suggest a rapid evolution of the luminosity as predicted for high accretion rates [Yorke, 2008].

In comparison to the core collapse simulations of Krumholz *et al.* [2007], the luminosity of SMM1 South would be reached at a stage where the embedded protostellar mass is around $0.3\,\mathrm{M}_\odot$. Accretion onto the protostar is the dominant luminosity source, and they find an accretion rate on the order of $10^{-4}\,\mathrm{M}_\odot\,\mathrm{yr}^{-1}$ from directly after the formation of the protostar until this stage. The resulting timescale of about 3000 yr is consistent with the outflow timescales. Also the mass outflow rate as well as the infall rate estimate may be consistent with the high accretion rate. SMM1 North is less luminous, and hence the protostellar mass would be even lower, but may still be consistent with a high accretion rate in their model. However, the formation of outflows is not incorporated therein. This comparison supports that the two cores harbour protostellar seeds that may become intermediate- to high-mass stars. Together with the examples of IRDC 18223-3 and ISOSS J23053+5953 SMM2, ISOSS J18364-0221 SMM1 can be assigned to the sparsely explored stage of massive clumps at the onset of star formation, exhibiting low luminosities but accreting and driving outflows.

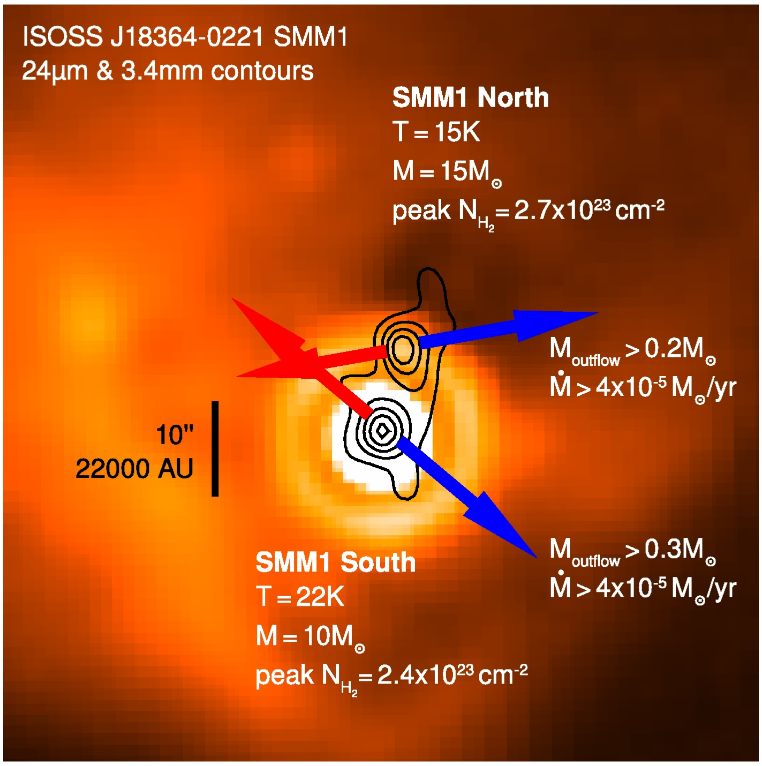

Figure 4.7: Schematic illustration of the identified cores, the corresponding outflows, and their properties. The 3.4 mm contours are plotted above the 24 $\mu$m emission (cf. Fig. 4.1).

# Chapter 5

# Mid-infrared spectroscopy towards young massive clumps

## 5.1 Motivation and target selection

As presented in the previous chapters, the majority of the cold clumps present in the ISOSS star-forming regions appear to harbour protostellar objects, in particular traced by 24 $\mu$m emission. Several of the clumps provide a large mass reservoir and presumably create stellar associations or clusters. A subset of the detected near- and mid-infrared sources may therefore represent young precursors of intermediate- or high-mass stars. The analysis of the infrared colours of sources in five regions described in Chapter 3 supports the presence of such objects. As already discussed there, important properties of the objects like e.g. the extinction towards the central source, the density and temperature structure as well as the dust properties cannot be constrained from the continuum flux measurements without relying on models and empirically defined criteria.

In this chapter the potential of space-based spectroscopic observations in the mid-infrared is explored. Aimed at a characterisation of discovered 24 $\mu$m objects coincident with massive clumps, the observations enable to:

1. Constrain the physical conditions in the inner regions of the massive clumps by means of gas diagnostics.

2. Relate the evolutionary stage of the sources to the properties of its cold envelope and parental star-forming region.

Six objects have been selected that span a large range of infrared flux ratios $F_{24}/F_8$ and $F_{70}/F_{24}$ as listed in Table 5.1. The different colours are thought to represent different evolutionary stages, with higher flux ratios indicating earlier phases. All targets have massive ($M \geq 75\,M_\odot$) and cold ($T \leq 18\,K$) envelopes as inferred from submillimetre dust continuum measurements and milli- to centimetre molecular line observations. In addition, they show indications for large-scale infall traced in $HCO^+$(3-2) and drive outflows, either observed in CO(2-1) or by shocked molecular hydrogen (in the IRAC 4.5 $\mu$m band or in the 1-0 S(1) line at 2.122 $\mu$m) [see Chapters 3, 4, and Birkmann, 2007]. The two sources in the ISOSS J18364-0221 region represent the extrema regarding the flux ratios.

Towards the six targets mid-infrared spectroscopy has been performed using the InfraRed Spectrograph (IRS, Houck *et al.* [2004]) aboard *Spitzer*. The spectra range from 5.2 to 38.0 $\mu$m with low spectral resolution smoothed to R $\approx$ 50, and from 9.9 to 37.2 $\mu$m

| Target Name | Assoc. Clump | Clump Mass ($M_\odot$) | log($F_{24}/F_8$) | log($F_{70}/F_{24}$) |
|---|---|---|---|---|
| 04225+5150 East | SMM1 | 275 | 1.0 | 1.9 |
| 18365-0221 East | SMM1 | 75 | $> 3.6$ | 1.9 |
| 18365-0221 West | SMM2 | 280 | 0.7 | 0.5 |
| 20153+3453 East | } SMM1 | 100 | 1.5 | 1.4 |
| 20153+3453 West | | | 0.5 | 1.0 |
| 23053+5953 East | SMM1 | 200 | 1.7 | 1.6 |

Table 5.1: List of target sources for the IRS observations.

with increased spectral resolution R $\sim$ 600 ("high"). Observational details are given in the next section.

The spectra cover the pure rotational quadrupole transitions of molecular hydrogen at wavelengths of $\lambda = 28.22$, 17.04, and 12.28 $\mu$m for the S(0), S(1), and S(2) transitions, respectively. For densities $n_{H_2} \geq 10^4\,\mathrm{cm}^{-3}$, the lines are thermalised by collisions and their intensity ratios are a sensitive temperature probe for the warm gas component (see Figure 5.4). Combining the low resolution but high signal-to-noise IRS spectra with the existing Spitzer and ground based observations, the SED coverage is significantly improved. Furthermore, dust grain properties and the effects of PAH and silicate features can be investigated.

## 5.2 Observations, data reduction and analysis

IRS has been used in staring mode in order to obtain low and high resolution spectra of the target sources. The observations were performed between July 2006 and April 2008 during the *Spitzer* observing cycles 3 and 4. To cover the maximum possible wavelength interval of 5.2 to 38.0 $\mu$m, all four available low resolution slits SL2, SL1, LL2, and LL1 were used, except for the target ISOSS J18364-0221 East that is not detected at 8 $\mu$m. In this case the short-low second order mode (SL2, 5.2 to 8.4 $\mu$m) was skipped. A signal-to-noise ratio of $\sim$ 100 at a final resolution of $\sim$ 50 in the continuum was reached, providing enough signal in spectral regions that show absorption. For the two targets ISOSS J18364-0221 East and ISOSS J20153+3453 East that show no or very weak IRAC counterparts, a signal-to-noise ratio of 100 could not be achieved at the shorter wavelengths. Here the integration times were chosen to reach a 1 $\sigma$ sensitivity of $\sim$ 0.1 mJy at 8 $\mu$m.

For the diagnostics of the warm gas in the sources, a wavelength coverage from $\lambda = 12.279\,\mu$m for $H_2$ $\upsilon$=0 S(2) to at least $\lambda = 28.221\,\mu$m for $H_2$ $\upsilon$=0 S(0) was required. Thus both high resolution slits short-high (SH, 10.0 to 19.5 $\mu$m) and long-high (LH, 19.3 to 36.9 $\mu$m) were used. Similarly, a signal-to-noise ratio greater than 100 for the LH module at 24 $\mu$m was reached that allows to achieve detections of faint lines above the relatively bright mid-infrared continuum. The integration times for the SH module were adjusted in order to reach a spectral line sensitivity for $H_2$ S(1) at $\lambda = 17.035\,\mu$m that is two times better than the sensitivity for the S(0) line.

All IRS staring mode observations took spectra at two nod positions placing the source at 1/3 and 2/3 of the slit length. The nod direction is always parallel to the long slit dimension, keeping the same slit orientation. One slit position per module is drawn in Figure 5.1 and 5.2.

For the high resolution modules the slit lengths are only 11.3″ (SH) and 22.3″ (LH). This makes a proper determination of the background difficult and thus necessitates ded-

| Target Name | RA/DEC (J2000) | Ramp Times × Cycles | | | | | |
|---|---|---|---|---|---|---|---|
| ISOSS J... | | SH | LH | SL2 | SL1 | LL2 | LL1 |
| 04225+5150 East | 4:22:32.47 +51:50:29.2 | 30s×2 | 14s×2 | 6s×2 | 6s×2 | 6s×2 | 6s×2 |
| 04225+5150 background | 4:22:30.45 +51:49:17.2 | - | 14s×2 | - | - | - | - |
| 18365-0221 East | 18:36:35.98 -02:21:49.9 | 120s×6 | 60s×8 | - | 60s×3 | 30s×2 | 30s×2 |
| 18365-0221 background | 18:36:38.56 -02:22:53.6 | - | 60s×8 | - | - | - | - |
| 18365-0221 West | 18:36:29.49 -02:21:58.5 | 120s×2 | 60s×2 | 6s×2 | 6s×2 | 6s×2 | 6s×2 |
| 18365-0221 background | 18:36:38.56 -02:22:53.6 | - | 60s×2 | - | - | - | - |
| 20153+3453 East | 20:15:21.29 +34:53:45.8 | 120s×3 | 60s×4 | 14s×4 | 14s×4 | 14s×2 | 14s×2 |
| 20153+3453 background | 20:15:15.73 +34:52:42.3 | - | 60s×4 | - | - | - | - |
| 20153+3453 West | 20:15:20.62 +34:53:53.4 | 30s×5 | 14s×5 | 6s×2 | 6s×2 | 6s×2 | 6s×2 |
| 20153+3453 background | 20:15:15.73 +34:52:42.3 | - | 14s×5 | - | - | - | - |
| 23053+5953 East | 23:05:23.71 +59:53:57.1 | 120s×2 | 60s×2 | 60s×3 | 60s×3 | 6s×2 | 6s×2 |
| 23053+5953 background | 23:05:29.69 +59:53:40.4 | - | 60s×2 | - | - | - | - |

Table 5.2: Summary of the IRS observations.

icated background measurements. However, for the SH module the dust continuum flux is determined by the low resolution observations, and the focus lies on the spectral lines on top of the continuum. For the LH module the case is different, because of the so-called "rogue" pixels in the detector array that show an elevated and time-dependent dark current. Although the number of rogue pixels has been reduced by reductions of the detector bias, a separate off-source background measurement is still highly recommended for sources fainter than about 2 Jy. This applies to all the target sources. Thus, dedicated background measurements have been carried out for the LH module, with the same ramp time and number of cycles as for the target sources, subsequent to the target observations. For the low resolution modules a subtraction of the background was accomplished without dedicated background observations, since the slit lengths of about 57″ (SL) and 168″ (LL) are sufficiently large. For additional redundancy to cosmic ray hits and also rogue pixels, at least two cycles were performed for each module. The target positions and exposure times are summarised in Table 5.2.

High accuracy IRS peak-up target acquisition using the blue array (13 to 18.5 $\mu$m) has been requested and successfully accomplished for four targets, but failed for the two targets in the ISOSS J18364-0221 region due to a false positive identification offset from the actual peak-up source. Therefore, those observations were repeated using optical PCRS (Pointing Calibration and Reference Sensor) peak-up acquisition. For the background observations no peak-up was performed.

The BCD provided by the SSC was the basis for further analysis. To create bad pixel masks and for rogue pixel identification prior to spectrum extraction, the IRSCLEAN_MASK software available from the SSC was used. Spectrum extraction was done with the SMART software [Higdon *et al.*, 2004] and used the accompanying calibration data. For the low resolution modules, the spectra of the individual orders were scaled to match the photometric data at 5.8, 8 and 24 $\mu$m and combined. The high resolution spectra were derived by extracting the full aperture of the respective modules. As described further below, some of the targets comprise multiple sources and prominent extended emission in several bands.

## 5.3 Mid-infrared spectra

Figure 5.3 shows the acquired low resolution spectra. Marks designate the lowest pure rotational $H_2$ transitions and known PAH bands [Draine and Li, 2007]. Several phenomena

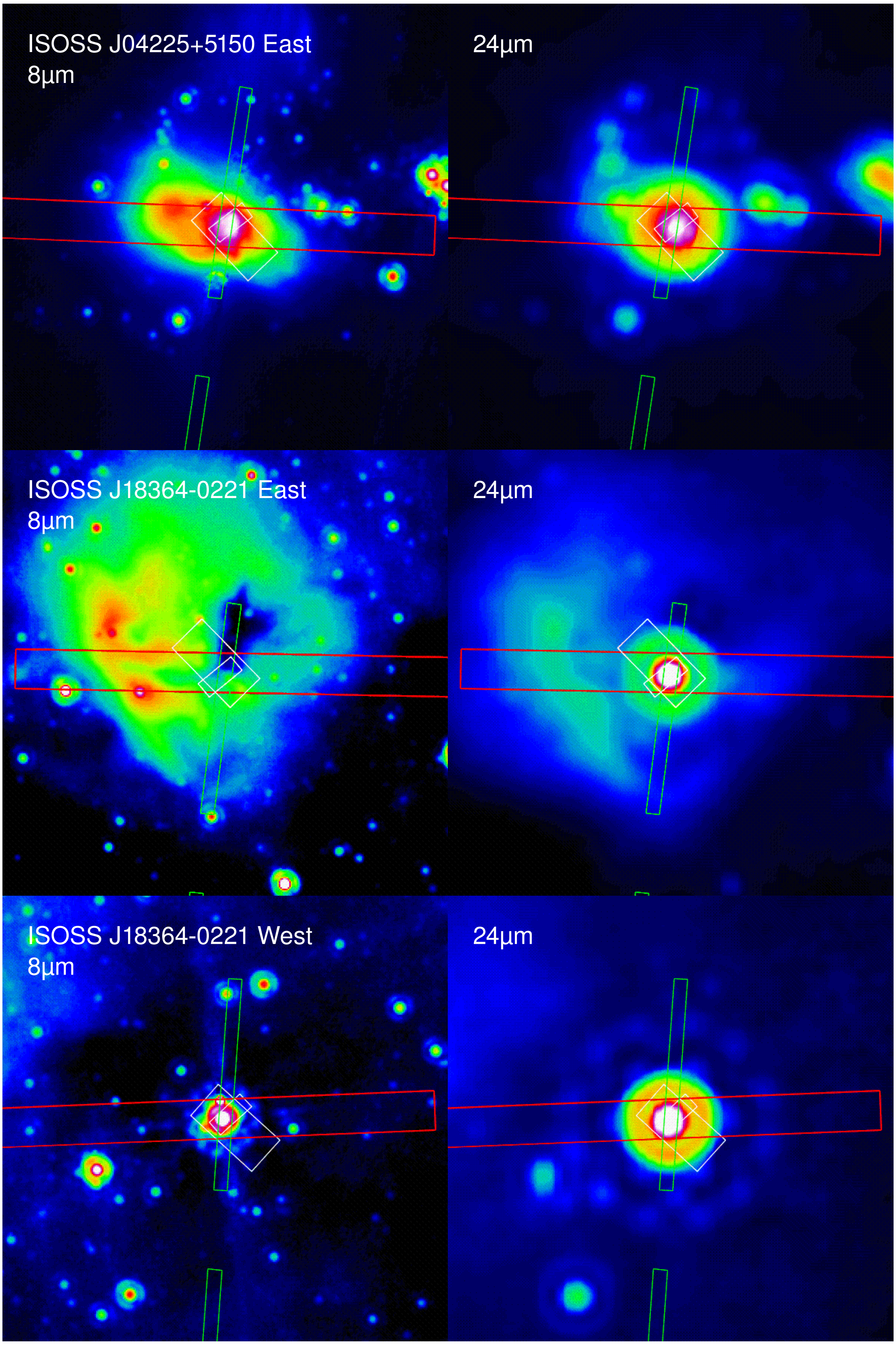

Figure 5.1: IRS slit positions observed towards three ISOSS regions, overlaid on 8 and 24 $\mu$m false-colour images. The low resolution module slits are given in green (SL) and red (LL), the high resolution module slits in white. For clarity, only one slit position per module is shown.

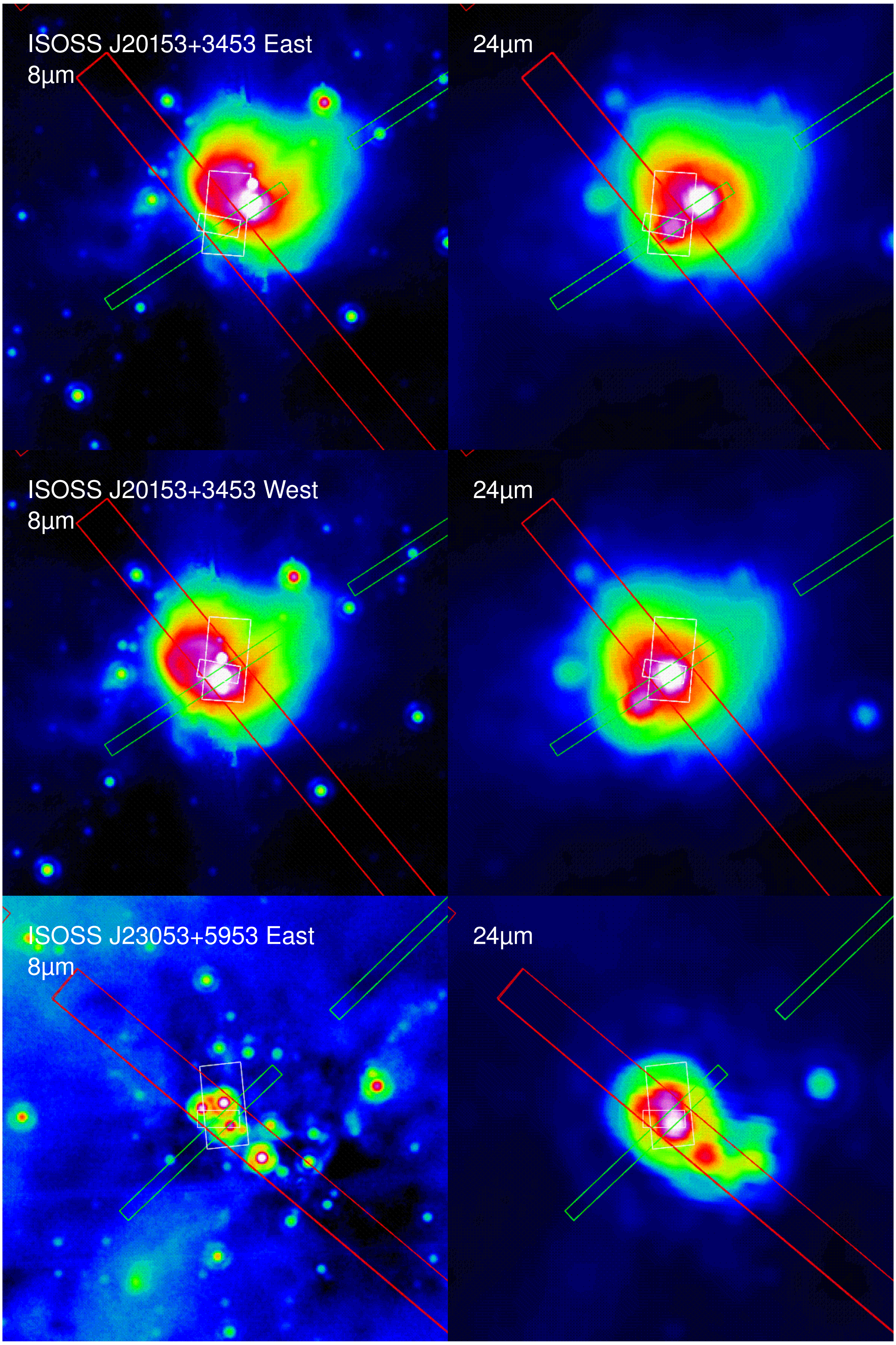

Figure 5.2: Slit positions of the IRS observations towards three ISOSS regions, overlaid on 8 and 24 $\mu$m false-colour images. Same arrangement as in Figure 5.1.

are apparent at the first glance:

- All spectra show strong features between 5 and 20 $\mu$m. The continuum rises steeply at longer wavelengths, except in the case of ISOSS J18364-0221 West. For this target, the continuum flattens beyond about 26 $\mu$m.
- $H_2$ transitions are present in all spectra but for ISOSS J18364-0221 West, where only the 28.2 $\mu$m line shows up clearly.
- The broad spectral features mostly coincide with known PAH bands.
- ISOSS J20153+3453 West is the only target that shows prominent emission in the silicate bands around 9.7 $\mu$m, whereas the other spectra show absorption.
- An absorption feature is present at about 15 $\mu$m in every spectrum, presumably attributed to solid $CO_2$ in ice mantles on dust grains.
- The spectra of ISOSS J04225+5150 East and J20153+3453 East appear very similar, in particular the PAH and $H_2$ emission.

In the following sections some of these aspects are analysed in more detail.

## 5.4 Continuum emission

At the shorter wavelengths, the continuum emission is difficult to entangle from the broad spectral features present in all spectra. This is least severe for the faint ISOSS J18364-0221 East target source. Beyond 20 $\mu$m, the continuum can be determined more reliably.

From the slit positions for the ISOSS J23053+5953 East target given in Figure 5.2 one can see that this clump has already formed a cluster of sources which contribute to the observed spectrum. A fragmentation of this clump into several cores has also been found by the interferometric study of Birkmann *et al.* [2007]. Clustering of embedded sources is also present for the ISOSS J04225+5150 East and the two J20153+3453 sources. For the latter, the 8 $\mu$m map shows artefacts very close to the brightest source in the north. In these cases, the obtained continua trace the warm dust content in the vicinity of the protostars. The steep rise indicates that the sources are embedded in the associated clumps of cold dust traced in the far-infrared and (sub-)millimetre (see Chapter 3).

The two ISOSS J18364-0221 targets appear rather singular (see also Chapter 4), only a faint second 8 $\mu$m source is seen in the south-east of J18364-0221 West. In the 8 $\mu$m map, the nearby peak in the north also represents an artefact produced by the bright target source.

ISOSS J18364-0221 West probably represents the most evolved source in the sample, implied by the low continuum flux ratios in Table 5.1. The continuum emission from this source flattens beyond about 26 $\mu$m. This indicates that it is less embedded in the cold dust of the associated massive SMM2 clump than it is the case for the other targets.

## 5.5 Molecular hydrogen emission

Molecular hydrogen may be excited through several mechanisms. Far-ultraviolet radiation ($\lambda < 91.2$ nm) radiatively pumps the electronically excited states. In the decay to the electronic ground state the high vibrational levels are populated, and the subsequent cascade to $\upsilon$=0 exhibits optical and infrared fluorescent emission. In this case, the level

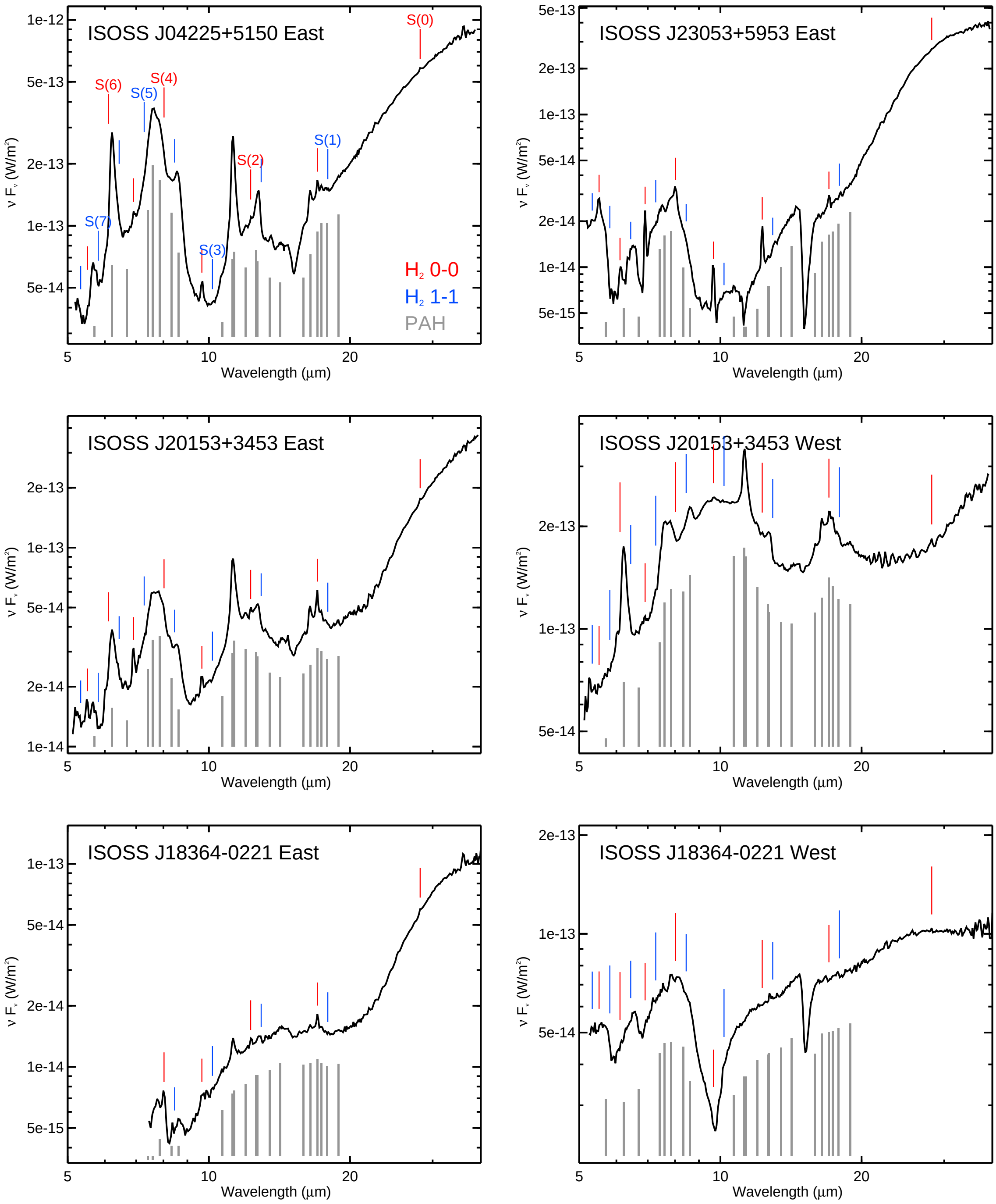

Figure 5.3: Collected mid-infrared spectra. Shown are the combined spectra obtained with the SL and LL modules. The $H_2$ pure rotational transitions for $\upsilon$=0 and $\upsilon$=1 are marked with red and blue lines above the spectra. For clarity, only every other line is labelled. The positions of known PAH features are indicated by grey bars below the spectra.

populations show a characteristic distribution [e.g. Black and van Dishoeck, 1987]. Furthermore, the excitation can be dominated by hard X-rays penetrating into zones that are opaque in the ultraviolet. X-ray sources are young stellar objects or active galactic nuclei. $H_2$ can also be formed in excited states. For the investigated sources, gas densities higher than $10^4\,\mathrm{cm}^{-3}$ are expected. Under these conditions, the dominant excitation at least for the lower energy levels arises from inelastic collisions. Thus, the lowest pure rotational levels remain in thermal equilibrium. These $H_2$ lines are quadrupole transitions with low radiative probabilities and therefore optically thin.

Assuming thermal equilibrium at the temperature $T_{\mathrm{kin}}$, the intensity ratio of two pure rotational transitions is

$$\frac{\mathrm{I}_1}{\mathrm{I}_2} = \frac{\lambda_2\,\mathrm{g}_1\,\mathrm{A}_1}{\lambda_1\,\mathrm{g}_2\,\mathrm{A}_2}\,\mathrm{e}^{\left(\frac{\mathrm{E}_2-\mathrm{E}_1}{\mathrm{k_B T_{kin}}}\right)}$$

with the wavelength $\lambda$ and the statistical factor $\mathrm{g} = (2\mathrm{J}+1)\mathrm{g_N}$ with $\mathrm{g_N} = 1$ for para-$H_2$ (even rotational quantum number J) and $\mathrm{g_N} = 3$ for ortho-$H_2$ (odd J). A represents the spontaneous transition probability and E the upper level energy [e.g. van Dishoeck, 1992].

To evaluate the measured line ratios, the expected line ratios have been calculated for a range of excitation temperatures. Figure 5.4 shows a comparison to the measured line ratios. The three lowest rotational transitions $\upsilon$=0 S(0), S(1), and S(2) have been extracted from five high resolution spectra. For ISOSS J8364-0221 West, only the S(0) line is extracted, while the other two lines are detected with a signal-to-noise ratio of about two only. Thus, the line ratio S(1)/S(0) is constrained to an upper limit. For this analysis, the effect of extinction was not considered, and thus additionally enlarges the uncertainty in the derived line ratios. Depending on the dust model, the extinction ratios for the wavelengths of the utilised $H_2$ lines are about two or less.

The $H_2$ line ratios for the other regions support the presence of warm gas towards the targeted clumps. The S(1)/S(0) ratio is consistent with an excitation temperature of around 150 K in all cases but the two ISOSS J18364-0221 sources. For ISOSS J18364-0221 East, the S(1)/S(0) temperature is about 100 K. The S(2)/S(1) ratio gives between about 450 and 600 K for all targets. The discrepant temperature ranges indicate that the assumption of a single excitation temperature does not hold. Instead, a gas temperature distribution is likely present with temperatures that range up to at least 600 K.

For ISOSS J18364-0221 East, the fact that the lowest temperature was found also supports the youth of this object with respect to the remaining sample. In the the case of ISOSS J18364-0221 West, where only the lowest transition seems to be present, the derived upper limit line ratio cannot be interpreted in the same way. As also suggested by the continuum emission, this source is probably not deeply embedded in the parental clump, and the gas column density traced by the observations is likely lower than in the other cases. The absolute S(0) line flux is about an order of magnitude lower than for the remaining sources.

## 5.6 PAH and silicate features

In a wide variety of sources in our own and external galaxies mid-infrared features attributed to PAHs have been observed [e.g. Peeters *et al.*, 2004]. Locally, PAHs were observed in the diffuse interstellar medium, in dense molecular clouds, in circumstellar envelopes, and in (proto-)planetary nebulae. PAH molecules contain on the order of 50 carbon atoms and thus are considered to form the small end of the dust grain size distribution [Tielens *et al.*, 1999]. They are thought to form an important diagnostics of ultraviolet radiation that excites electronic molecular states. The subsequent decay

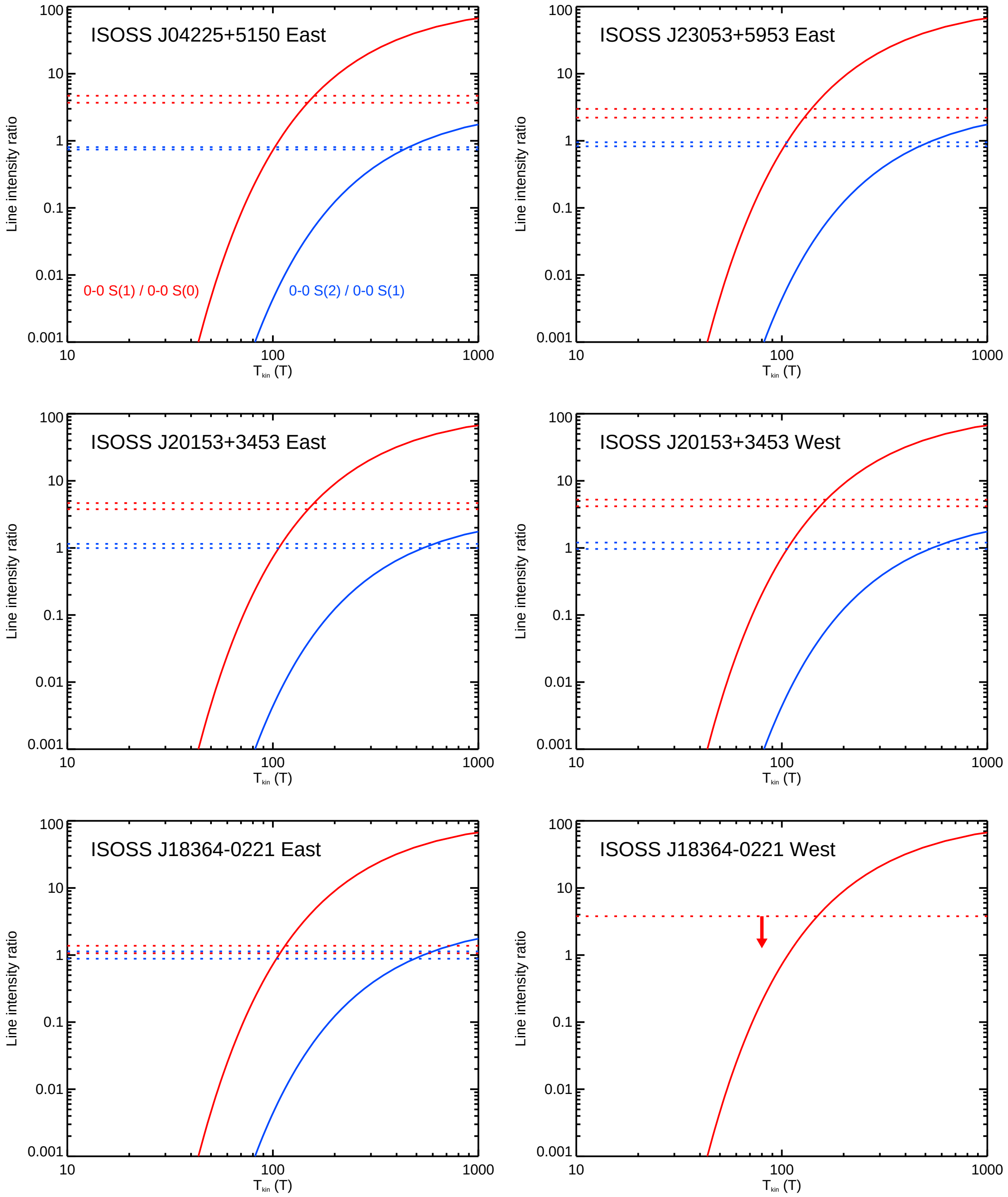

Figure 5.4: Measured line intensity ratios for the $H_2$ transitions $\upsilon$=0 S(1)/S(0) (red) and S(2)/S(1) (blue). The dotted lines give the error range of the measured line ratios. The solid curves give the line ratios as expected in thermal equilibrium for different excitation temperatures $T_{\rm kin}$. For ISOSS J18364-0221 West the S(1) line is tentatively detected only.

results in vibrational emission in the C-H and C-C stretching and bending vibrational modes. The corresponding features are at 3.3, 6.2, 7.7, 8.6, 11.2, 12.8, and 16.4 $\mu$m. In addition, weaker bands have been found [e.g. compiled in Draine and Li, 2007]. Naturally, PAHs also trace the abundance of very small dust grains.

Many of the broad spectral features notably present in the observed spectra at wavelengths below 20 $\mu$m probably arise from PAHs. In particular, the peaks at 6.2, around 7.7, and around 11.2 $\mu$m are prominent in the first four spectra in Figure 5.3. For ISOSS J23053+5953 East, the 11.2 $\mu$m band is present in absorption. From an inspection of the individual images it becomes clear that this is mainly due to bright emission in that band also offset from the source. Thus, the derived background contains this feature and it is subtracted. ISOSS J18354-0221 East shows less prominent features, but the 11.2 $\mu$m peak is also present. In the spectrum of ISOSS J18354-0221 West this feature is weak, although the 7.7 $\mu$m band is present.

The interpretation of these variations from source to source is not straightforward: Observed variations have been attributed to a range of different physical or chemical characteristics of PAHs, including charge state, different subcomponents with varying composition, clustering, molecular structure, etc. [Peeters *et al.*, 2005, and references therein]. For ISOSS J04225+5150 East, J23053+5953 East and the two J20153+3453 sources ultraviolet radiation, probably from young stellar objects, is present. This appears to be less the case for the remaining J18364-0221 sources.

For all sources but ISOSS J20153+3453 West, the silicate band at about 9.7 $\mu$m can be seen in absorption. One possibility to explain this is via line-of-sight effects. In contrast to the other targets, this clump may feature a cavity of low-density material and therefore exhibit little absorption. If one assumes that ISOSS J18364-0221 West represents a more evolved young stellar object with a dispersed envelope, the deep silicate absorption feature would favour an edge-on disk geometry.

## 5.7 Different evolutionary stages

The mid-infrared spectra presented in this chapter provide indications that the observed clump sample comprises different stages of evolution. The results are summarised with respect to each group in the following. The presented analysis covers a part of the possible diagnostics. Additional aspects are beyond the scope of this work, but may further constrain the physical characteristics of the observed sources.

### 5.7.1 Cluster-forming clumps

As mentioned above, ISOSS J04225+5150, J23053+5953 East and the two J20153+3453 sources show a clustering of sources that contribute to the observed spectra. These sources are probably still partly embedded in the parental clump material with dust temperatures below 100 K that leads to the steeply rising dust continua beyond 20 $\mu$m and to the silicate absorption around 9.7 $\mu$m. The differing silicate emission of ISOSS J20153+3453 West may result from a cavity in the line-of-sight.

The $H_2$ line emission implies that also warmer gas is associated. The gas temperature distribution ranges at least to about 600 K. The presence of prominent PAH features indicates that the radiation field contains a copious amount of ultraviolet photons. Furthermore, the abundance of very small dust grains may also contribute to the continuum emission beyond 20 $\mu$m. Such grains can be transiently heated by radiation and emit non-thermally in the mid- to far-infrared [e.g. Rawlings *et al.*, 2005].

### 5.7.2 The young protostellar ISOSS J18364-0221 East source

This source was investigated in detail in Chapter 4. The mid-infrared spectrum arises from an embedded protostellar object that is driving an energetic outflow and accreting. The $H_2$ lines indicate that the gas temperature distribution may be shifted to lower temperatures for this source, but still extends to several 100 K. The general less prominent features attributed to PAHs and silicates also suggest low dust temperatures and a less intense radiation field.

### 5.7.3 The young stellar object ISOSS J18364-0221 West

Though associated with a massive cold clump, the mid-infrared spectrum of this object suggests that it is not deeply embedded therein. The relatively flat continuum at the longer wavelengths might arise from the remaining dispersed envelope and a circumstellar disk. The absence of the $H_2$ transitions at shorter wavelengths is consistent with small amounts of warm or hot gas that may be confined to the inner region of a disk and thus shadowed. Also the prominent silicate absorption suggests an edge-on disk geometry.

# Chapter 6

# Implications for the initial phases of high-mass star formation

The results presented in the previous chapters characterise the star-forming content of a subsample of the massive cold ISOSS regions. In the following, the more general findings are reviewed and put in the context of the early stages of high-mass star formation.

## 6.1 The search for massive prestellar clumps and cores

As outlined in Chapter 1, the observational search for massive prestellar clumps and cores is of crucial importance. Using the ISOSS it was possible to select candidate regions that comprise large amounts of cold dust and are not associated with sources of high luminosity. Evaluated for a subsample, the total masses of the regions are of the order of $1000\,\mathrm{M}_\odot$. As shown in Chapter 3, several cold clumps have been identified with masses above $100\,\mathrm{M}_\odot$. Besides, also clumps of lower masses reside in the investigated regions. Although the average dust temperatures are low, all the clumps exhibit signatures of ongoing star formation. The probably youngest objects identified in this work are the cores in ISOSS J18364-0221 SMM1 (Chapter 4). In the case of the SMM1 North core, the outflow activity is the only evidence for its protostellar nature. These results support that massive prestellar cores, if they exist, are short-lived objects.

## 6.2 Accreting protostellar objects

The onset of star-formation observed in the observed regions has produced a number of mid-infrared sources that are associated with massive clumps. Their near- to mid-infrared emission has been evaluated using radiative transfer models. By these means, several candidates for young protostellar objects, still embedded in their parental clumps, with current masses in the intermediate-mass range were identified. The associated outflow activity implies that they are actively accreting. Already mentioned above, the ISOSS J18364-0221 SMM1 cores presumably are the youngest examples. Having lower protostellar masses, their accretion rates are increased with respect to those of low-mass star-forming cores. It remains unsettled if this also holds for the other sources. Nevertheless, some of them may also represent precursors of high-mass stars and thus members of the previously little explored evolutionary stages before they reach the high-mass regime.

## 6.3 Fragmentation and substructure of massive clumps

The fact that multiple embedded objects were found towards the massive clumps implies that they embody significant density substructure. However, the number of detected sources is not very high for most massive clumps, with the exceptions of the cluster-forming ISOSS J20153+3453 SMM1, J04225+5150 East, and J23053+5953 SMM1 clumps. The detailed study of ISOSS J18364-0221 SMM1 revealed only two embedded cores. No firm overall conclusions on the prevalent fragmentation processes can be drawn from these findings, but they are consistent with the generation of a distribution of core masses beyond the Jeans mass scale.

## Chapter 7

# Upcoming observations with the Herschel Space Observatory

## 7.1 Limitations of previous observations

Though state-of-the-art facilities and instruments have been used, the presented studies are limited mainly by the angular resolution of the observations. In particular, the crucial mid- and far-infrared wavelength regimes propose severe observational challenges: The large mirrors of ground-based telescopes offer high angular resolution, but provide access to very limited atmospheric windows only. In addition, the observable domain is determined by their site and does not cover the whole sky. This drives the development of the next generation of space observatories. An important step in aperture size will be the upcoming ESA Herschel mission with its 3.5 m mirror. This chapter outlines the planned observations addressing the early phases of high-mass star formation in the framework of a key programme.

## 7.2 The Herschel Space Observatory

The ESA Herschel Space Observatory [Pilbratt, 2005, 2008], due for launch in 2009, is expected to provide many new insights into the early phases of star formation. It will operate in the far-infrared to submillimetre wavelength range and use a 3.5 m passively cooled monolithic mirror with low emissivity, the largest mirror built for a space telescope so far (see Figure 7.1). An Ariane 5 rocket will carry Herschel together with ESA's Planck satellite and place them on their separate routes to different orbits around L2. There, Herschel shall observe routinely for at least 3.5 years. A heat shield will prevent direct illumination by the sun and the earth and allow the mirror to cool to about 80 K. Herschel will carry three scientific instruments:

- The Heterodyne Instrument for the Far Infrared (HIFI, de Graauw *et al.* [2005]) covers the two bands 157 to 212 $\mu$m and 240 to 625 $\mu$m with spectroscopy at resolutions around $10^6$. It will collect two polarisations simultaneously.

- The Spectral and Photometric Imaging Receiver (SPIRE, [Griffin *et al.*, 2006]) is a camera that provides simultaneous imaging in three broad bands at 250, 360, and 520 $\mu$m. Furthermore, a Fourier transform spectrometer between 200 and 670 $\mu$m offers a resolution up to 1000 at 250 $\mu$m.

- The Photodetector Array Camera and Spectrometer (PACS, [Poglitsch *et al.*, 2006]) provides imaging photometry between 60 and 210 $\mu$m where two of three bands are observed simultaneously, and integral-field line spectroscopy at a resolution of 1700 in the same range.

The high background from the mirror necessitates chopping for staring observations. Based on the experience with the ISOPHOT focal plane chopper, the chopping mirror mechanism for the PACS instrument [Krause *et al.*, 2006] was developed at the Max-Planck-Institut für Astronomie and the flight hardware was built by Zeiss (Oberkochen).

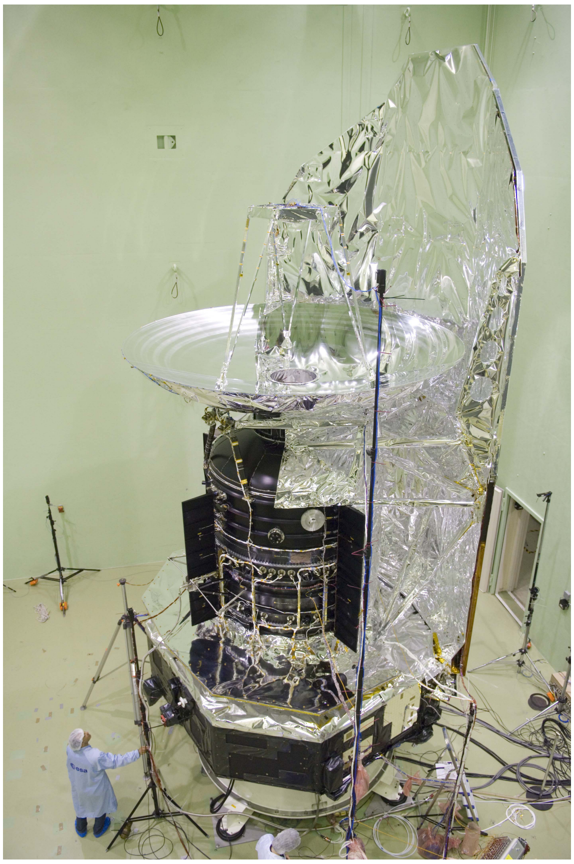

Figure 7.1: The Herschel Space Observatory, being prepared for acoustic tests in June 2008 at ESTEC, Noordwijk, The Netherlands. Photo: ESA.

## 7.3 Planned observations of high-mass star formation

The key programme "The earliest phases of star formation: From low- to high-mass objects" [Krause *et al.*, 2007] utilises the imaging capabilities of PACS and SPIRE to map the far-infrared emission of a unique sample of low- and high-mass target sources. For the high-mass star-forming regions, all possible bands at 75, 110, 170, 250, 360, and 520 $\mu$m will be used to generate maps with sizes between $6' \times 6'$ and $4' \times 14'$ adapted to the source morphologies as seen in the (sub-)millimetre continuum.

PACS employs filled arrays of bolometers, operated at 0.3 K, with instantaneous beam sampling. For the short wavelength bands $4 \times 2$ subarrays of $16 \times 16$ pixels each are combined and the pixel scale is $3.2'' \times 3.2''$. For the long wavelength band, two $16 \times 16$

subarrays are tiled with a pixel scale of $6.4'' \times 6.4''$. The angular resolution with PACS varies from about $5''$ at $75\,\mu$m to around $12''$ at $170\,\mu$m. The SPIRE detectors are arrays of spider-web bolometers, also operated at 0.3 K, with hexagonally packed feedhorns. The number of bolometers are 139 ($250\,\mu$m), 88 ($360\,\mu$m), and 43 ($520\,\mu$m), and the FWHM beams are $19''$, $24''$, and $35''$, respectively. To achieve full spatial sampling over fields of several arcminutes across, either a 64-point jiggle pattern (SPIRE) or scanning at an angle tilted with respect to the array axes (PACS, SPIRE) is necessary. Both instruments will be used in scanning mode. The expected point source sensitivity is about 10 mJy in all bands, corresponding to a sensitivity for cold cores better than about $0.3\,M_\odot$ at distances of 5 kpc. The observational setup is robust against changes in instrument sensitivities and contains a sufficient set of redundant scans.

Figure 7.2 shows an example layout of the observations. The target list of the programme comprises 16 ISOSS regions including those studied in the previous chapters, and the preparation of parts of this programme was undertaken in the course of this thesis. Also the technical aspects of the planned observations have been devised and implemented. In addition to the ISOSS regions, promising sources selected from IRDC samples and sources detected in regions associated with accreting high-mass stars are included. For all targets valuable data sets that complement the Herschel observations have been acquired.

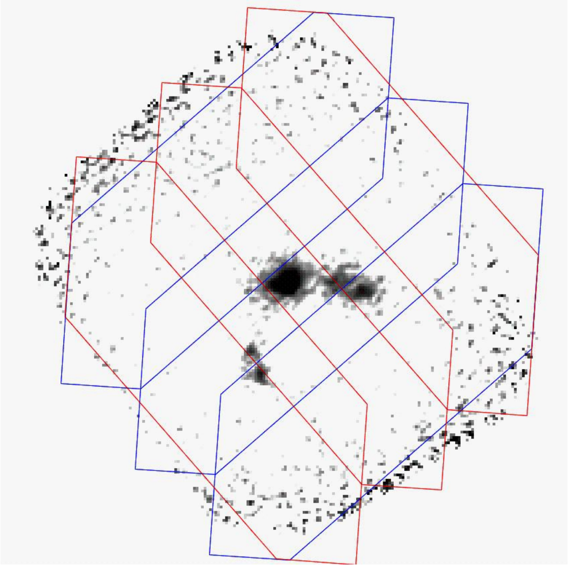

Figure 7.2: Layout of the Herschel PACS observations towards ISOSS J18364-0221. The greyscale image shows 1.2 mm continuum emission observed with MAMBO-2 at the IRAM 30m telescope ($10' \times 8'$), north is up and east is left. For the PACS $110\,\mu$m band observations, the two perpendicular scan directions are overplotted in red (3 adjacent scans northeast-southwest) and blue (3 adjacent scans northwest-southeast). Both directions are tilted with respect to the array axes that roughly point north (long axis) and west (short axis) for the chosen observational epoch.

## 7.4 Scientific aims

The main goal of these observations is to accurately determine the dust temperature and density distribution of the targeted regions and to search for more examples of massive clumps and cores in an early or even prestellar stage of evolution. The derivation of dust temperatures of individual clumps, as undertaken in the studies in Chapter 3 and 4, relied mainly on submillimetre measurements and in particular on the far-infrared observations at 70 $\mu$m with an angular resolution of about 18″. As evident from the SEDs presented there, the peak predicted between 100 and 200 $\mu$m is not sampled by the available data, and the estimated uncertainties of the dust temperatures lead to mass ranges that span a factor of two or more.

The Herschel observations will provide the important photometry covering the SED peaks of the cold clumps, and the angular resolution will match that of the single-dish submillimetre (8″ to 15″) and millimetre (at best 11″) data. Especially the bands at 75 and 110 $\mu$m yield a significant improvement in angular resolution compared to preceding observations. The combination of these data sets will allow to constrain the slope of the dust opacity in the (sub-)millimetre, and thus constrain the consistent range of dust models. This will then reduce the uncertainty of the dust temperatures by a large fraction to an estimated range of ±1 K. In the 10 to 20 K temperature regime, the corresponding masses differ by less than 30%.

Furthermore, the improved angular resolution of the measurements will be the basis for advanced modelling of the clumps and their substructure. Regarding the method of comparison to model catalogues utilised in Chapter 3, the far-infrared photometry at high spatial resolution will test the predictions of the implemented models and possibly reveal deviations from the relatively simple model structure. More sophisticated, the maps of thermal dust emission can be used to rigorously constrain the parameter space for adjusted radiative transfer calculations [Wolf *et al.*, 1999; Steinacker *et al.*, 2006]. For the best-suited targets, presumably at small distances, a comprehensive 3D modelling of the density and temperature structure is possible as demonstrated by Steinacker *et al.* [2005].

In contrast to wide-field surveys that will also be attempted with Herschel, this programme focuses on a more detailed understanding of the detailed star formation physics. Furthermore, the resulting database serves as an important reference for those surveys. They will greatly benefit from a comparison with a source sample with well-established physical properties.

## 7.5 Searching for cold clumps with Planck

The ESA Planck mission is dedicated to image the Cosmic Microwave Background (CMB) radiation over the whole sky with unprecedented angular resolution and sensitivity [Tauber, 2004], also for the CMB polarisation. The Planck instruments cover nine wavelength bands between 350 $\mu$m and 1 cm, with an angular resolution from 5′ to 33′. Once the CMB monopole and dipole terms are subtracted from the Planck all-sky maps, emission from the Milky Way remains the dominant feature. For CMB studies this mainly poses a foreground contamination. However, these maps will provide a great opportunity to localise the coldest and least evolved clumps and cores. They further extend the wavelength coverage of the IRAS and ISOSS surveys. In particular, many sources at mid- and high Galactic latitudes should be detected by Planck. The estimated sensitivity for 15 K dust aggregates at a distance of 2 kpc is on the order of $1\,\mathrm{M}_\odot$, and more than $10^4$ detections are expected. Among them possibly are also candidate massive clumps and cores. The most promising sources will then be studied in detail using Herschel [Juvela *et al.*, 2007] and other facilities.

## Chapter 8

# The prospects of observations with the JWST Mid-Infrared Instrument

## 8.1 Motivation

One result from the studies presented in previous chapters is the fact that star formation has initiated in all of the massive clumps that have been identified. Some of the embedded sources were traced only at mid-infrared wavelengths, exhibiting fluxes as low as 0.2 Jy at 24 $\mu$m and less than 50 $\mu$Jy at 8 $\mu$m in the case of ISOSS J18364-0221 SMM1 South. As noted before, the question which of these sources are precursors of high-mass stars is not answered from the available measurements. Furthermore, also several cluster-forming clumps are present, harbouring a number of presumably young stellar objects. Some of these probably represent the first observable stages in the formation of associations and clusters, and their properties reflect the initial conditions for this process. Thus, further observations of the sources promise to return important physical parameters that can be compared to the different theoretical considerations for the evolution of massive clumps and high-mass star formation.

For instance, if the clustered sources are accreting, presumably from circumstellar disks, it would be very interesting to derive the disk inclinations. These are expected to be related to the initial angular momentum of the parental cores and maybe clumps, and possibly are also sensitive to their magnetic field configuration. In the same spirit, to trace outflows and jets to their individual driving sources would provide key insights into the accretion process, i.e. possibly constrain the accretion history, and also reveal the core rotation.

A severe obstacle for such studies is the available angular resolution of mid-infrared observations and the corresponding sensitivity. The apertures of suitable spaceborne observatories (IRAS, ISO, MSX, *Spitzer*) did not exceed 0.85 m yet, limiting the angular resolution. This is less problematic for large-aperture ground-based telescopes that can observe only in the limited atmospheric bands, up to wavelengths of around 10 $\mu$m (N band) or 20 $\mu$m (Q band). However, the point source sensitivity that can be achieved with today's largest telescopes does hardly reach the mentioned flux levels. The future generation of ground-based telescopes with aperture diameters significantly greater than 10 m ("Extremely Large Telescopes") aim to improve this by factors of up to 1000, but the corresponding instruments also face severe challenges, i.e. the required background subtraction techniques and the realisation of adaptive optics in the mid-infrared.

Besides the already discussed far-infrared Herschel Space Observatory, the James Webb Space Telescope (JWST) will represent the next huge step in spaceborne infrared astronomy and overcome some of the aforementioned difficulties. This chapter introduces the mission and discusses the prospects of mid-infrared observations that will be possible with this unique facility.

In parallel to the studies presented in the previous chapters, the participation in the preparatory phase of the JWST Mid-Infrared Instrument consituted a part of the thesis project. This included the testing of the instrument verification model for its performance, also with regard to its scientific use for high-mass star formation research. The results will serve as basis for the detailed design of dedicated observing programmes in the upcoming months.

## 8.2 The James Webb Space Telescope mission

The James Webb Space Telescope [Gardner *et al.*, 2006] is a large, infrared-optimised observatory. It is a project of NASA, ESA and the Canadian Space Agency (CSA) and the destined successor of the Hubble Space Telescope (HST). The current mission schedule foresees a launch in 2013. Similar to the upcoming ESA Herschel and Planck missions, the JWST will reside in an orbit around the second Lagrange point (L2). It will have a segmented primary mirror of 6.5 m in diameter and a sunshield of about 22×12 m to allow the mirror to passively cool to below 50 K. Figure 8.1 illustrates the JWST design.

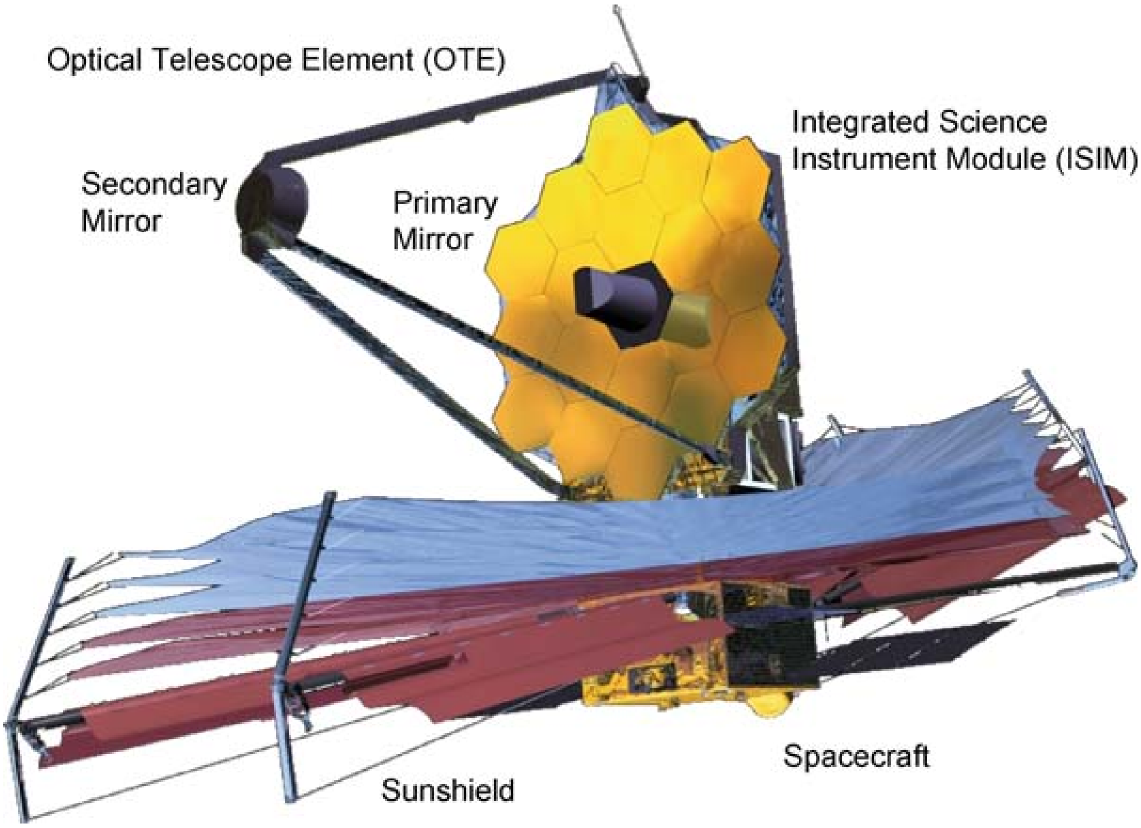

Figure 8.1: Drawing of the JWST design.

Due to the limited fairing diameter of the Ariane 5 launcher, both the mirror and sunshade will fold up and open only once the JWST is in space. A minimum mission duration of 5 yr is intended, but the spacecraft will carry propellant for at least 10 yr of operation after launch. No other consumables that would limit the lifetime are incorporated. Similar to the HST, the JWST will be operated from a Science and Operations Center located at the Space Telescope Science Institute. In brief, the main science drivers of the JWST mission can be summarised in four themes:

- *The End of the Dark Ages: First Light and Reionisation*
  The JWST shall identify the first luminous sources to form and determine the ionisation history of the early universe.
- *The Assembly of Galaxies*
  The JWST shall explore how galaxies and the dark matter, gas, stars, metals, morphological structures, and active nuclei within them evolved from the epoch of reionisation to the present day.
- *The Birth of Stars and Protoplanetary Systems*
  The JWST shall unravel the birth and early evolution of stars, from infall on to dust-enshrouded protostars to the genesis of planetary systems.
- *Planetary Systems and the Origins of Life*
  The JWST shall determine the physical and chemical properties of planetary systems including our own, and investigate the potential for the origins of life in those systems.

The JWST's instruments are designed to work primarily in the near- and mid-infrared, with some capability in the visible range. The four scientific instruments will operate under cryogenic vacuum conditions and are currently undergoing construction and testing:

- The Fine Guidance Sensor (FGS, Hutchings *et al.* [2005]) is a broadband guide camera for both guide star acquisition and fine pointing. The sensor operates over a wavelength range of 1 to 5 $\mu$m and has two HgCdTe detector arrays. The FGS Tunable Filter Imager (TFI, Doyon *et al.* [2005]) is a wide-field, narrow-band camera that provides imaging between 1.6 and 4.9 $\mu$m via tunable Fabry-Perot etalons. The camera has a single HgCdTe detector array. The FGS is provided by CSA.
- The Near-Infrared Camera (NIRCam, Rieke *et al.* [2005]) is an imager with a large field of view and high angular resolution. The NIRCam covers a wavelength range of 0.6 to 5 $\mu$m and employs ten HgCdTe detector arrays, and it is also the Optical Telescope Element wavefront sensor. The NIRCam is provided by the University of Arizona.
- The Near-Infrared Spectrograph (NIRSpec, Jakobsen *et al.* [2005]) allows multi-object, slit, and integral-field spectroscopy at low and medium spectral resolutions. The maximum wavelength range is 0.6 to 5 $\mu$m. The NIRSpec has two HgCdTe detector arrays and is supplied by ESA, with components provided by NASA.
- The Mid-Infrared Instrument (MIRI) provides imaging and spectroscopic measurements over the wavelength range 5 to 29 $\mu$m. MIRI is provided by the European Consortium with ESA and by NASA. It is described in more detail below.

The instruments are contained in the Integrated Science Instrument Module (ISIM) attached to the backplane of the primary mirror as shown in Figure 8.2.

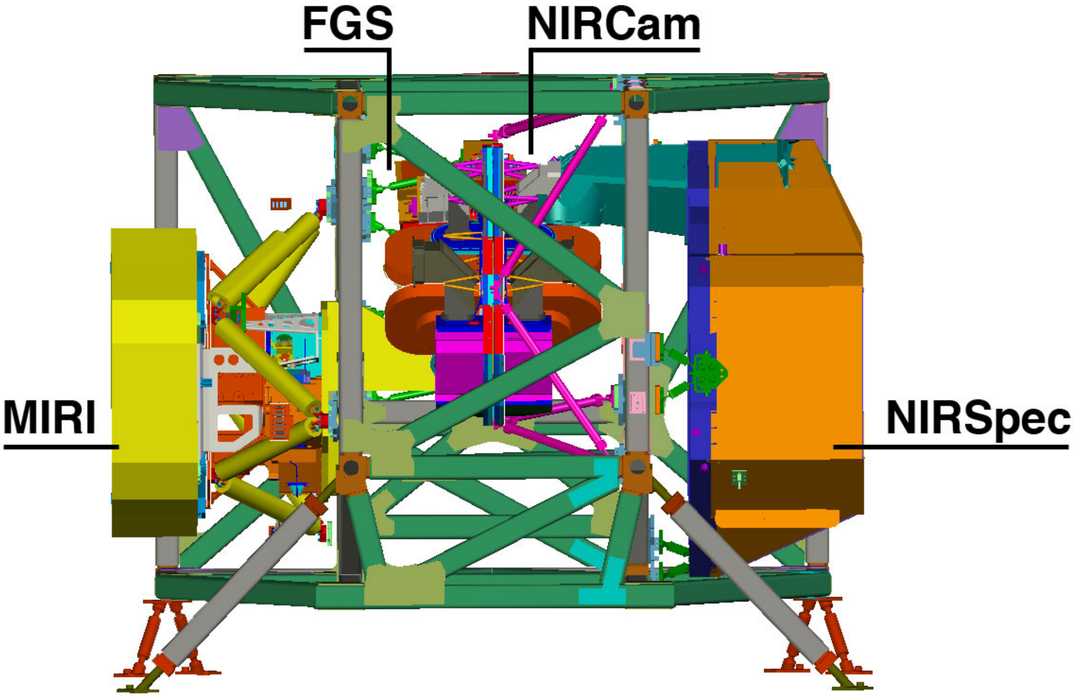

Figure 8.2: The JWST instruments' arrangement in the ISIM behind the primary mirror.

## 8.3 The Mid-Infrared Instrument MIRI

The JWST science goals indicated briefly above require a versatile mid-infrared instrument with a wide field-of-view for imaging, broad and narrow band filters, spectroscopy with a spectral resolution between 50 and 5000, and high dynamic range coronagraphy. These specifications are the basis of the MIRI design [Wright *et al.*, 2004]. The MIRI consists of the Optical Bench Assembly (OBA) with its Instrument Control Electronics (ICE), the detector modules (Focal Plane Modules, FPM) with associated Focal Plane Electronics (FPE), and a cryocooler. The MIRI OBA operating temperature lies below 10 K which will be achieved by active cooling and isolation from the warmer ISIM that is passively cooled to about 40 K. The MIRI detectors will be operated at about 7 K. The OBA contains two optical subcomponents, an imager and an integral-field spectrograph, plus an on-board calibration unit. Figure 8.3 illustrates the complete instrument. MIRI is developed by a European consortium of more than 20 scientific institutes, nationally funded, with the detectors and the active cooling system provided by NASA/JPL. All MIRI wheel mechanisms are based on a ratchet principle first flown aboard ISO [Lemke *et al.*, 1996] that provides highly repeatable positioning [Lemke *et al.*, 2006]. The wheel mechanisms have been developed under MPIA responsibility and are built in collaboration with Zeiss (Oberkochen).

### 8.3.1 Imaging, coronagraphy and low-resolution spectroscopy

The MIRI imager module provides broadband imaging, coronagraphy, and low-resolution (R≈100 at 5 to 10 $\mu$m) slit spectroscopy using a single 1024×1024 pixel Raytheon Si:As detector with 25 $\mu$m pixels. Figure 8.4 shows the focal plane arrangement of the elements of the MIRI imager.

The region on the left is the clear aperture available for imaging. The mechanical frame

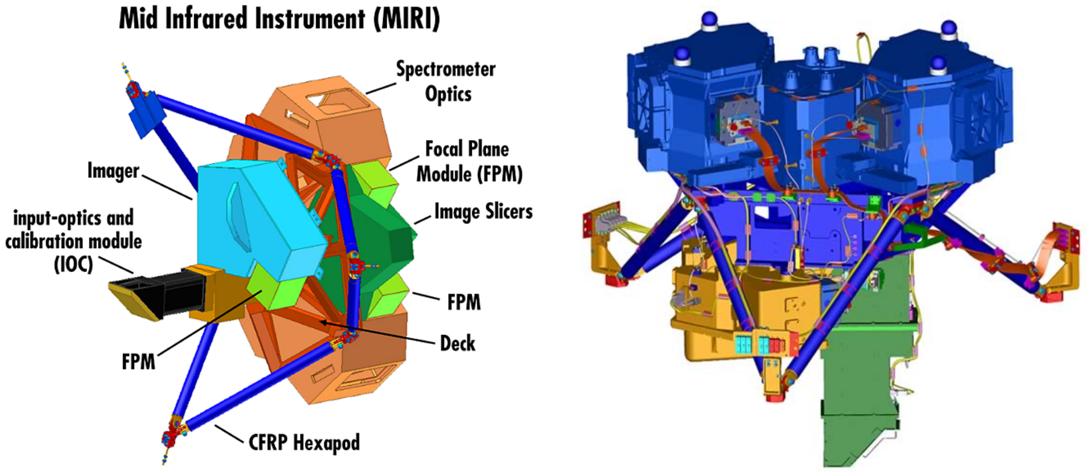

Figure 8.3: The MIRI Optical Bench Assembly and its subcomponents. MIRI is connected to the ISIM with a carbon-fibre reinforced polymer (CFRP) hexapod structure. On the right, a CAD rendering shows a rotated view with the spectrometer in blue, the imager in yellow and the IOC in green.

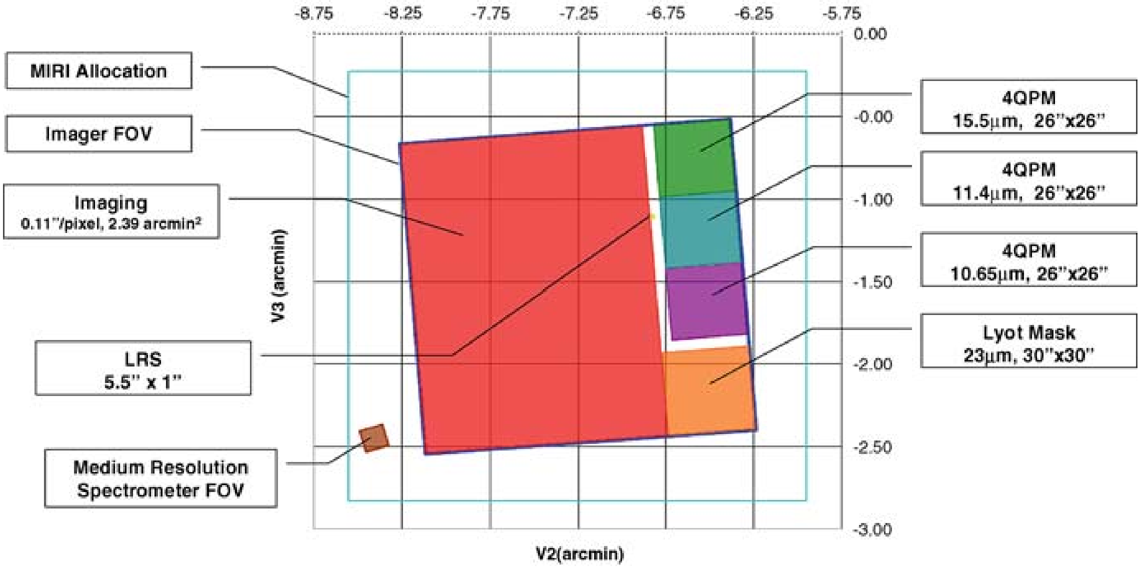

Figure 8.4: The MIRI imaging focal plane. The four coronagraphic fields utilise one quarter of the imager field-of-view and are coloured green, blue, violet and orange. The adjacent strip is devoted to the low-resolution slit spectroscopy mode, and broadband imaging will use the remaining field coloured in red.

that supports the coronagraphic masks and the slit for the low-resolution spectrometer is shown in white. The coronagraphic masks include three phase masks for quadrant-phase coronagraphy optimised for the wavelengths 10.65, 11.4 and 15.5 $\mu$m [Rouan *et al.*, 2007]. In addition, one opaque spot is present for a Lyot coronagraph at 23 $\mu$m. The imager filter wheel comprises 18 positions. 12 filters are for imaging, four filter and diaphragm combinations for coronagraphy, one ZnS-Ge double prism for the low-resolution spectroscopic mode, and one dark position. The filter specifications are listed in Table 8.1. The imager will have a pixel scale of $0.11''$ per pixel and a total field-of-view of $113'' \times 113''$.

| Filter Name | Central wavelength ($\mu$m) | Width ($\mu$m) | |
|---|---|---|---|
| F560W | 5.6 | 1.2 | Broadband |
| F770W | 7.7 | 2.2 | PAH, broadband |
| F1000W | 10 | 2 | Silicate, broadband |
| F1130W | 11.3 | 0.7 | PAH, broadband |
| F1280W | 12.8 | 2.4 | Broadband |
| F1500W | 15 | 3 | Broadband |
| F1800W | 18 | 3 | Silicate, broadband |
| F2100W | 21 | 5 | Broadband |
| F2550W | 25.5 | $\sim$4 | Broadband |
| F2550WR | 25.5 | $\sim$4 | Redundant filter to reduce risk |
| FND | Neutral density | - | Coronagraphic acquisition |
| FLENS | Lens | - | Testing |
| OPAQUE | Blackened blank | - | Darks |
| F1065C | 10.65 | 0.53 | Phase mask, $NH_3$, silicate |
| F1140C | 11.4 | 0.57 | Phase mask, continuum or PAH |
| F1550C | 15.5 | 0.78 | Phase mask, continuum |
| F2300C | 23 | 4.6 | Focal plane mask, debris disks peak |
| P750L | 7.5 | 5 | Prism, R $\approx$ 100 at 7.5 $\mu$m |

Table 8.1: The foreseen items on the 18-position MIRI imager filter wheel.

### 8.3.2 Integral-field spectroscopy

The MIRI integral-field spectrograph MRS obtains simultaneous spectral and spatial data on a small field. Accurate target positioning will be possible using offsets from the imager field-of-view to the neighbouring spectrograph field (see Figure 8.4). Dichroics divide the incoming light into four spectral ranges and each of the two 1024×1024 pixel detector arrays receives two ranges. The arrays are similar to the one employed in the imager, yet one array is optimised for long wavelengths, providing an increased quantum efficiency beyond about 13 $\mu$m. To obtain a complete spectrum, exposures at three dichroic grating wheel positions are needed. Two wheel mechanisms enable to place the gratings in the optical paths. Each of these wheel mechanisms holds a grating wheel with three pairs of gratings on the one side and a dichroic wheel on the other. They are shared between the two optical sections for the short- and long-wavelength spectral ranges. Four image slicers produce dispersed images with a spectral resolution of R $\approx$ 3000 over the 5 to 29 $\mu$m wavelength range. The integral-field spectroscopy parameters are listed in Table 8.2.

## 8.4 MIRI observations of early-stage star formation

The anticipated performance of the MIRI will allow to study the formation of stars in unprecedented detail. In particular, the early evolutionary stages of massive clumps and cores will be addressed profoundly. In the following, an example originating from this work is described. The mid-infrared imaging with high angular resolution will provide decisive

| Wavelength ($\mu$m) | Pixel size ($''$) | Slice width ($''$) | Slices | Field-of-view ($''$) | Resolution |
|---|---|---|---|---|---|
| 5.0…7.7 | 0.196 | 0.176 | 22 | 3.00×3.87 | 2400…3700 |
| 7.7…11.9 | 0.196 | 0.277 | 16 | 3.50×4.42 | 2400…3600 |
| 11.9…18.3 | 0.245 | 0.387 | 16 | 5.20×6.19 | 2400…3600 |
| 18.3…28.3 | 0.273 | 0.645 | 12 | 6.70×7.73 | 2000…2400 |

Table 8.2: Specifications of the MIRI integral-field spectrograph channels.

evidence for several previously unconstrained parameters of the very young object detected towards the star-forming core ISOSS J18364-0221 SMM1 South as discussed in Chapter 4.

### 8.4.1 A model for a young star-forming core

The *Spitzer* observations at 24 $\mu$m revealed an embedded source towards the compact ISOSS J18364-0221 SMM1 South core that is not detected at shorter wavelengths. In addition, a molecular outflow was found originating from the core, and the jet that powers the outflow was also seen in molecular hydrogen emission (see Figure 4.7). This source probably represents a protostellar object that accretes from the surrounding envelope, maybe through an accretion disk. Under this assumption, the measured fluxes from Table 4.1 were fed into the model fitting tool also used in Chapter 3. Upper flux limits for the IRAC bands were added, and the distance was fixed to 2.2 kpc. Foreground extinctions of $\mathrm{A_V} = 0$ to 300 were allowed.

The SED of this source is not fitted by an highly reddened stellar spectrum. A cut-off $\sigma_\mathrm{d} < 5$ selects 61 models. All of them belong to the earliest Stage I category and the total extinction to the central protostar is beyond $\mathrm{A_V} = 340$. Table 8.3 lists the parameters of the selected models and the best-fit model SED is plotted in Figure 8.5.

| Parameter | Range |
|---|---|
| Selected cut-off | $\chi^2_\mathrm{d} < 5$ |
| Fitted models | Stage I |
| Total extinction | $\mathrm{A_V} > 340$ |
| Preferred inclination | high |
| Central mass ($\mathrm{M_\odot}$) | $2.4 - 8.7$ |
| Envelope accretion rate ($\mathrm{M_\odot}$/yr) | $6 \cdot 10^{-5} - 3 \cdot 10^{-4}$ |

Table 8.3: Results of the SED fitting for ISOSS J18364-0221 SMM1 South.

Notably, the ranges of the central mass and accretion rate do not correspond to the expectations from the comparison of the source with the simulation of Krumholz *et al.* [2007]. This stems from the more physical and dynamical nature of the latter, whereas the SED fitting uses steady radiative transfer models. Thus, the fit results cannot be taken as firm predictions of the source properties. From the SED plot it is also obvious that the far-infrared emission as measured by the MIPS SED mode (53 to 93 $\mu$m) is not well reproduced. In this wavelength regime, the effect of the foreground extinction is rather uncertain. In addition to the model geometry, this may also contribute to the discrepancy. Also the limitation of the model calculation in the (sub-)millimetre is visible.

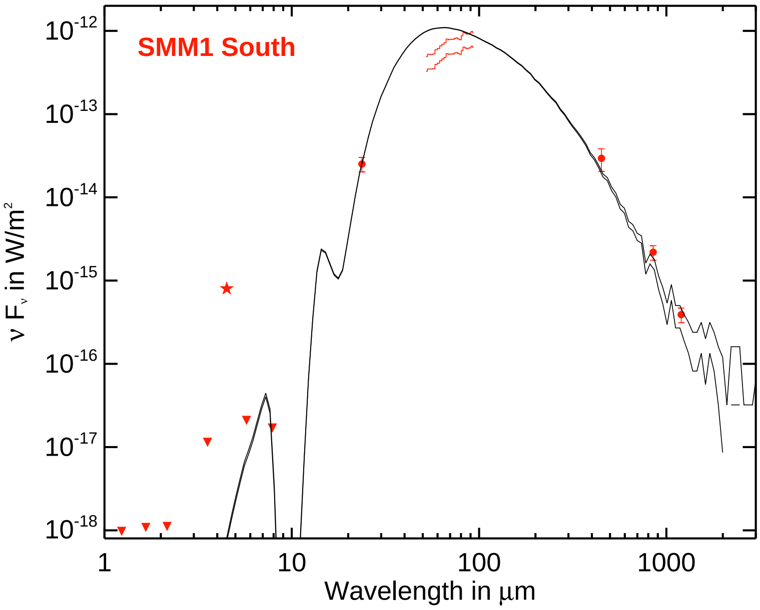

Figure 8.5: Spectral energy distributions of ISOSS J18364-0221 SMM1 South (red) and of the best-fit model. The photometric data is plotted as in Figure 4.4. The two black curves give the error range of the model SED.

### 8.4.2 The imaging capabilities of MIRI

Primarily determined by the mirror dimensions, the achievable angular resolution of the JWST is enhanced by an order of magnitude with respect to *Spitzer*. Thus, it is expected to provide the sharpness known from the HST, but in the infrared. The aim here is to use the radiative transfer calculation to visualise the imaging capabilities of MIRI. The parameters of the best-fit model do not represent the extremes among the selected models and make it a suitable example. The radiative transfer code of Whitney *et al.* [2003] was used to generate mid-infrared images of the model for the fitted inclination with respect to the line-of-sight of $i = 87.13°$. The Monte-Carlo calculation used $50 \times 10^6$ photons and the same parameters as given by the online fitter for the best-fit model. Also the fitted foreground extinction of $\mathrm{A_V} = 197.68$ was applied. Images have been created for the MIPS 24 $\mu$m filter and for the MIRI imager 25.5 $\mu$m filter (F2550W). Figure 8.6 shows the applied filter responses, both individually normalised to a peak response of unity. This MIRI imager response curve was obtained from the expected detector quantum efficiency and the measured filter transmission curve.

In Figure 8.7 the observed and modelled mid-infrared flux distribution towards the ISOSS J18364-0221 SMM1 South. The pixel scale of the model images is equivalent to the MIRI imager pixel scale of $0.11''$ per pixel. The observed image is oriented such that the outflow axis corresponds to the vertical model axis, where the model exhibits an envelope cavity. The cavity structure determines the calculated mid-infrared flux distribution as obvious in the upper right panel. To approximate the observations, this model image was convolved with the point response function for MIPS provided by the SSC with a FWHM of $5.6''$. Similarly, the model image has been convolved with a point response function scaled to $0.91''$ FWHM to generate a representation of the MIRI observations shown in the lower right.

The approximation of the MIPS observations is consistent with the actual observed

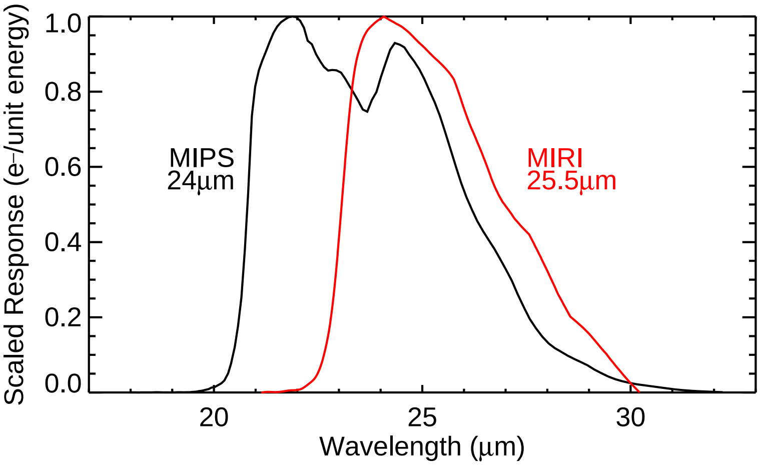

Figure 8.6: Response of the MIPS 24 $\mu$m and MIRI 25.5 $\mu$m (red) filters. Both curves are normalised to their peak response.

morphology and the observed intensity. The model's cavity structure is unresolved and a single point source pattern arises. In contrast, the higher angular resolution available with the MIRI imager allows to resolve the cavity morphology and its orientation. Thus, these observations test how well the model geometry approximates the inner structure of this star-forming core. In particular, the inclination can be constrained, a parameter that has been assumed in the derivation of the outflow properties in Chapter 4.

## 8.5 The performance of MIRI derived from Verification Model testing

### 8.5.1 The MIRI Verification Model test campaign

The MIRI development model philosophy consists of four distinct instrument models:

- The Structural Model providing early qualification of the primary structure and confidence in optical alignment testing philosophy,
- the Structural Thermal Model, an upgrade and refurbishment of the SM used for early verification of the instrument thermal performance,
- the Verification Model (VM) which checks the scientific performance and all electrical interfaces and provides additional confidence building testing of the thermal performance and allows commissioning of the test facility for the flight model,
- and the Flight Model which undergoes partial pre-flight testing and acceptance testing.

In addition, the subassemblies (Spectrometer Optics, Imager, IOC, Focal Plane System, ICE) and units (wheel and cover mechanisms) all follow separate, parallel, qualification tracks.

The MIRI VM was assembled in 2007 and two cold test campaigns were conducted between November 2007 and October 2008. This model is the first scientifically representative model, allowing a first assessment of the performance. Images of the VM are

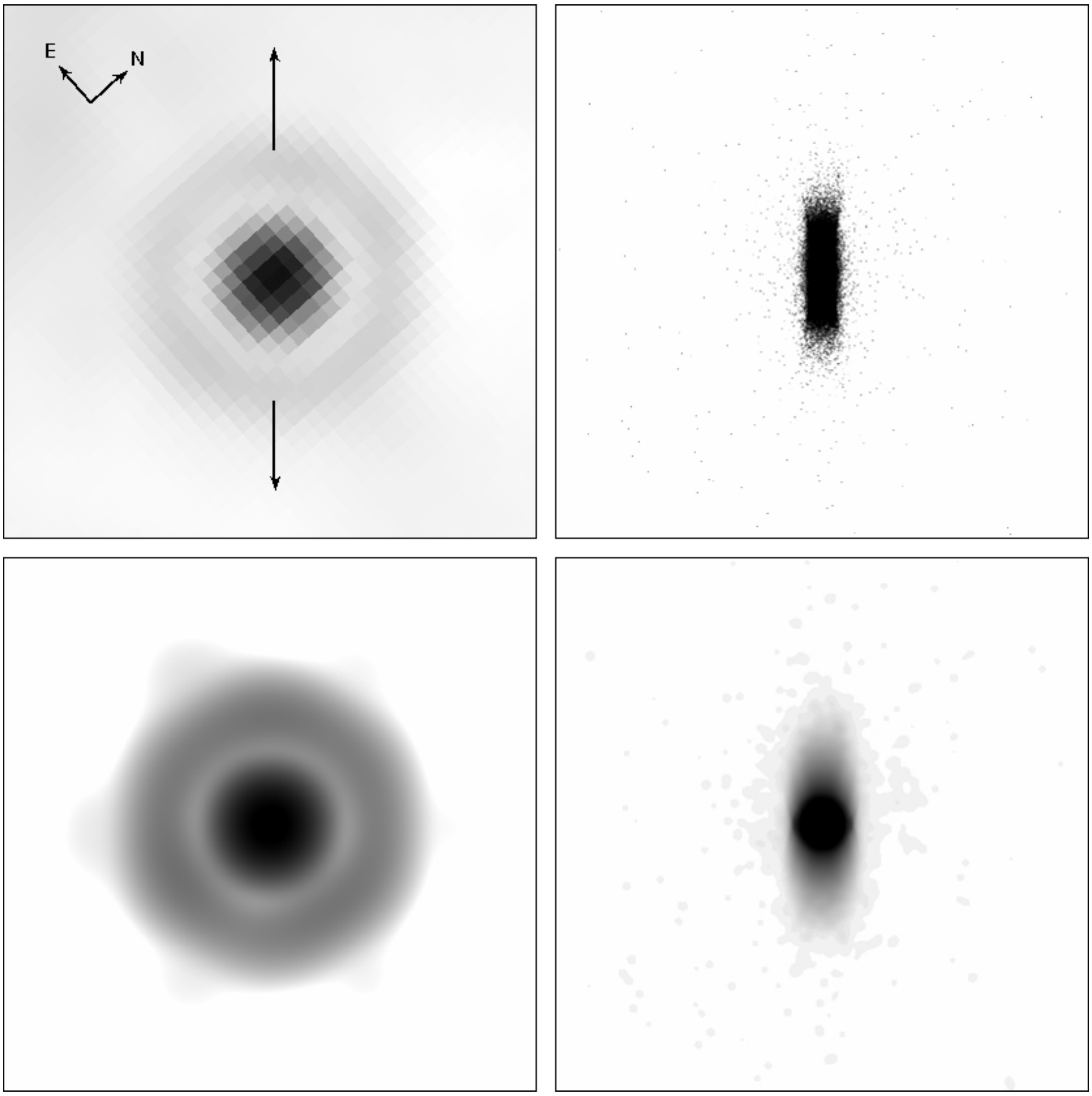

Figure 8.7: Observed and modelled images of ISOSS J18364-0221 SMM1 South. The panels span $45'' \times 45''$, corresponding to 99000 AU. Each greyscale image is logarithmically scaled over a range of 150 MJy sr$^{-1}$. Upper left: The MIPS 24 $\mu$m image, the observed outflow axis is vertically oriented and indicated by arrows. Upper right: Native image from radiative transfer calculation, the modelled envelope cavity is vertically oriented. Lower left: Radiative transfer image convolved with the MIPS point response function, approximating the observed image. Lower right: Radiative transfer image convolved with the MIRI point response function.

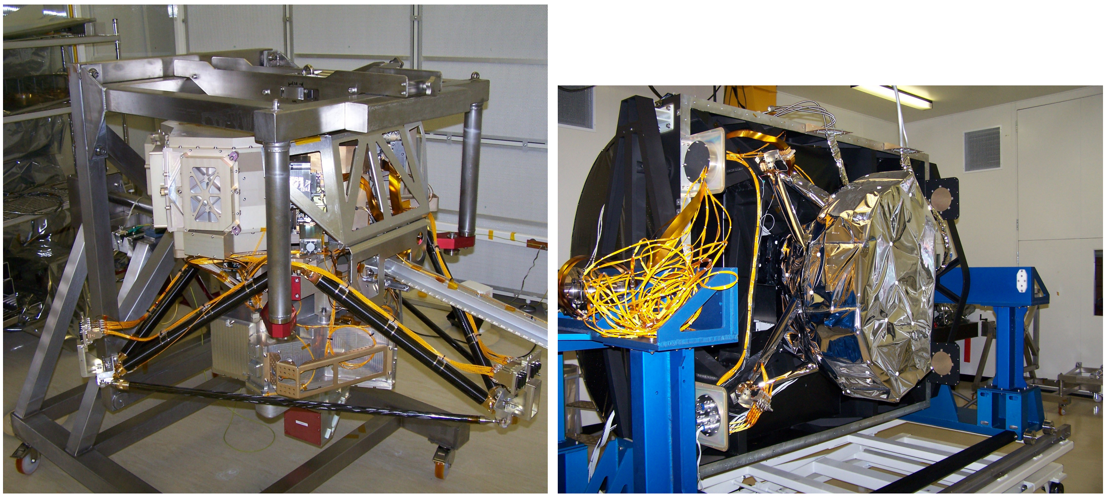

Figure 8.8: The MIRI Verification Model. Left: The fully assembled MIRI VM on its support equipment in October 2007. The spectrometer is seen above, the imager in between the black hexapod structure. Right: The MIRI VM installed on the test rig in November 2007 before it was placed in the cryogenic test chamber. The VM is fully covered with its multi-layer thermal insulation.

shown in Figure 8.8. The MIRI VM is not a fully populated model. For the imager, three of the filters (F770W, F1130W, F2550W) and two of the coronagraph masks (F2300C Lyot and F1140C quadrant phase mask) are installed but the low resolution spectrometer prism is not present. For the spectrometer, two channels that operate over the wavelength range from 4.9 to 11.8$\mu$m at a spectral resolving power in excess of 3000 are operable. Their spectral images are detected simultaneously on two halves of one of the 1024×1024 detectors. The other spectrometer detector array is present and functional but is dark. The spectrometer calibration source is present, but the imager calibration source is not.

To conduct testing of the MIRI instrument operating at temperatures as low as 6 K in a 40 K environment, a customised test rig has been developed. It houses the MIRI Telescope Simulator (MTS) which is used to provide calibration stimulus for the instrument during testing. Besides, it also provides the capability to turn the instrument through 180° when supported on the flight interface. This allows baseline imagery data to be taken during alignment testing in three different orientations.

In order to facilitate the operations of the MIRI instrument, a sophisticated set of electrical ground support equipment (EGSE) has been developed. The EGSE user interface consists of a development version of the real JWST ground system software package. This includes real time command and control capabilities, as well as providing displays and plots of housekeeping telemetry data. It also provides storage of all housekeeping and real-time log data, and has a built-in scripting language, which was used to develop all test procedures required to run the campaign. The EGSE includes a basic science data handling system, to deliver MIRI science images from the flight interface to the user. Raw science data is converted into FITS format. A real-time visualisation system provides the capability to inspect the science results at the earliest opportunity after acquisition from MIRI. This was used to aid test set-up procedures, and to check that each test had executed correctly. A Data Handling and Analysis System (DHAS) provides deeper, offline analysis of test data. The DHAS includes a data processing pipeline for first-level reduction of detector data.

The two cold MIRI VM test campaigns included repeated functional tests under ambient and cryogenic conditions, alignment and thermal balance tests, electromagnetic compatibility tests, characterisation of the MTS, and MIRI VM performance testing.

### 8.5.2 The MIRI VM performance

Most of the MIRI VM functional tests were passed flawlessly. A few problems were discovered that led to specific improvements, e.g. software updates and slight changes in the mechanism driving parameters that only mildly affected the test campaign. The MIRI thermal design was found to fulfil the requirements that the optical module is cooled down to 15.5 K, and the detectors within to below 6.7 K. During a simulated nominal operation, the optical module acquired a uniform temperature of 6.2 K, and thus all the thermal interfaces are acceptable. Also the heat load from MIRI on the cryocooler, measured under conditions very similar to those expected in flight, does not exceed the allowed range with an encouraging margin. In particular, the detector temperatures could be held within the requirements even at intentionally increased dissipation. Their temperature control provides excellent stability.

In the following sections, the main results from the MIRI VM test campaigns regarding the scientific performance are outlined. Where appropriate, also the flight model requirements are mentioned. However, these are not to be met by the VM.

#### Detector performance

The MIRI detectors used in the VM tests are engineering grade devices of varying quality. The imaging detector exhibits good sensitivity performance, but has a significant number of disconnected pixels on the lower right portion of the array (see Figure 8.9). The short wavelength spectrometer detector has good cosmetic properties and acceptable performance, it is by far the best of the three arrays. The long wavelength array is not fed by an optical path in the VM instrument, but it has a modest number of dead pixels and has one output that is not entirely stable. However, all are of adequate quality to carry out the performance testing the VM instrument was designed to address.

The MIRI detectors are read out using a sample-up-the-ramp technique. At frame zero, the pixel is reset, then subsequently integrates signal and is read non-destructively every few seconds (2.76 s for the full array). Each read-out corresponds to one frame, and all frames acquired before the next reset belong to one integration. An exposure in many cases comprises several integrations. “FASTMODE” is a read-out mode where each pixel is addressed on $10\,\mu$s intervals and sampled once within that interval. “SLOWMODE” is a read-out mode where each detector pixel is addressed for $100\,\mu$s and thus sampled 10 times, with the latter 8 samples averaged and returned as a single frame. By averaging data in this manner, the overall data rate is dramatically reduced while it still allows reduction in the effective read noise by a factor of $\sqrt{8}$. The penalty is fewer samples per ramp, so that a cosmic ray hit will contaminate a larger fraction of the total integration, and first or last frame effects have a bigger impact on the data quality. For exposures with 4 or more frames per integration, the slope of the ramp can be determined reliably.

Regarding the scientific performance, important detector properties that were investigated in the VM campaigns are the dark current, the read-out noise and the linearity of the ramps. The flight requirements on the dark current are $0.03\,\mathrm{e^-\,s^{-1}}$ and on the read-out noise $19\,\mathrm{e^-}$. Furthermore, the linearity shall be correctable to 0.25%. The measured dark current for the VM at the nominal operating temperature of 6.7 K is around $20\,\mathrm{e^-\,s^{-1}}$, and the read-out noise is about $50\,\mathrm{e^-}$. The deviations from linearity of individual pixel

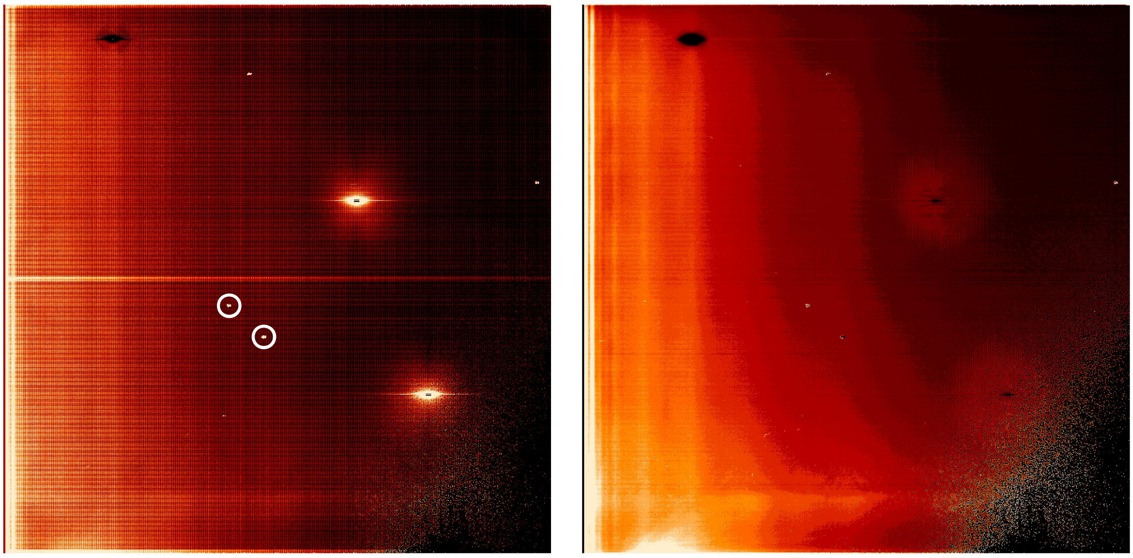

Figure 8.9: Images from the MIRI imager detector used in the VM tests. Left: Individual frame from a (nearly) dark exposure, corrected using the reference pixels of the outer four columns on the left and right. The large-scale gradient from left to right probably stems from residual illumination of the detector. Two of the several bad pixel clusters are marked with with circles. Besides, two positive and one negative "photo-emitting" defects are present (bright spots in the right half, dark spot at the upper left) that cause the surrounding pixels to glow. The lower right corner hosts many disconnected pixels. Right: Slope image derived from the same exposure. In the lower left, a glowing region appears that stems from the column shift register.

ramps are small (see Figure 8.10). A quadratic fit to the ramps reproduces the pixel values within less than 1% relative differences. The VM imager is not equipped with all stray light baffles, and thus the dark measurements are probably not representative. Besides, the testing of the engineering arrays revealed the following:

- Relaxation in the first frames: After the reset clock is turned off, the signal drops to negative values before it turns and integrates into the positive range. This goes also for the reference pixels along the left and right edges of the array and thus the effect is corrected for when they are subtracted.

- Offset in the first integration: The mean integrated signal from a bright source is found to be $0.93 \pm 0.05$ times that of the average of all subsequent integrations in one exposure. This effect is likely caused by the change in the detector clocking pattern at the start of new exposures, and it may also depend on the absolute signal level in the detector.

- Detector transients: Soon after turning on the instrument and the detectors, transients were seen that appear independent of the reset frequency. They are substantially reduced by subtracting the reference pixels, and diminish after about 30 min. During routine operations, the instrument will not be turned on or off often.

- Latent images: Infrared detectors characteristically produce latent (or persistent) images after a bright source of illumination has been removed. The exposed detector

> pixels were found to have values lower than background pixels that had little or no illumination, and this decreases with time, thus producing positive latents. The imager detector latents appear at a level of about $2.4 \pm 0.8 \times 10^{-3}$ times that of an incident non-saturating source. Latents from extremely saturated point sources decay with a half-value period of about 1 h. As MIRI shall observe very faint targets, this will probably dictate that the detectors will have to be annealed after observing very bright objects.

The first module level test results derived for the flight model detectors show that the improvements, which were partly triggered by the VM tests, are sufficient so that the flight specifications are met [Ressler *et al.*, 2008]. This goes in particular for the dark current and the read-out noise. Furthermore, due to several changes in the flight model detectors, the majority of the listed effects were eliminated or mitigated. Thus, the VM test campaign has provided important return in this respect.

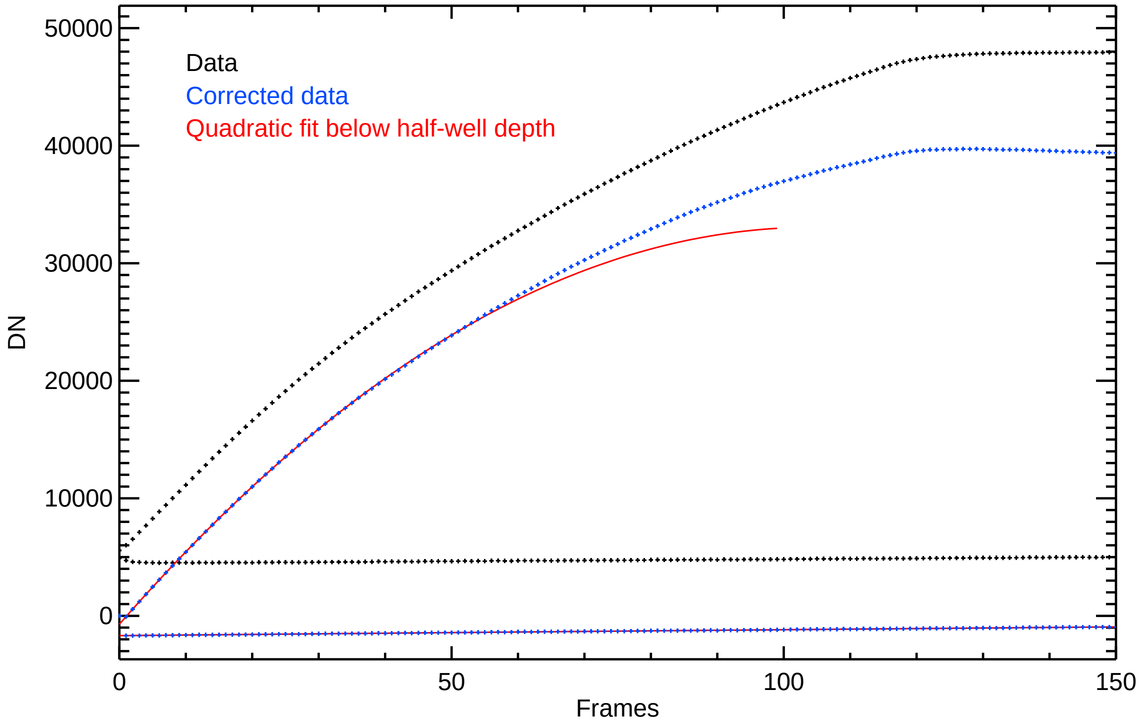

Figure 8.10: Individual ramps for one pixel of the MIRI imager detector from a dark and a saturated exposure. The saturation level (well depth) is about 47000 DN. The raw measurements are given in black, reference pixel corrected values in blue, and quadratic fits to the values below half-well depth are shown in red. In addition, the first two frames and the last frame are neglected for the fit.

Not characterised so far are the effects of ionising radiation on the detectors. On orbit, the detector arrays experience a flux of high energy particles and radiation. This can lead to increases in responsivity and noise that are not stable and introduce time-dependence in the calibration [Wolf *et al.*, 1995; Hora *et al.*, 2006]. These effects can be erased via curing procedures, usually by heating the detector, which have to be implemented.

### The imager point spread function

An important aspect of the scientific performance of the MIRI imager is the expected image quality. It is well defined by two key parameters associated with the point spread function (PSF). The FWHM is a good measure of the achievable spatial resolution, whilst the fraction of a point sources energy which is encircled within a given radius is a good measure of the sensitivity.

To project a compact point source within the MIRI field-of-view, a circular, 100 $\mu$m diameter pinhole was illuminated. The geometric size of the image was equivalent to a 1.43 pixel diameter spot at the imager detector ($0.16''$ on the sky), which compares to the 2 pixel diameter predicted for a point source observed by the JWST at 5.6 $\mu$m wavelength. In the PSF analysis, the effect of geometric broadening was not removed and is expected to mildly deteriorate the derived measures. Furthermore, pedestal features that stem from the mechanical structure around the pinhole are present that presumably lower the measured encircled energy by a small fraction.

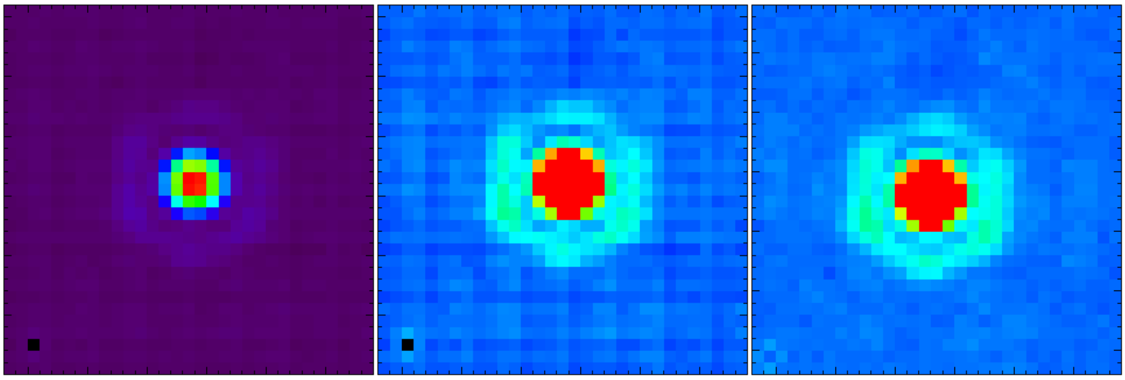

Figure 8.11: The point spread function of the MIRI VM observed through the F1130W filter. Left: Background subtracted image, scaled from -10% to 100% of the peak level. Centre: Same image, scaled from -10% to 20%. Right: Same image and scale as in centre. Correlated noise has been removed and bad pixels were cleaned. Adopted from Lim *et al.* [2008].

| Filter Name | Expected FWHM[a] ($''$) | Measured FWHM ($''$) | Modelled radius of first dark ring[b] ($''$) | Fraction of encircled energy within first dark ring [c] |
|---|---|---|---|---|
| F770W | 0.30 | 0.30 | 0.30 | 0.53 |
| F1130W | 0.44 | 0.42 | 0.44 | 0.54 |
| F2300C | 0.90 | 0.82 | 0.89 | 0.42 |
| F2550W | 1.0 | 0.91 | 0.99 | 0.63 |

[a] Scaled from a nominal FWHM of 2 pixels at 5.6 $\mu$m.
[b] Derived from a segmented telescope model.
[c] Normalised to a $5''$ radius aperture.

Table 8.4: Parameters of the MIRI VM point spread function.

Figure 8.11 shows the image of the pinhole taken through the F1130W filter, and

Table 8.4 lists the measurements for four VM filters. Notably, the measured FWHM values are consistent with the expected values scaled from a nominal PSF at 5.6 $\mu$m. According to the flight model requirement on image quality, the encircled energy within the first dark ring, determined from a JWST segmented telescope model, shall exceed 56%. Except for the coronagraphy filter, the measured fractions are close to or better than this. In summary, the image quality of the MIRI VM is already close to the flight model expectations and requirements.

For the integrated observatory, in particular the segmented primary mirror of the JWST introduces a complex subtructure to the resulting PSF. Alignment errors and almost every motion of any component in the system will induce some level of wavefront error. To provide compensation, an active control system is designed that also uses rigid body motions of the 18 primary mirror segments and the secondary mirror. For illustration, Figure 8.12 shows a simulated PSF at 11.4 $\mu$m.

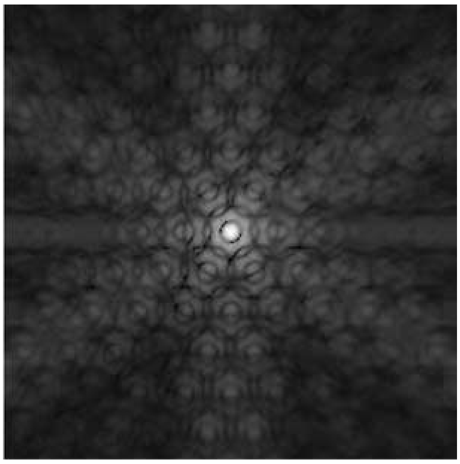

Figure 8.12: Simulated JWST point spread function at 11.4 $\mu$m. The segmented primary mirror geometry and phase aberrations were taken into account. Adopted from Boccaletti *et al.* [2005].

### Spectrometer performance

Several test observations with the short-wavelength MIRI integral field spectrometer are shown in Figure 8.13. A flatfield illumination was provided by the internal calibration source. In the first panel, the flatfield image reveals the positions and the curvature of the individual slices. They are in excellent agreement with the optical model, and the uniformity of the illumination shows that the calibration system works as intended. The overall fall in signal level with increasing wavelength is due to the calibration sources 800 K grey body emission spectrum. The absolute signal level is consistent with the nominal spectrometer throughput. The spectral fringes seen on both slice groups have been predicted as an unavoidable feature of the MIRI detector technology. They stem from constructive and destructive interferences on plane-parallel surfaces in the optical path, i.e. the detector substrates. Three of the slice spectra in Channel 2 appear slightly less bright than the others. In these cases, the internal slice specific pupil mask was intentionally undersized as part of an investigation into the delivered spectral resolution. In combination with the optical model, the flatfield observations allowed to derive the mapping functions from pixels to slices and to wavelength regions. From these, spectral

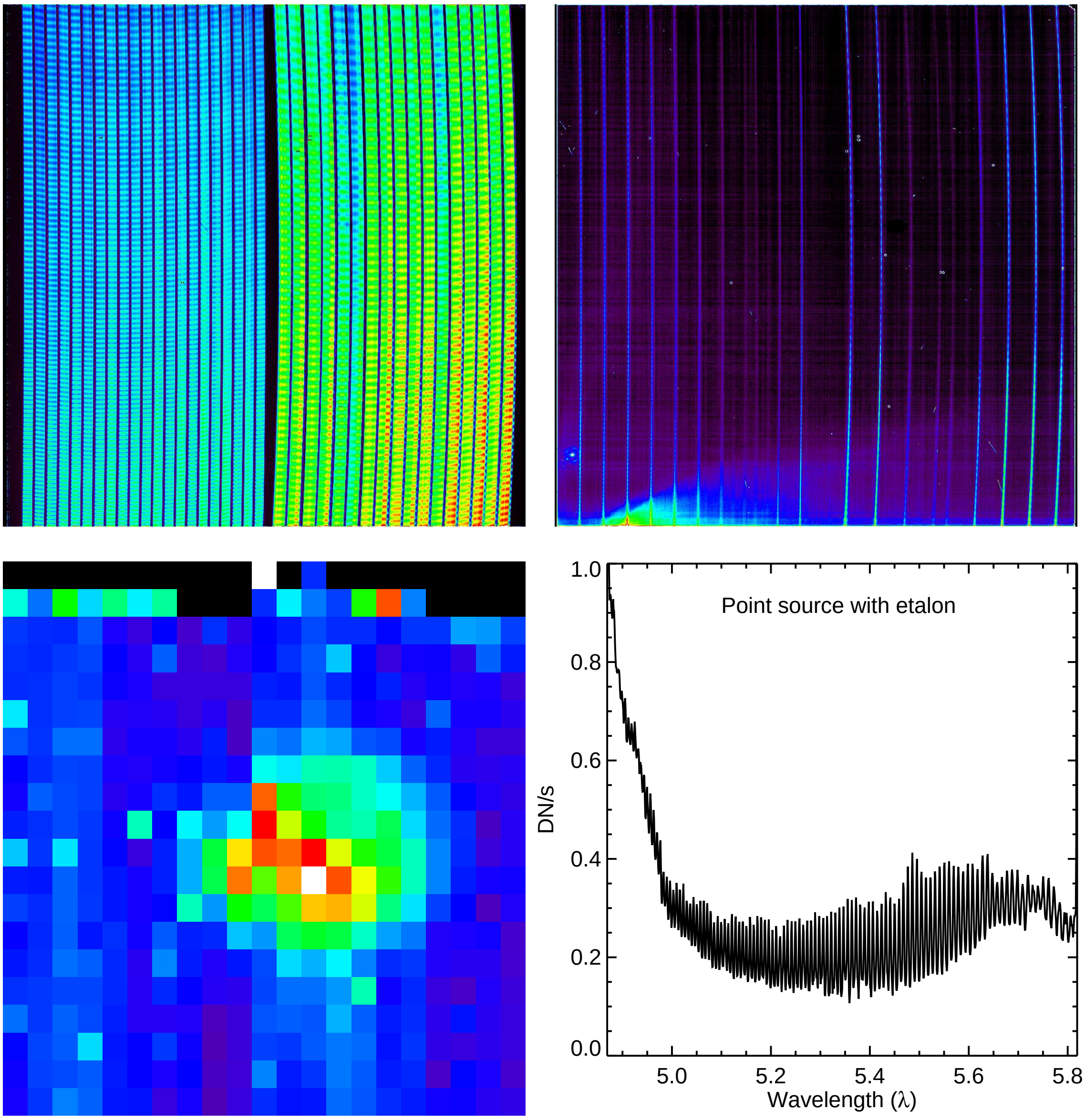

Figure 8.13: Test observations with the MIRI integral field spectrometer. Upper left: Slope image of a flatfield exposure. The left part of the detector array receives the slices of Channel 1B (5.7 to 6.7 $\mu$m), the right part those of Channel 2A (8.6 to 10.2 $\mu$m). Wavelength increases from the bottom to the top of the images. Upper right: Slope image of a faint point source within the spectrometer field-of-view. Lower left: View of a data cube of Channel 1 integrated over the spectral dimension. A defocused continuum point source was imaged in the right half of the field-of-view. The pixel scale is $0.176'' \times 0.196''$. Lower right: Spectrum of a pooint source extracted from one pixel of the data cube. A point source with an etalon was imaged. The etalon lines are resolved in the derived spectrum.

datacubes can be built. The lower left panel of Figure 8.13 shows the spatial dimensions of an integrated cube. No flatfield corrections and bad pixel masks were applied. During the VM testing, it was not possible to properly focus the external point source within the spectrometer field-of-view, and thus the obtained image shows a rather broad footprint of the source. The MTS is corrected for the flight model tests to provide a focused source. The extracted spectrum of a point source with an etalon that allows wavelength calibration shows that the individual lines are properly resolved. The wavelength calibration and fringe correction are currently under development, and also the analysis of the image quality and stability is ongoing. Nevertheless, the derived results so far indicate that also the MIRI VM spectrometer performance meets the expectations.

## 8.6 Summary and outlook on further analysis

The JWST with MIRI will provide a unique mid-infrared observatory that allows to disentangle the high-mass star formation process to unprecedented detail. The sensitivity and imaging performance of MIRI is required for follow-up studies of the youngest objects discovered by *Spitzer*. A case in point is the compact ISOSS J18364-0221 SMM1 South protostellar core that may represent a forming high-mass star in an early stage that so far sparsely explored. For this source, the simulations of the imaging with the spatial resolution that is expected for MIRI show that the inner structure of the core can be revealed and related important parameters like the presence and orientation of cavities can be inferred. In addition, the integral-field spectroscopy provided by MIRI will allow to characterise the local gas distribution and temperatures. The encouraging first tests of the MIRI VM undertaken within the last year indicate that MIRI will deliver outstanding observations. The MIRI VM image quality almost meets the flight model requirements, and also the spectrometer performs well. Besides, the flight model detectors provide the necessary low dark current and read-out noise.

At present, several important aspects of the instrument remain to be evaluated. On detector level, the appropriate linearity and flatfield corrections will be implemented. For the imager, the ongoing analysis of the test data will assess the spectrophotometric performance after a relative calibration of the utilised stimulating sources has been established. Furthermore, from the comprehensive set of measurements with the VM the photometric stability over the testing period and possible out-of-band sensitivities will be checked. Already mentioned above, the wavelength calibration for the spectrometer will be the basis for more detailed analysis.

# Chapter 9

# Summary and Outlook

## 9.1 Summary

This work addresses the early stages of high-mass star formation observationally. High-mass stars are almost always found in associations and clusters. These systems are presumably formed from massive clumps that comprise compact cores of high density. The initially prestellar cores are expected to first generate low-mass protostellar seeds that accrete at high rates and gain mass. The lack of clear examples for these very early stages motivate the search for massive and cold clumps.

From the ISO Serendipity Survey, a sample of massive star-forming regions that contain a large fraction of cold dusty material has been identified. Follow-up observations at multiple wavelengths are evaluated and the star-forming content of a number of regions is characterised. Altogether, 13 identified clumps found in six ISOSS regions are studied using photometric data from the near-infrared to the millimetre regime. Derived from the spectral energy distributions, the dust temperatures vary between 12 and 22 K, and in most cases these cold components dominate the clump masses which range from about 2 to $170\,\mathrm{M}_\odot$. Thus, the far-infrared selection method successfully identified candidate birthplaces of high-mass stars and the accompanying associations or clusters. Nevertheless, star formation has initiated in all the studied clumps. The majority of clumps harbour mid-infrared sources, interpreted as embedded young stellar objects. Several of them are assigned to the intermediate-mass range, and most are low-mass objects. The ISOSS J18364-0221 SMM1 clump is investigated using millimetre interferometry and harbours the youngest objects identified: two compact cores of about $15\,\mathrm{M}_\odot$ that drive outflows, and only one of them is detected in the mid-infrared. In particular the latter objects may represent examples for the early protostellar stages of high-mass star formation. However, massive prestellar cores remain elusive and probably persist on short timescales only. Several massive clumps have served as targets for mid-infrared spectroscopy. They are found to harbour molecular hydrogen gas at temperatures of several 100 K, with the clump mentioned above exhibiting the lowest values. Towards clumps that are associated with multiple sources, also prominent features that stem from PAHs are present which probably trace interstellar ultra-violet radiation.

More facets of the investigated sources will be revealed by the upcoming observations with ESA's Herschel far-infrared space observatory. A dedicated key programme addresses the first stages in the formation of high-mass stars including the presented ISOSS regions. The observations at unexampled high angular resolution will establish narrow constraints on the dust temperature and density distributions and further allow very detailed radiative transfer modelling.

To reveal the inner structure of the clumps and cores that harbour candidate high-mass star precursors requires observations as can be obtained with the mid-infrared instrument MIRI aboard the James Webb Space Telescope. The angular resolution with respect to the available data will be improved by roughly an order of magnitude. Derived from a radiative transfer simulation of a core, this will allow to resolve presumed cavities and characterise the core envelope geometry.

The first assessment of the scientific performance of MIRI has been made by testing the Verification Model. Although it does not thoroughly mimic the flight model in many respects, the measured imaging quality and spectrometer performance almost meet the flight requirements. This suggests that MIRI will deliver the expected scientific return, and, according to experience, discover new phenomena.

## 9.2 Future work

The results presented in this work motivate further analysis and studies besides the mentioned space telescope observations. The main objectives and means of upcoming studies focused on the ISOSS regions are the following:

- More examples of the identified massive clumps will be studied in detail to uncover their possible fragmentation and substructures. This will be possible using millimetre continuum interferometry.
- The kinematic structure of compact high-mass star-forming cores, initially addressed in this work, is an important prediction of concurrent simulations. Observations of additional molecular emission at interferometric resolution will allow to implement more physical radiative transfer models, and thus to better constrain the velocity distribution.
- To clarify the relation of jets and molecular outflows e.g. in the case of ISOSS J18364-0221 SMM1, the jet velocities will be constrained using ground-based near-infrared spectroscopy at high spectral resolution.
- The collected mid-infrared spectra towards presumably singular sources will be combined with the available photometric data to produce a comprehensive model. This will be based on radiative transfer models for the continuum, but also on the detailed analysis of the profiles of silicate emission features, PAH features, molecular hydrogen lines and fine-structure lines.
- Using recently available dust models that include PAHs, the interstellar material and radiation field present in the observed cluster-forming clumps will be investigated.

The search for massive prestellar cores remains a crucial task to explore the initial conditions of high-mass star formation. Already mentioned, the Planck survey will provide the possibility to find new candidate sources. The all-sky survey carried out by the Japanese infrared satellite AKARI provides photometric data at wavelengths beyond 100 $\mu$m [Murakami *et al.*, 2007]. The cryogenic mission phase ended in August 2007 when the liquid helium supply was depleted, and the achieved sky coverage reached about 94%. The processing of the collected data in the four photometric bands at 65, 90, 140, and 160 $\mu$m is ongoing. Point source catalogues shall be released in September 2009, and these will provide a basis for the selection of star-forming regions similar to the method applied with the ISOSS.

## Parts of this thesis appear in the following publications:

### Refereed journals:

*An infrared-submillimeter study of starforming regions*
*selected by the ISOSS 170 μm survey*
Martin Hennemann, Stephan M. Birkmann, Oliver Krause & Dietrich Lemke
A&A, Volume 485, Issue 3, 2008, pp. 753-763

*Star-Forming Cores Embedded in a Massive Cold Clump:*
*Fragmentation, Collapse and Energetic Outflows*
Martin Hennemann, Stephan M. Birkmann, Oliver Krause, Dietrich Lemke,
Yaroslav Pavlyuchenkov, Surhud More, & Thomas Henning
Submitted to ApJ, 2008

### Conference proceedings:

*A (Sub)Millimeter survey of massive star-forming regions*
*identified by the ISOPHOT Serendipity Survey (ISOSS)*
Martin Hennemann, Stephan M. Birkmann, Oliver Krause, & Dietrich Lemke
Triggered Star Formation in a Turbulent ISM, edited by B. G. Elmegreen & J. Palous.
Proceedings of the International Astronomical Union, IAU Symposium 237.
Cambridge University Press, 2007, pp. 424-424

*First results from MIRI verification model testing*
Tanya Lim, Jose L. Alvarez, Eva Bauwens, Alejandro Garcia Bedregal, Joris Blommaert, Helmut Dannerbauer, Paul Eccleston, Marc Ferlet, Sebastian Fischer, Macarena Garcia-Marin, Alistair Glasse, Adrian Michael Glauser, Karl Gordon, Tom Greene, Tim Grundy, Martin Hennemann, Ulrich Klaas, Alvaro Labiano, Fred Lahuis, Juan Rafael Martínez-Galarza, Bruno Merin Martin, Jane Morrison, Theodoros Nakos, Brian O'Sullivan, Bart Pindor, Michael Ressler, Bryan Shaughnessy, Bart Vandenbussche, Martyn Wells, Gillian Wright & Jens Zuther
Space Telescopes and Instrumentation 2008: Optical, Infrared, and Millimeter, edited by J. M. Oschmann, Jr., M. W. M. de Graauw & H. A. MacEwen.
Proceedings of SPIE Volume 7010

# Bibliography

P. André, S. Basu, and S.-i. Inutsuka. The Formation and Evolution of Prestellar Cores. *ArXiv e-prints*, January 2008.

P. André. Observations of protostars and protostellar stages. In T. Montmerle, C. J. Lada, I. F. Mirabel, and J. Tran Thanh Van, editors, *The Cold Universe*, pages 179–+, 1994.

H. G. Arce and A. I. Sargent. The Evolution of Outflow-Envelope Interactions in Low-Mass Protostars. *ApJ*, 646:1070–1085, August 2006.

J. Bally. Outflows from Massive Stars. In H. Beuther, H. Linz, and Th. Henning, editors, *Massive Star Formation: Observations Confront Theory*, volume 387 of *Astronomical Society of the Pacific Conference Series*, pages 158–+, May 2008.

H. Baumeister, P. Bizenberger, C. A. L. Bayler-Jones, Z. Kovács, H.-J. Röser, and R.-R. Rohloff. Cryogenic engineering for OMEGA2000: design and performance. In M. Iye and A. F. M. Moorwood, editors, *Instrument Design and Performance for Optical/Infrared Ground-based Telescopes*, volume 4841 of *Proceedings of SPIE*, pages 343–354, March 2003.

C. A. Beichman, G. Neugebauer, H. J. Habing, P. E. Clegg, and T. J. Chester, editors. *Infrared astronomical satellite (IRAS) catalogs and atlases. Volume 1: Explanatory supplement*, volume 1, 1988.

H. Beuther and D. Shepherd. Precursors of UCHII Regions and the Evolution of Massive Outflows. In M. S. N. Kumar, M. Tafalla, and P. Caselli, editors, *Cores to Clusters: Star Formation with Next Generation Telescopes*, pages 105–119, November 2005.

H. Beuther and J. Steinacker. The Protostar in the Massive Infrared Dark Cloud IRDC 18223-3. *ApJL*, 656:L85–L88, February 2007.

H. Beuther, P. Schilke, F. Gueth, M. McCaughrean, M. Andersen, T. K. Sridharan, and K. M. Menten. IRAS 05358+3543: Multiple outflows at the earliest stages of massive star formation. *A&A*, 387:931–943, June 2002.

H. Beuther, P. Schilke, K. M. Menten, F. Motte, T. K. Sridharan, and F. Wyrowski. High-Mass Protostellar Candidates. II. Density Structure from Dust Continuum and CS Emission. *ApJ*, 566:945–965, February 2002.

H. Beuther, P. Schilke, T. K. Sridharan, K. M. Menten, C. M. Walmsley, and F. Wyrowski. Massive molecular outflows. *A&A*, 383:892–904, March 2002.

H. Beuther, E. B. Churchwell, C. F. McKee, and J. C. Tan. The Formation of Massive Stars. In B. Reipurth, D. Jewitt, and K. Keil, editors, *Protostars and Planets V*, pages 165–180, 2007.

H. Beuther, H. Linz, and Th. Henning, editors. *Massive Star Formation: Observations Confront Theory*, volume 387 of *Astronomical Society of the Pacific Conference Series*, May 2008.

S. M. Birkmann, O. Krause, and D. Lemke. Very Cold and Massive Cores near ISOSS J18364-0221: Implications for the Initial Conditions of High-Mass Star Formation. *ApJ*, 637:380–383, January 2006.

S. M. Birkmann, O. Krause, M. Hennemann, Th. Henning, J. Steinacker, and D. Lemke. A massive protostellar core with an infalling envelope. *A&A*, 474:883–890, November 2007.

S. M. Birkmann. The early phases of massive star birth. *Ph.D. Thesis, Combined Faculties for the Natural Sciences and for Mathematics of the Ruperto-Carola University of Heidelberg, Germany*, February 2007.

P. Bizenberger, M. J. McCaughrean, C. Birk, D. Thompson, and C. Storz. Omega Prime: the wide-field near-infrared camera for the 3.5-m telescope of the Calar Alto Observatory. In A. M. Fowler, editor, *Infrared Astronomical Instrumentation*, volume 3354 of *Proceedings of SPIE*, pages 825–832, August 1998.

J. H. Black and E. F. van Dishoeck. Fluorescent excitation of interstellar H2. *ApJ*, 322:412–449, November 1987.

A. Boccaletti, P. Baudoz, J. Baudrand, J. M. Reess, and D. Rouan. Imaging exoplanets with the coronagraph of JWST/MIRI. *Advances in Space Research*, 36:1099–1106, 2005.

N. W. Boggess, J. C. Mather, R. Weiss, C. L. Bennett, E. S. Cheng, E. Dwek, S. Gulkis, M. G. Hauser, M. A. Janssen, T. Kelsall, S. S. Meyer, S. H. Moseley, T. L. Murdock, R. A. Shafer, R. F. Silverberg, G. F. Smoot, D. T. Wilkinson, and E. L. Wright. The COBE mission - Its design and performance two years after launch. *ApJ*, 397:420–429, October 1992.

S. Bogun, D. Lemke, U. Klaas, U. Herbstmeier, R. Assendorp, G. Richter, R. Laureijs, M. F. Kessler, M. Burgdorf, B. Schulz, G. Pelz, C. A. Beichman, and M. Rowan-Robinson. First data from the ISOPHOT FIR Serendipity survey. *A&A*, 315:L71–L74, November 1996.

I. A. Bonnell and M. R. Bate. Binary systems and stellar mergers in massive star formation. *MNRAS*, 362:915–920, September 2005.

I. A. Bonnell and M. R. Bate. Star formation through gravitational collapse and competitive accretion. *MNRAS*, 370:488–494, July 2006.

I. A. Bonnell, M. R. Bate, and H. Zinnecker. On the formation of massive stars. *MNRAS*, 298:93–102, July 1998.

I. A. Bonnell, M. R. Bate, C. J. Clarke, and J. E. Pringle. Competitive accretion in embedded stellar clusters. *MNRAS*, 323:785–794, May 2001.

I. A. Bonnell, C. J. Clarke, and M. R. Bate. The Jeans mass and the origin of the knee in the IMF. *MNRAS*, 368:1296–1300, May 2006.

J. Brand and L. Blitz. The Velocity Field of the Outer Galaxy. *A&A*, 275:67–+, August 1993.

S. Cabrit and C. Bertout. CO line formation in bipolar flows. II - Decelerated outflow case and summary of results. *ApJ*, 348:530–541, January 1990.

G. Chabrier. Galactic Stellar and Substellar Initial Mass Function. *PASP*, 115:763–795, July 2003.

M. Choi, N. J. Evans, II, and D. T. Jaffe. Extremely High Velocity Outflows. *ApJ*, 417:624–+, November 1993.

E. Churchwell. Ultra-Compact HII Regions and Massive Star Formation. *ARAA*, 40:27–62, 2002.

P. C. Clark, I. A. Bonnell, and R. S. Klessen. The star formation efficiency and its relation to variations in the initial mass function. *MNRAS*, 386:3–10, May 2008.

J. M. De Buizer, A. M. Watson, J. T. Radomski, R. K. Piña, and C. M. Telesco. Mid-Infrared Detection of a Hot Molecular Core in G29.96-0.02. *ApJL*, 564:L101–L104, January 2002.

T. de Graauw, E. Caux, R. Guesten, F. Helmich, J. Pearson, T. G. Phillips, R. Schieder, X. Tielens, P. Saraceno, J. Stutzki, C. K. Wafelbakker, and N. D. Whyborn. The Herschel-Heterodyne Instrument for the Far-Infrared (HIFI). In *Bulletin of the American Astronomical Society*, volume 37, pages 1219–+, December 2005.

J. Di Francesco, N. J. Evans, II, P. Caselli, P. C. Myers, Y. Shirley, Y. Aikawa, and M. Tafalla. An Observational Perspective of Low-Mass Dense Cores I: Internal Physical and Chemical Properties. In B. Reipurth, D. Jewitt, and K. Keil, editors, *Protostars and Planets V*, pages 17–32, 2007.

C. L. Dobbs, I. A. Bonnell, and P. C. Clark. Centrally condensed turbulent cores: massive stars or fragmentation? *MNRAS*, 360:2–8, June 2005.

R. Doyon, R. Hutchings, N. Rowlands, C. Evans, E. Greenberg, A. Scott, R. Abraham, L. Ferrarese, A. Fullerton, R. Jayawardhana, D. Johnstone, M. R. Meyer, J. Pipher, and M. Sawicki. TFI: The JWST Tunable Filter Imager. In *Bulletin of the American Astronomical Society*, volume 37, pages 1352–+, December 2005.

B. T. Draine and H. M. Lee. Optical properties of interstellar graphite and silicate grains. *ApJ*, 285:89–108, October 1984.

B. T. Draine and A. Li. Infrared Emission from Interstellar Dust. IV. The Silicate-Graphite-PAH Model in the Post-Spitzer Era. *ApJ*, 657:810–837, March 2007.

M. P. Egan, R. F. Shipman, S. D. Price, S. J. Carey, F. O. Clark, and M. Cohen. A Population of Cold Cores in the Galactic Plane. *ApJL*, 494:L199+, February 1998.

J. H. Elias. H2 emission from Herbig-Haro objects. *ApJ*, 241:728–735, October 1980.

B. G. Elmegreen. On the Rapid Collapse and Evolution of Molecular Clouds. *ApJ*, 668:1064–1082, October 2007.

C. W. Engelbracht, M. Blaylock, K. Y. L. Su, J. Rho, G. H. Rieke, J. Muzerolle, D. L. Padgett, D. C. Hines, K. D. Gordon, D. Fadda, A. Noriega-Crespo, D. M. Kelly, W. B. Latter, J. L. Hinz, K. A. Misselt, J. E. Morrison, J. A. Stansberry, D. L. Shupe, S. Stolovy, W. A. Wheaton, E. T. Young, G. Neugebauer, S. Wachter, P. G. Pérez-González, D. T.

Frayer, and F. R. Marleau. Absolute Calibration and Characterization of the Multiband Imaging Photometer for Spitzer. I. The Stellar Calibrator Sample and the 24 $\mu$m Calibration. *PASP*, 119:994–1018, September 2007.

M. L. Enoch, J. Glenn, N. J. Evans, II, A. I. Sargent, K. E. Young, and T. L. Huard. Comparing Star Formation on Large Scales in the c2d Legacy Clouds: Bolocam 1.1 mm Dust Continuum Surveys of Serpens, Perseus, and Ophiuchus. *ApJ*, 666:982–1001, September 2007.

N. Evans. Panel Discussion I: What is a Massive Protostar? Theoretical Definitions, Observational Criteria, and Evolutionary Sequence. In H. Beuther, H. Linz, and Th. Henning, editors, *Massive Star Formation: Observations Confront Theory*, volume 387 of *Astronomical Society of the Pacific Conference Series*, pages 425–+, May 2008.

G. G. Fazio, J. L. Hora, L. E. Allen, M. L. N. Ashby, P. Barmby, L. K. Deutsch, J.-S. Huang, S. Kleiner, M. Marengo, S. T. Megeath, G. J. Melnick, M. A. Pahre, B. M. Patten, J. Polizotti, H. A. Smith, R. S. Taylor, Z. Wang, S. P. Willner, W. F. Hoffmann, J. L. Pipher, W. J. Forrest, C. W. McMurty, C. R. McCreight, M. E. McKelvey, R. E. McMurray, D. G. Koch, S. H. Moseley, R. G. Arendt, J. E. Mentzell, C. T. Marx, P. Losch, P. Mayman, W. Eichhorn, D. Krebs, M. Jhabvala, D. Y. Gezari, D. J. Fixsen, J. Flores, K. Shakoorzadeh, R. Jungo, C. Hakun, L. Workman, G. Karpati, R. Kichak, R. Whitley, S. Mann, E. V. Tollestrup, P. Eisenhardt, D. Stern, V. Gorjian, B. Bhattacharya, S. Carey, B. O. Nelson, W. J. Glaccum, M. Lacy, P. J. Lowrance, S. Laine, W. T. Reach, J. A. Stauffer, J. A. Surace, G. Wilson, E. L. Wright, A. Hoffman, G. Domingo, and M. Cohen. The Infrared Array Camera (IRAC) for the Spitzer Space Telescope. *ApJS*, 154:10–17, September 2004.

J. Forbrich, T. Stanke, R. Klein, Th. Henning, K. M. Menten, K. Schreyer, and B. Posselt. A multi-wavelength study of a double intermediate-mass protostar - from large-scale structure to collimated jets. *ArXiv e-prints*, September 2008.

J. P. Gardner, J. C. Mather, M. Clampin, R. Doyon, M. A. Greenhouse, H. B. Hammel, J. B. Hutchings, P. Jakobsen, S. J. Lilly, K. S. Long, J. I. Lunine, M. J. McCaughrean, M. Mountain, J. Nella, G. H. Rieke, M. J. Rieke, H.-W. Rix, E. P. Smith, G. Sonneborn, M. Stiavelli, H. S. Stockman, R. A. Windhorst, and G. S. Wright. The James Webb Space Telescope. *Space Science Reviews*, 123:485–606, April 2006.

E. Gonzalez-Alfonso and J. Cernicharo. HCN hyperfine anomalies in dark clouds. *A&A*, 279:506–520, November 1993.

K. D. Gordon, C. W. Engelbracht, D. Fadda, J. Stansberry, S. Wachter, D. T. Frayer, G. Rieke, A. Noriega-Crespo, W. B. Latter, E. Young, G. Neugebauer, Z. Balog, J. W. Beeman, H. Dole, E. Egami, E. E. Haller, D. Hines, D. Kelly, F. Marleau, K. Misselt, J. Morrison, P. Pérez-González, J. Rho, and W. A. Wheaton. Absolute Calibration and Characterization of the Multiband Imaging Photometer for Spitzer. II. 70 $\mu$m Imaging. *PASP*, 119:1019–1037, September 2007.

M. Griffin, A. Abergel, P. Ade, P. André, J.-P. Baluteau, J. Bock, A. Franceschini, W. Gear, J. Glenn, D. Griffin, K. King, E. Lellouch, D. Naylor, G. Olofsson, I. Perez-Fournon, M. Rowan-Robinson, P. Saraceno, E. Sawyer, A. Smith, B. Swinyard, L. Vigroux, and G. Wright. Herschel-SPIRE: design, performance, and scientific capabilities. In *Space Telescopes and Instrumentation I: Optical, Infrared, and Millimeter*, volume 6265 of *Proceedings of SPIE*, July 2006.

P. Hennebelle, M. Pérault, D. Teyssier, and S. Ganesh. Infrared dark clouds from the ISOGAL survey. Constraints on the interstellar extinction curve. *A&A*, 365:598–611, January 2001.

Th. Henning, W. Pfau, and W. J. Altenhoff. Infrared and radio emission from very young and massive stellar objects. *A&A*, 227:542–552, January 1990.

Th. Henning, A. Lapinov, K. Schreyer, B. Stecklum, and I. Zinchenko. IRAS 12326-6245: Luminous very young stellar objects with a massive molecular outflow. *A&A*, 364:613–624, December 2000.

Th. Henning, K. Schreyer, R. Launhardt, and A. Burkert. Massive young stellar objects with molecular outflows. *A&A*, 353:211–226, January 2000.

S. J. U. Higdon, D. Devost, J. L. Higdon, B. R. Brandl, J. R. Houck, P. Hall, D. Barry, V. Charmandaris, J. D. T. Smith, G. C. Sloan, and J. Green. The SMART Data Analysis Package for the Infrared Spectrograph on the Spitzer Space Telescope. *PASP*, 116:975–984, October 2004.

W. S. Holland, E. I. Robson, W. K. Gear, C. R. Cunningham, J. F. Lightfoot, T. Jenness, R. J. Ivison, J. A. Stevens, P. A. R. Ade, M. J. Griffin, W. D. Duncan, J. A. Murphy, and D. A. Naylor. SCUBA: a common-user submillimetre camera operating on the James Clerk Maxwell Telescope. *MNRAS*, 303:659–672, March 1999.

J. L. Hora, B. M. Patten, G. G. Fazio, and W. J. Glaccum. The effects of cosmic rays and solar flares on the IRAC detectors: the first two years of in-flight operation. In D. A. Dorn and A. D. Holland, editors, *High Energy, Optical, and Infrared Detectors for Astronomy II*, volume 6276 of *Society of Photo-Optical Instrumentation Engineers (SPIE) Conference Series*, July 2006.

T. Hosokawa and K. Omukai. Evolution of Massive Protostars with High Accretion Rates. *ArXiv e-prints*, June 2008.

S. Hotzel. The ISOPHOT Serendipity Survey – Structures in the Cold Dust of the Milky Way. *Ph.D. Thesis, Combined Faculties for the Natural Sciences and for Mathematics of the Ruperto-Carola University of Heidelberg, Germany*, May 2001.

J. R. Houck, T. L. Roellig, J. van Cleve, W. J. Forrest, T. Herter, C. R. Lawrence, K. Matthews, H. J. Reitsema, B. T. Soifer, D. M. Watson, D. Weedman, M. Huisjen, J. Troeltzsch, D. J. Barry, J. Bernard-Salas, C. E. Blacken, B. R. Brandl, V. Charmandaris, D. Devost, G. E. Gull, P. Hall, C. P. Henderson, S. J. U. Higdon, B. E. Pirger, J. Schoenwald, G. C. Sloan, K. I. Uchida, P. N. Appleton, L. Armus, M. J. Burgdorf, S. B. Fajardo-Acosta, C. J. Grillmair, J. G. Ingalls, P. W. Morris, and H. I. Teplitz. The Infrared Spectrograph (IRS) on the Spitzer Space Telescope. *ApJS*, 154:18–24, September 2004.

J. B. Hutchings, D. Aldridge, R. Doyon, C. Evans, D. Provencal, and N. Rowlands. The Fine Guidance Sensor for the JWST. In *Bulletin of the American Astronomical Society*, volume 37, pages 1353–+, December 2005.

R. Indebetouw, J. S. Mathis, B. L. Babler, M. R. Meade, C. Watson, B. A. Whitney, M. J. Wolff, M. G. Wolfire, M. Cohen, T. M. Bania, R. A. Benjamin, D. P. Clemens, J. M. Dickey, J. M. Jackson, H. A. Kobulnicky, A. P. Marston, E. P. Mercer, J. R.

Stauffer, S. R. Stolovy, and E. Churchwell. The Wavelength Dependence of Interstellar Extinction from 1.25 to 8.0 $\mu$m Using GLIMPSE Data. *ApJ*, 619:931–938, February 2005.

R. Indebetouw, T. P. Robitaille, B. A. Whitney, E. Churchwell, B. Babler, M. Meade, C. Watson, and M. Wolfire. Embedded Star Formation in the Eagle Nebula with Spitzer GLIMPSE. *ApJ*, 666:321–338, September 2007.

P. Jakobsen, S. Arribas, T. Boeker, A. Bunker, S. Charlot, D. Crampton, P. Ferruit, M. Franx, R. Maiolino, G. de Marchi, H. Moseley, B. Rauscher, M. Regan, H.-W. Rix, and J. Valenti. NIRSpec - Near-IR Multi-Object Spectrograph for JWST. In *Bulletin of the American Astronomical Society*, volume 37, pages 1352–+, December 2005.

A.-K. Jappsen, R. S. Klessen, R. B. Larson, Y. Li, and M.-M. Mac Low. The stellar mass spectrum from non-isothermal gravoturbulent fragmentation. *A&A*, 435:611–623, May 2005.

T. Jenness and F. Economou. The SCUBA Data Reduction Pipeline: ORAC-DR at the JCMT. In D. M. Mehringer, R. L. Plante, and D. A. Roberts, editors, *Astronomical Data Analysis Software and Systems VIII*, volume 172 of *Astronomical Society of the Pacific Conference Series*, pages 171–+, 1999.

T. Jenness and J. F. Lightfoot. Reducing SCUBA Data at the James Clerk Maxwell Telescope. In R. Albrecht, R. N. Hook, and H. A. Bushouse, editors, *Astronomical Data Analysis Software and Systems VII*, volume 145 of *Astronomical Society of the Pacific Conference Series*, pages 216–+, 1998.

M. Juvela, I. Ristorcelli, A. Abergel, Ph. André, J.-P. Bernard, S. Bontemps, S. Boulanger, L. Cambresy, R. Davies, C. Dickinson, F.-X. Désert, X. Dupac, J. Fischera, M. Giard, D. Harrison, J. Harju, G. Joncas, A. Jones, J. Kainulainen, Cs. Kiss, U. Klaas, O. Krause, G. Lagache, J.-M. Lamarre, R. Laureijs, K. Lehtinen, J. F. Macias-Perez, B. Maffei, P. Martin, K. Mattila, P. McGehee, C. Meny, M.-A. Miville-Deschenes, S. Molinari, L. Montier, F. Motte, R. Nartallo, L. Pagani, R. Paladini, V.-M. Pelkonen, J.-L. Puget, W. Reach, J. Tauber, L. V. Toth, L. Valenziano, D. Ward-Thompson, and A. Zavagno. Galactic cold cores: A herschel survey of the source populations revealed by planck. Herschel Open Time Key Programme, `http://herschel.esac.esa.int/Key_Programmes.shtml`, 2007.

M. F. Kessler, J. A. Steinz, M. E. Anderegg, J. Clavel, G. Drechsel, P. Estaria, J. Faelker, J. R. Riedinger, A. Robson, B. G. Taylor, and S. Ximénez de Ferrán. The Infrared Space Observatory (ISO) mission. *A&A*, 315:L27–L31, November 1996.

E. Keto and K. Wood. Observations on the Formation of Massive Stars by Accretion. *ApJ*, 637:850–859, February 2006.

H. Kirk, D. Johnstone, and M. Tafalla. Dynamics of Dense Cores in the Perseus Molecular Cloud. *ApJ*, 668:1042–1063, October 2007.

O. Krause, D. Lemke, L. V. Tóth, U. Klaas, M. Haas, M. Stickel, and R. Vavrek. A very young star forming region detected by the ISOPHOT Serendipity Survey. *A&A*, 398:1007–1020, February 2003.

O. Krause, S. M. Birkmann, G. H. Rieke, D. Lemke, U. Klaas, D. C. Hines, and K. D. Gordon. No cold dust within the supernova remnant Cassiopeia A. *Nature*, 432:596–598, December 2004.

O. Krause, R. Vavrek, S. Birkmann, U. Klaas, M. Stickel, L. V. Tóth, and D. Lemke. Early Stages of Massive Star Formation Revealed by ISO. *Baltic Astronomy*, 13:407–410, 2004.

O. Krause, D. Lemke, R. Hofferbert, A. Böhm, U. Klaas, J. Katzer, F. Höller, and M. Salvasohn. The cold focal plane chopper of HERSCHEL's PACS instrument. In E. Atad-Ettedgui, J. Antebi, and D. Lemke, editors, *Optomechanical Technologies for Astronomy*, volume 6273 of *Proceedings of SPIE*, July 2006.

O. Krause, Th. Henning, H. Beuther, S. Birkmann, M. Hennemann, R. Launhardt, D. Lemke, H. Linz, M. Nielbock, J. Steinacker, R. Klein, B. Stecklum, and P. André. The earliest phases of star formation: From low- to high-mass objects. Herschel-PACS Guaranteed Time Key Programme, `http://herschel.esac.esa.int/Key_Programmes.shtml`, 2007.

O. Krause. The nature of cold sources from the 170 micron ISOPHOT Serendipity Survey. *Ph.D. Thesis, Combined Faculties for the Natural Sciences and for Mathematics of the Ruperto-Carola University of Heidelberg, Germany*, October 2003.

M. R. Krumholz and I. A. Bonnell. Models for the Formation of Massive Stars. *ArXiv e-prints*, December 2007.

M. R. Krumholz and C. F. McKee. A minimum column density of 1gcm$^{-2}$ for massive star formation. *Nature*, 451:1082–1084, February 2008.

M. R. Krumholz and J. C. Tan. Slow Star Formation in Dense Gas: Evidence and Implications. *ApJ*, 654:304–315, January 2007.

M. R. Krumholz, R. I. Klein, and C. F. McKee. Radiation pressure in massive star formation. In R. Cesaroni, M. Felli, E. Churchwell, and M. Walmsley, editors, *Massive Star Birth: A Crossroads of Astrophysics*, volume 227 of *IAU Symposium*, pages 231–236, 2005.

M. R. Krumholz, C. F. McKee, and R. I. Klein. How Protostellar Outflows Help Massive Stars Form. *ApJL*, 618:L33–L36, January 2005.

M. R. Krumholz, C. F. McKee, and R. I. Klein. The formation of stars by gravitational collapse rather than competitive accretion. *Nature*, 438:332–334, November 2005.

M. R. Krumholz, R. I. Klein, and C. F. McKee. Radiation-Hydrodynamic Simulations of Collapse and Fragmentation in Massive Protostellar Cores. *ApJ*, 656:959–979, February 2007.

M. R. Krumholz. Collapse, Fragmentation, and Accretion in Massive Cores. In H. Beuther, H. Linz, and Th. Henning, editors, *Massive Star Formation: Observations Confront Theory*, volume 387 of *Astronomical Society of the Pacific Conference Series*, pages 200–+, May 2008.

S. Kurtz, R. Cesaroni, E. Churchwell, P. Hofner, and C. M. Walmsley. Hot Molecular Cores and the Earliest Phases of High-Mass Star Formation. *Protostars and Planets IV*, pages 299–+, May 2000.

R. B. Larson. Thermal physics, cloud geometry and the stellar initial mass function. *MNRAS*, 359:211–222, May 2005.

D. Lemke, U. Klaas, J. Abolins, P. Abraham, J. Acosta-Pulido, S. Bogun, H. Castaneda, L. Cornwall, L. Drury, C. Gabriel, F. Garzon, H. P. Gemuend, U. Groezinger, E. Gruen, M. Haas, C. Hajduk, G. Hall, I. Heinrichsen, U. Herbstmeier, G. Hirth, R. Joseph, U. Kinkel, S. Kirches, C. Koempe, W. Kraetschmer, E. Kreysa, H. Krueger, M. Kunkel, R. Laureijs, P. Luetzow-Wentzky, K. Mattila, T. Mueller, T. Pacher, G. Pelz, E. Popow, I. Rasmussen, J. Rodriguez Espinosa, P. Richards, S. Russell, H. Schnopper, J. Schubert, B. Schulz, C. Telesco, C. Tilgner, R. Tuffs, H. Voelk, H. Walker, M. Wells, and J. Wolf. ISOPHOT - capabilities and performance. *A&A*, 315:L64–L70, November 1996.

D. Lemke, A. Böhm, F. de Bonis, M. Ebert, T. Gross, U. Grözinger, Th. Henning, M. Hinz, R. Hofferbert, A. Huber, O. Krause, S. Kuhlmann, G. Luichtel, J. Ramos, R.-R. Rohloff, C. Stein, M. Trunz, M. Übele, and K. Weidlich. Cryogenic filter- and spectrometer wheels for the Mid Infrared Instrument (MIRI) of the James Webb Space Telescope (JWST). In *Optomechanical Technologies for Astronomy*, volume 6273 of *Proceedings of SPIE*, July 2006.

Tanya Lim, Jose L. Alvarez, Eva Bauwens, Alejandro Garcia Bedregal, Joris Blommaert, Helmut Dannerbauer, Paul Eccleston, Marc Ferlet, Sebastian Fischer, Macarena Garcia-Marin, Alistair Glasse, Adrian Michael Glauser, Karl Gordon, Tom Greene, Tim Grundy, Martin Hennemann, Ulrich Klaas, Alvaro Labiano, Fred Lahuis, Juan Rafael Martínez-Galarza, Bruno Merin Martin, Jane Morrison, Theodoros Nakos, Brian O'Sullivan, Bart Pindor, Michael Ressler, Bryan Shaughnessy, Bart Vandenbussche, Martyn Wells, Gillian Wright, and Jens Zuther. First results from miri verification model testing. volume 7010, page 70103A. SPIE, 2008.

H. Linz, B. Stecklum, Th. Henning, P. Hofner, and B. Brandl. The G9.62+0.19-F hot molecular core. The infrared view on very young massive stars. *A&A*, 429:903–921, January 2005.

M. Lombardi and J. Alves. Mapping the interstellar dust with near-infrared observations: An optimized multi-band technique. *A&A*, 377:1023–1034, October 2001.

F. J. Low, P. S. Smith, M. Werner, C. Chen, V. Krause, M. Jura, and D. C. Hines. Exploring Terrestrial Planet Formation in the TW Hydrae Association. *ApJ*, 631:1170–1179, October 2005.

M.-M. Mac Low and R. S. Klessen. Control of star formation by supersonic turbulence. *Reviews of Modern Physics*, 76:125–194, January 2004.

D. Makovoz and F. R. Marleau. Point-Source Extraction with MOPEX. *PASP*, 117:1113–1128, October 2005.

C. F. McKee and J. C. Tan. Massive star formation in 100,000 years from turbulent and pressurized molecular clouds. *Nature*, 416:59–61, March 2002.

C. F. McKee and J. C. Tan. The Formation of Massive Stars from Turbulent Cores. *ApJ*, 585:850–871, March 2003.

F. Motte, S. Bontemps, P. Schilke, N. Schneider, K. M. Menten, and D. Broguière. The earliest phases of high-mass star formation: a 3 square degree millimeter continuum mapping of Cygnus X. *A&A*, 476:1243–1260, December 2007.

H. Murakami, H. Baba, P. Barthel, D. L. Clements, M. Cohen, Y. Doi, K. Enya, E. Figueredo, N. Fujishiro, H. Fujiwara, M. Fujiwara, P. Garcia-Lario, T. Goto, S. Hasegawa, Y. Hibi, T. Hirao, N. Hiromoto, S. S. Hong, K. Imai, M. Ishigaki, M. Ishiguro, D. Ishihara, Y. Ita, W.-S. Jeong, K. S. Jeong, H. Kaneda, H. Kataza, M. Kawada, T. Kawai, A. Kawamura, M. F. Kessler, D. Kester, T. Kii, D. C. Kim, W. Kim, H. Kobayashi, B. C. Koo, S. M. Kwon, H. M. Lee, R. Lorente, S. Makiuti, H. Matsuhara, T. Matsumoto, H. Matsuo, S. Matsuura, T. G. Müller, N. Murakami, H. Nagata, T. Nakagawa, T. Naoi, M. Narita, M. Noda, S. H. Oh, A. Ohnishi, Y. Ohyama, Y. Okada, H. Okuda, S. Oliver, T. Onaka, T. Ootsubo, S. Oyabu, S. Pak, Y.-S. Park, C. P. Pearson, M. Rowan-Robinson, T. Saito, I. Sakon, A. Salama, S. Sato, R. S. Savage, S. Serjeant, H. Shibai, M. Shirahata, J. Sohn, T. Suzuki, T. Takagi, H. Takahashi, T. Tanabé, T. T. Takeuchi, S. Takita, M. Thomson, K. Uemizu, M. Ueno, F. Usui, E. Verdugo, T. Wada, L. Wang, T. Watabe, H. Watarai, G. J. White, I. Yamamura, C. Yamauchi, and A. Yasuda. The Infrared Astronomical Mission AKARI. *PASJ*, 59:369–+, October 2007.

G. Neugebauer, H. J. Habing, R. van Duinen, H. H. Aumann, B. Baud, C. A. Beichman, D. A. Beintema, N. Boggess, P. E. Clegg, T. de Jong, J. P. Emerson, T. N. Gautier, F. C. Gillett, S. Harris, M. G. Hauser, J. R. Houck, R. E. Jennings, F. J. Low, P. L. Marsden, G. Miley, F. M. Olnon, S. R. Pottasch, E. Raimond, M. Rowan-Robinson, B. T. Soifer, R. G. Walker, P. R. Wesselius, and E. Young. The Infrared Astronomical Satellite (IRAS) mission. *ApJL*, 278:L1–L6, March 1984.

A. Noriega-Crespo, P. Morris, F. R. Marleau, S. Carey, A. Boogert, E. van Dishoeck, N. J. Evans, II, J. Keene, J. Muzerolle, K. Stapelfeldt, K. Pontoppidan, P. Lowrance, L. Allen, and T. L. Bourke. A New Look at Stellar Outflows: Spitzer Observations of the HH 46/47 System. *ApJS*, 154:352–358, September 2004.

V. Ossenkopf and Th. Henning. Dust opacities for protostellar cores. *A&A*, 291:943–959, November 1994.

M. Osterloh, Th. Henning, and R. Launhardt. Infrared Images and Millimeter Data from Cold Southern IRAS Sources. *ApJS*, 110:71–+, May 1997.

P. Padoan and Å. Nordlund. The Stellar Initial Mass Function from Turbulent Fragmentation. *ApJ*, 576:870–879, September 2002.

P. Padoan, Å. Nordlund, A. G. Kritsuk, M. L. Norman, and P. S. Li. Two Regimes of Turbulent Fragmentation and the Stellar Initial Mass Function from Primordial to Present-Day Star Formation. *ApJ*, 661:972–981, June 2007.

F. Palla, R. Cesaroni, J. Brand, P. Caselli, G. Comoretto, and M. Felli. H2O masers associated with dense molecular clouds and ultracompact H II regions. 2: The extended sample. *A&A*, 280:599–608, December 1993.

Y. N. Pavlyuchenkov and B. M. Shustov. A Method for Molecular-Line Radiative-Transfer Computations and Its Application to a Two-Dimensional Model for the Starless Core L1544. *Astronomy Reports*, 48:315–326, April 2004.

Y. Pavlyuchenkov, D. Wiebe, B. Shustov, Th. Henning, R. Launhardt, and D. Semenov. Molecular Emission Line Formation in Prestellar Cores. *ArXiv e-prints*, August 2008.

E. Peeters, H. W. W. Spoon, and A. G. G. M. Tielens. Polycyclic Aromatic Hydrocarbons as a Tracer of Star Formation? *ApJ*, 613:986–1003, October 2004.

E. Peeters, N. L. Martín-Hernández, N. J. Rodríguez-Fernández, and X. Tielens. High Excitation ISM and Gas. *Space Science Reviews*, 119:273–292, August 2005.

M. Perault, A. Omont, G. Simon, P. Seguin, D. Ojha, J. Blommaert, M. Felli, G. Gilmore, F. Guglielmo, H. Habing, S. Price, A. Robin, B. de Batz, C. Cesarsky, D. Elbaz, N. Epchtein, P. Fouque, S. Guest, D. Levine, A. Pollock, T. Prusti, R. Siebenmorgen, L. Testi, and D. Tiphene. First ISOCAM images of the Milky Way. *A&A*, 315:L165–L168, November 1996.

G. L. Pilbratt. Herschel Space Observatory - Overview and Observing Opportunities. In *Bulletin of the American Astronomical Society*, volume 37, pages 1219–+, December 2005.

G. Pilbratt. Herschel Mission Overview, Photometry, and Key Programmes. In *37th COSPAR Scientific Assembly. Held 13-20 July 2008, in Montréal, Canada*, 2008.

A. Poglitsch, C. Waelkens, O. H. Bauer, J. Cepa, H. Feuchtgruber, Th. Henning, C. van Hoof, F. Kerschbaum, D. Lemke, E. Renotte, L. Rodriguez, P. Saraceno, and B. Vandenbussche. The photodetector array camera and spectrometer (PACS) for the Herschel Space Observatory. In *Space Telescopes and Instrumentation I: Optical, Infrared, and Millimeter*, volume 6265 of *Proceedings of SPIE*, July 2006.

W. H. Press, S. A. Teukolsky, W. T. Vetterling, and B. P. Flannery. *Numerical recipes in FORTRAN. The art of scientific computing.* Cambridge: University Press, second edition, 1992.

J. M. Rathborne, J. M. Jackson, and R. Simon. Infrared Dark Clouds: Precursors to Star Clusters. *ApJ*, 641:389–405, April 2006.

J. M. Rathborne, R. Simon, and J. M. Jackson. The Detection of Protostellar Condensations in Infrared Dark Cloud Cores. *ApJ*, 662:1082–1092, June 2007.

M. G. Rawlings, M. Juvela, K. Mattila, K. Lehtinen, and D. Lemke. ISO observations of 3-200 $\mu$m emission by three dust populations in an isolated local translucent cloud. *MNRAS*, 356:810–828, January 2005.

W. T. Reach, J. Rho, E. Young, J. Muzerolle, S. Fajardo-Acosta, L. Hartmann, A. Sicilia-Aguilar, L. Allen, S. Carey, J.-C. Cuillandre, T. H. Jarrett, P. Lowrance, A. Marston, A. Noriega-Crespo, and R. L. Hurt. Protostars in the Elephant Trunk Nebula. *ApJS*, 154:385–390, September 2004.

W. T. Reach, S. T. Megeath, M. Cohen, J. Hora, S. Carey, J. Surace, S. P. Willner, P. Barmby, G. Wilson, W. Glaccum, P. Lowrance, M. Marengo, and G. G. Fazio. Absolute Calibration of the Infrared Array Camera on the Spitzer Space Telescope. *PASP*, 117:978–990, September 2005.

W. T. Reach. SIRTF Background Estimation: Methods and implementation. Technical Report, IPAC, Pasadena, http://ssc.spitzer.caltech.edu/documents/background/, 2000.

M. P. Redman, T. Khanzadyan, R. M. Loughnane, and P. B. Carolan. Cold Supersonic Turbulence in Massive Cores. In H. Beuther, H. Linz, and Th. Henning, editors, *Massive Star Formation: Observations Confront Theory*, volume 387 of *Astronomical Society of the Pacific Conference Series*, pages 38–+, May 2008.

B. Reipurth and J. Bally. Herbig-Haro Flows: Probes of Early Stellar Evolution. *ARAA*, 39:403–455, 2001.

Michael E. Ressler, Hyung Cho, Richard A. M. Lee, Kalyani G. Sukhatme, John J. Drab, George Domingo, Mark E. McKelvey, Jr. Robert E. McMurray, and Jessie L. Dotson. Performance of the jwst/miri si:as detectors. volume 7021, page 70210O. SPIE, 2008.

G. H. Rieke, E. T. Young, C. W. Engelbracht, D. M. Kelly, F. J. Low, E. E. Haller, J. W. Beeman, K. D. Gordon, J. A. Stansberry, K. A. Misselt, J. Cadien, J. E. Morrison, G. Rivlis, W. B. Latter, A. Noriega-Crespo, D. L. Padgett, K. R. Stapelfeldt, D. C. Hines, E. Egami, J. Muzerolle, A. Alonso-Herrero, M. Blaylock, H. Dole, J. L. Hinz, E. Le Floc'h, C. Papovich, P. G. Pérez-González, P. S. Smith, K. Y. L. Su, L. Bennett, D. T. Frayer, D. Henderson, N. Lu, F. Masci, M. Pesenson, L. Rebull, J. Rho, J. Keene, S. Stolovy, S. Wachter, W. Wheaton, M. W. Werner, and P. L. Richards. The Multiband Imaging Photometer for Spitzer (MIPS). *ApJS*, 154:25–29, September 2004.

M. Rieke, D. Kelly, S. Horner, and NIRCam Team. The Near Infrared Camera (NIRCam) for the James Webb Space Telescope (JWST). In *Bulletin of the American Astronomical Society*, volume 37, pages 1351–+, December 2005.

T. P. Robitaille, B. A. Whitney, R. Indebetouw, K. Wood, and P. Denzmore. Interpreting Spectral Energy Distributions from Young Stellar Objects. I. A Grid of 200,000 YSO Model SEDs. *ApJS*, 167:256–285, December 2006.

T. P. Robitaille, B. A. Whitney, R. Indebetouw, and K. Wood. Interpreting Spectral Energy Distributions from Young Stellar Objects. II. Fitting Observed SEDs Using a Large Grid of Precomputed Models. *ApJS*, 169:328–352, April 2007.

D. Rouan, A. Boccaletti, P. Baudoz, C. Cavarroc, J. Baudrand, and J. M. Reess. The Coronagraphic Mode of MIRI/JWST. In P. Kalas, editor, *In the Spirit of Bernard Lyot: The Direct Detection of Planets and Circumstellar Disks in the 21st Century*, June 2007.

G. Sandell and D. A. Weintraub. On the Similarity of FU Orionis Stars to Class I Protostars: Evidence from the Submillimeter. *ApJS*, 134:115–132, May 2001.

R. J. Sault, P. J. Teuben, and M. C. H. Wright. A Retrospective View of MIRIAD. In R. A. Shaw, H. E. Payne, and J. J. E. Hayes, editors, *Astronomical Data Analysis Software and Systems IV*, volume 77 of *Astronomical Society of the Pacific Conference Series*, pages 433–+, 1995.

F. L. Schöier, F. F. S. van der Tak, E. F. van Dishoeck, and J. H. Black. An atomic and molecular database for analysis of submillimetre line observations. *A&A*, 432:369–379, March 2005.

D. S. Shepherd and E. Churchwell. Bipolar Molecular Outflows in Massive Star Formation Regions. *ApJ*, 472:225–+, November 1996.

D. S. Shepherd, M. S. Povich, B. A. Whitney, T. P. Robitaille, D. E. A. Nürnberger, L. Bronfman, D. P. Stark, R. Indebetouw, M. R. Meade, and B. L. Babler. Molecular Outflows and a Mid-Infrared Census of the Massive Star Formation Region Associated with IRAS 18507+0121. *ApJ*, 669:464–482, November 2007.

R. F. Silverberg, M. G. Hauser, N. W. Boggess, T. J. Kelsall, S. H. Moseley, and T. L. Murdock. Design of the diffuse infrared background experiment (DIRBE) on COBE. In M. S. Scholl, editor, *Infrared Spaceborne Remote Sensing*, volume 2019 of *Proceedings of SPIE*, pages 180–189, October 1993.

R. Simon, J. M. Jackson, J. M. Rathborne, and E. T. Chambers. A Catalog of Midcourse Space Experiment Infrared Dark Cloud Candidates. *ApJ*, 639:227–236, March 2006.

M. D. Smith and A. Rosen. Synthetic Spitzer Infrared Array Camera band maps from simulations of protostellar jets. *MNRAS*, 357:1370–1376, March 2005.

T. K. Sridharan, H. Beuther, P. Schilke, K. M. Menten, and F. Wyrowski. High-Mass Protostellar Candidates. I. The Sample and Initial Results. *ApJ*, 566:931–944, February 2002.

T. K. Sridharan, H. Beuther, M. Saito, F. Wyrowski, and P. Schilke. High-Mass Starless Cores. *ApJL*, 634:L57–L60, November 2005.

S. W. Stahler and F. Palla. *The Formation of Stars*. The Formation of Stars, by Steven W. Stahler, Francesco Palla, pp. 865. ISBN 3-527-40559-3. Wiley-VCH , January 2005., January 2005.

B. Stecklum, B. Brandl, Th. Henning, I. Pascucci, T. L. Hayward, and J. C. Wilson. High resolution mid-infrared imaging of W3(OH). *A&A*, 392:1025–1029, September 2002.

J. Steinacker, A. Bacmann, Th. Henning, R. Klessen, and M. Stickel. 3D continuum radiative transfer in complex dust configurations. II. 3D structure of the dense molecular cloud core $\rho$ Oph D. *A&A*, 434:167–180, April 2005.

J. Steinacker, A. Bacmann, and Th. Henning. Ray Tracing for Complex Astrophysical High-opacity Structures. *ApJ*, 645:920–927, July 2006.

M. Stickel, D. Lemke, S. Bogun, U. Klaas, M. Kunkel, L. V. Toth, S. Hotzel, U. Herbstmeier, M. F. Kessler, R. J. Laureijs, M. J. Burgdorf, C. A. Beichman, M. Rowan-Robinson, A. Efstathiou, G. Richter, and M. Braun. ISOPHOT far-infrared serendipity sky survey. In P. J. Quinn, editor, *Observatory Operations to Optimize Scientific Return*, volume 3349 of *Proceedings of SPIE*, pages 115–125, July 1998.

M. Stickel, D. Lemke, U. Klaas, O. Krause, and S. Egner. The ISOPHOT 170 $\mu$m Serendipity Survey II. The catalog of optically identified galaxies%. *A&A*, 422:39–54, July 2004.

M. Stickel, U. Klaas, and D. Lemke. The ISOPHOT 170 $\mu$m Serendipity Survey. III. FIR statistics of optically identified galaxies. *A&A*, 466:831–838, May 2007.

M. Stickel, O. Krause, U. Klaas, and D. Lemke. The ISOPHOT 170 $\mu$m Serendipity Survey. IV. The far-infrared sky atlas. *A&A*, 466:1205–1210, May 2007.

J. A. Tauber. The Planck mission. *Advances in Space Research*, 34:491–496, 2004.

A. G. G. M. Tielens, S. Hony, C. van Kerckhoven, and E. Peeters. Interstellar and circumstellar PAHs. In P. Cox and M. Kessler, editors, *The Universe as Seen by ISO*, volume 427 of *ESA Special Publication*, pages 579–+, March 1999.

D. Tody. IRAF in the Nineties. In R. J. Hanisch, R. J. V. Brissenden, and J. Barnes, editors, *Astronomical Data Analysis Software and Systems II*, volume 52 of *Astronomical Society of the Pacific Conference Series*, pages 173–+, January 1993.

E. F. van Dishoeck. Interstellar Medium - Part Two - the Chemical State of Diffuse and Dense Interstellar Gas. In T. Encrenaz and M. F. Kessler, editors, *Infrared Astronomy with ISO*, pages 283–+, 1992.

E. I. Vorobyov and S. Basu. The Burst Mode of Protostellar Accretion. *ApJ*, 650:956–969, October 2006.

C. M. Walmsley, E. Churchwell, A. Nash, and E. Fitzpatrick. Hyperfine anomalies of HCN in cold dark clouds. *ApJL*, 258:L75–L78, July 1982.

A. J. Walsh, P. C. Myers, J. Di Francesco, S. Mohanty, T. L. Bourke, R. Gutermuth, and D. Wilner. A Large-Scale Survey of NGC 1333. *ApJ*, 655:958–972, February 2007.

D. Ward-Thompson, F. Motte, and P. Andre. The initial conditions of isolated star formation - III. Millimetre continuum mapping of pre-stellar cores. *MNRAS*, 305:143–150, May 1999.

D. Ward-Thompson, P. André, R. Crutcher, D. Johnstone, T. Onishi, and C. Wilson. An Observational Perspective of Low-Mass Dense Cores II: Evolution Toward the Initial Mass Function. In B. Reipurth, D. Jewitt, and K. Keil, editors, *Protostars and Planets V*, pages 33–46, 2007.

M. W. Werner, T. L. Roellig, F. J. Low, G. H. Rieke, M. Rieke, W. F. Hoffmann, E. Young, J. R. Houck, B. Brandl, G. G. Fazio, J. L. Hora, R. D. Gehrz, G. Helou, B. T. Soifer, J. Stauffer, J. Keene, P. Eisenhardt, D. Gallagher, T. N. Gautier, W. Irace, C. R. Lawrence, L. Simmons, J. E. Van Cleve, M. Jura, E. L. Wright, and D. P. Cruikshank. The Spitzer Space Telescope Mission. *ApJS*, 154:1–9, September 2004.

B. A. Whitney, K. Wood, J. E. Bjorkman, and M. J. Wolff. Two-dimensional Radiative Transfer in Protostellar Envelopes. I. Effects of Geometry on Class I Sources. *ApJ*, 591:1049–1063, July 2003.

J. Wolf, L. Wiest, U. Groezinger, D. Lemke, and J. Schubert. Si:As blocked-impurity-band detectors for ISO's photometer. In M. S. Scholl and B. F. Andresen, editors, *Infrared Spaceborne Remote Sensing III*, volume 2553 of *Proceedings of SPIE*, pages 482–488, September 1995.

S. Wolf, Th. Henning, and B. Stecklum. Multidimensional self-consistent radiative transfer simulations based on the Monte-Carlo method. *A&A*, 349:839–850, September 1999.

D. O. S. Wood and E. Churchwell. Massive stars embedded in molecular clouds - Their population and distribution in the galaxy. *ApJ*, 340:265–272, May 1989.

G. S. Wright, G. H. Rieke, L. Colina, E. van Dishoeck, G. Goodson, T. Greene, P.-O. Lagage, A. Karnik, S. D. Lambros, D. Lemke, M. Meixner, H.-U. Norgaard, G. Oloffson, T. Ray, M. Ressler, C. Waelkens, D. Wright, and A. Zhender. The JWST MIRI instrument concept. In J. C. Mather, editor, *Optical, Infrared, and Millimeter Space Telescopes*, volume 5487 of *Proceedings of SPIE*, pages 653–663, October 2004.

Y. Wu, Y. Wei, M. Zhao, Y. Shi, W. Yu, S. Qin, and M. Huang. A study of high velocity molecular outflows with an up-to-date sample. *A&A*, 426:503–515, November 2004.

H. W. Yorke and P. Bodenheimer. Theoretical Developments in Understanding Massive Star Formation. In H. Beuther, H. Linz, and Th. Henning, editors, *Massive Star Formation: Observations Confront Theory*, volume 387 of *Astronomical Society of the Pacific Conference Series*, pages 189–+, May 2008.

H. W. Yorke and C. Sonnhalter. On the Formation of Massive Stars. *ApJ*, 569:846–862, April 2002.

H. W. Yorke. Evolution of Accreting Protostars. In J. Steinacker and A. Bacman, editors, *EPoS 2008: The Early Phase of Star Formation—The future of the field*, July 2008.

Q. Zhang, T. K. Sridharan, T. R. Hunter, Y. Chen, H. Beuther, and F. Wyrowski. A jet-like outflow toward the high-mass (proto) stellar object IRAS 18566+0408. *A&A*, 470:269–279, July 2007.

H. Zinnecker and H. W. Yorke. Toward Understanding Massive Star Formation. *ARAA*, 45:481–563, September 2007.

H. Zinnecker. Prediction of the protostellar mass spectrum in the Orion near-infrared cluster. *New York Academy Sciences Annals*, 395:226–235, October 1982.

# Danksagung

Ich möchte allen danken, die zur Entstehung dieser Arbeit beigetragen haben:

Herrn Prof. Dr. Dietrich Lemke, für die Möglichkeit, dieses interessante Thema zu bearbeiten; für die sehr gute Betreuung und die kritische Durchsicht der Arbeit.

Herrn Prof. Dr. Wolfgang Duschl, für das Mitwirken in meinem Betreuungskomitee und die freundliche Übernahme des Zweitgutachtens.

Herrn Dr. Ulrich Klaas, für die Unterstützung und Zusammenarbeit im Rahmen der MIRI Testkampagne und die Teilnahme an meinem Betreuungskomitee.

Den Herren Dr. Oliver Krause und Dr. Stephan Birkmann, für die vielen Hilfestellungen insbesondere bei Beobachtungsanträgen und Beobachtungen.

Herrn Prof. Dr. Thomas Henning und Herrn Prof. Dr. Hans-Walter Rix, für die Möglichkeit, die Doktorarbeit am Max-Planck-Institut für Astronomie durchzuführen; für die Finanzierung von Konferenzteilnahmen und Beobachtungsaufenthalten, und für die gute Zusammenarbeit.

Herrn Prof. Dr. Kalevi Mattila, für die freundliche Aufnahme an der Sternwarte der Universität Helsinki.

Herrn Dr. Hendrik Linz, für die gewissenhafte Durchsicht von Teilen dieser Arbeit.

Allen Kollegen in der Gruppe Infrarot-Weltraumastronomie, am Institut und in Heidelberg, für die Hilfe bei verschiedensten Fragen, und für die sehr angenehme Arbeitsatmosphäre.

Meiner lieben Freundin Sarah.